Measurement of Cherenkov light with the HEAT telescopes at the Pierre Auger Observatory

von

Ilya Bekman

Masterarbeit in Physik

vorgelegt der
Fakultät für Mathematik, Informatik und Naturwissenschaften
der
Rheinisch-Westfälischen Technischen Hochschule Aachen

in Juli 2012

angefertigt am

III. Physikalischen Institut A

Erstgutachter und Betreuer	Zweitgutachter
Prof. Dr. Thomas Hebbeker III. Physikalisches Institut A RWTH Aachen	Prof. Dr. Christopher Wiebusch III. Physikalisches Institut B RWTH Aachen

Abstract

Measurement of Cherenkov light with the HEAT telescopes at the Pierre Auger Observatory
The Pierre Auger Observatory in Argentina examines ultra-high energy cosmic rays. Incident rays in the atmosphere interact with atomic nuclei initiating cascades of subatomic interactions resulting in extensive air showers. These excite gas molecules, which emit fluorescence and Cherenkov light detectable at the ground. This is feasible with the 24 fluorescence telescopes, that are surveying the area of the Observatory. The low-energy extension HEAT (High Elevation Auger Telescopes) consists of three additional fluorescence telescopes with a field of view over the standard telescopes. Because of the different field of view, a higher fraction of incident light is composed of Cherenkov light, which is outside of the usual operational mode of the telescopes. To examine the impact of this effect on the reconstruction of the particle shower, analysis of the reconstruction observables is performed comparing the reconstruction of the air showers Monte-Carlo simulations and and the data acquired with HEAT. The $X_{\max}$ dependence on Cherenkov light fraction is studied.

Messung von Cherenkovlicht mit den HEAT Teleskopen am Pierre Auger Observatorium
Das Pierre Auger Observatorium in Argentinien untersucht höchstenergetische kosmische Strahlung. Wenn diese Strahlung auf die Erdatmosphäre trifft, wechselwirkt sie mit den Atomkernen und löst Teilchenkaskaden und so ausgedehnte Luftschauer aus. Diese regen ihrerseits Moleküle an, sodass Fluoreszenz- und Cherenkov-Licht abgestrahlt und am Boden detektiert werden können. Dies ist mit Hilfe der 24 Fluoreszenzteleskopen, die die Fläche des Observatoriums überschauen, möglich. Die Niederenergieerweiterung HEAT (High Elevation Auger Telescopes) besteht aus drei zusätzlichen Fluoreszenz-Teleskopen, deren Gesichtsfeld über dem der standard Teleskope liegt. Aufgrund des geänderten Gesichtsfeldes wird ein prozentual höherer Anteil an Cherenkov-Licht detektiert, was die Teleskope außerhalb ihres Standatd-Betriebsmodus bringt. Um den Einfluss des Cherenkov-Lichts auf die Schauerrekonstruktion zu untersuchen, werden die Rekonstruktionsobservablen über ein Vergleich der Luftschauer-Simulationen mit den Daten der in HEAT gemessenen Schauer analysiert. Die Abhängigkeit des $X_{\max}$ von dem Cherenkovlichtanteil wird untersucht.

Свет Черенкова в ядерных ливнях из сверхвысокоенергетического космического излучения измеряемый с помошью HEAT в Обсерватории Пьера Оже Обсерватория Пьера Оже в аргентине исследует сверхвысокоенергетическое космическое излучение. Излучение бомбардирует атмосферу и реагирует с её атомами инициируя каскад ядерных взаимодействий, источник ядерных ливней. Так образуемые дочерние частицы возбуждают молекулы газа, которые в свою очередь испускают свечет флуоресценции и Черенкова измеримые на поверхности. Это возможно с помошью 24-х флуоресцентных телескопов осматриваюших плошадь Обсерватории. Низко енергетическое разширение HEAT (High Elevation Auger Telescopes) состоит из трёх дополнительных телескопов, чеё поле зрения приподнято над полем зрения стандартных телескопов. Из-за изменённого поля зрения более высокая часть падаюшего света состоит из излучения Черенкова, так что телескопы работают в не стандартном режиме. Для того чтобы исследовать влияние этого эффекта на реконструкцию ядерных ливней, произведён анализ измеряемых величин сравнивая монте-карло симуляции ядерных ливней с данными добытыми HEAT. Изучается зависимость $X_{\max}$от доли света Черенкова.

Contents

List of Figures

1 Introduction

Cosmic rays opened new insights into high energy physics, space and the Universe as a whole, right from the time of their discovery by Victor Hess at the beginning of the 20^{th} century [1]. Today the composition and origin of cosmic rays are considered fundamental questions of astroparticle physics.

Incident cosmic rays in the atmosphere interact with atomic nuclei initiating cascades of subatomic interactions. These cascades of secondary particles, called extensive air showers, excite gas molecules, which emit detectable fluorescence and Cherenkov light and some secondary particles arrive at the ground. The Pierre Auger Observatory in Argentina examines the cosmic rays at ultra-high energies by measuring the air showers.

The measurement of the light emitted by the air showers is achievable with the 24 fluorescence telescopes, that are surveying the area of the Observatory. The low-energy extension HEAT (High Elevation Auger Telescopes) consists of three additional fluorescence telescopes, with a field of view which is tilted upwards by 30°. This way nearby air showers can be detected. Though, because of the different field of view, a higher fraction of incident light is composed of Cherenkov light, which brings the telescopes outside of the design operational mode.

With Cherenkov-rich showers it is possible to extend the observable spectrum towards lower energies. The shape of the energy spectrum and the composition of the cosmic rays below 10^{18} eV would allow valuable insights into their sources, shading light on the potential region of the transition between the galactical to extragalactical component. The main ingredients to achieve this are quality measurements of the energy, X_{max} and the shower axis.

The impact of Cherenkov light on the shower reconstruction of the HEAT data is to be examined. After the introduction of the detector the simulation and reconstruction of air showers is described. In this work a framework for usage of detailed Monte-Carlo Cherenkov light simulations by CORSIKA is introduced for further cross-checks with Offline light simulations. To study reconstruction framework consistency two datasets of Monte-Carlo showers generated with CORSIKA and CONEX are each separated in Cherenkov-rich and Cherenkov-poor subsets and framework biases are determined and compared to check all steps of the reconstruction and suited datacuts are choosen. In the second step the HEAT data is analysed for X_{max} dependence on Cherenkov light fraction. For CONEX dataset the mean X_{max} is shown to be constant for two different primaries, whereas in the HEAT data are shown to be dependent on Cherenkov light fraction. A correction for the dependence is proposed.

2 Astroparticles

This chapter is mainly based on publications of Blümer et al. [2], Letessier-Selvon and Stanev [3] and Dembinski [4].

2.1 Cosmic rays

Cosmic rays – usually referring to stable charged high energy particles – were found to arrive at the Earth from galactic and probably also extragalactic sources and interact with the atmosphere. The energies of these particles extend over many orders of magnitude, at least up to 10^{20} eV as shown in figure 2.1.

2.1.1 Energy spectrum

The flux of the ultrahigh-energy cosmic rays (UHECR) can be well described by a power law

$$\frac{\mathrm{d}N}{\mathrm{d}E} \propto E^{-\gamma} \quad , \tag{2.1}$$

where the spectral index γ is measured to be about 2.7 up to energies of some PeV. The feature of spectrum at about $10^{15.5}$ eV where γ changes to about 3.2 is called “knee”. At the “ankle” around $10^{18.5}$ eV the spectral index changes to about 2.6, where most models assume a transition between galactic and extragalactic sources [5]. The cut-off of the spectrum is a prominent feature: at about $10^{19.5}$ eV, matching the Greisen-Zatsepin-Kuz’min (GZK) [6, 7] cutoff, γ changes to 4.3.

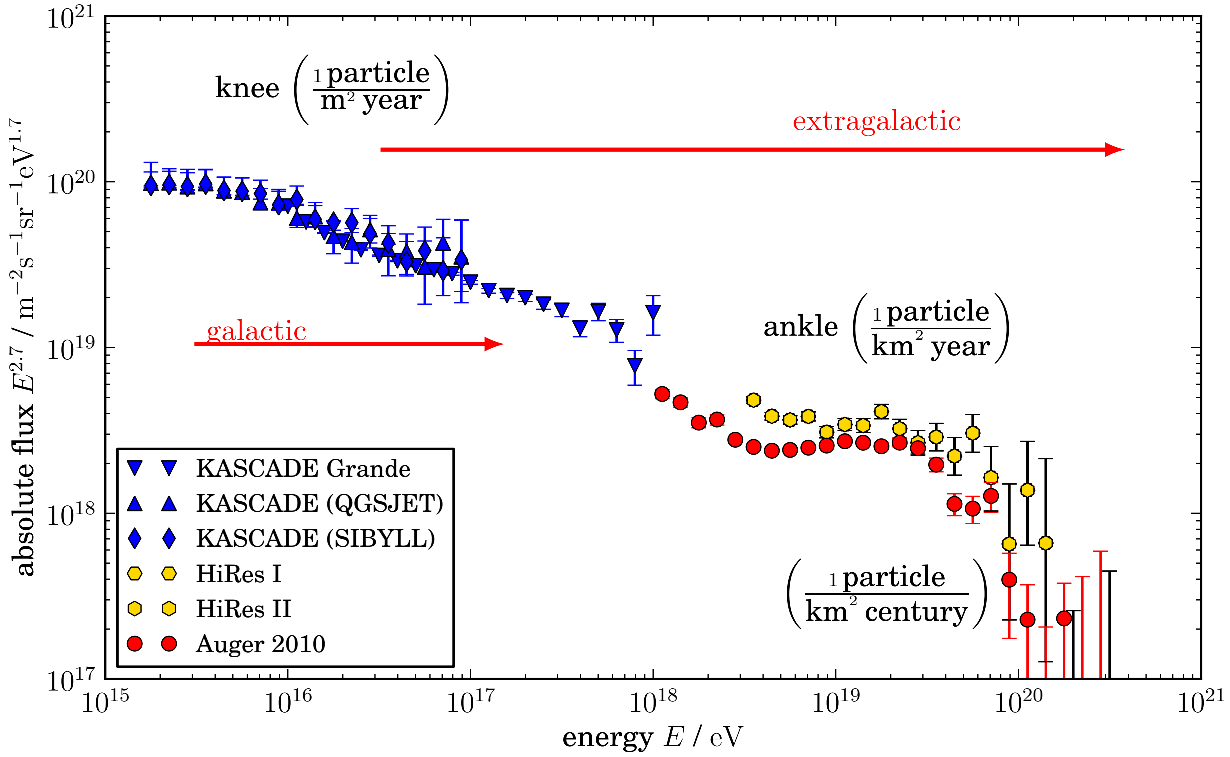

Figure 2.1: Combined spectrum of primary ultrahigh-energy cosmic rays. Courtesy of Tim Niggemann, based on [8, 9, 10, 11, 12, 13].

2.1.2 Sources

One of the most important and yet open questions in modern astroparticle physics is the one of the sources of UHECRs and their acceleration mechanisms. There are two proposed mechanisms to achieve high energies for primary particles: the one-shot acceleration and Fermi shock acceleration. The former can be compared to the techniques used in man-made colliders (e.g. cyclotrons).The latter relies on the multiple scattering of particles on turbulent magnetic fields across the front of a shockwave (e.g. supernovae).

Michael Hillas attributed the energy of the primary particles to the conditions at the potential acceleration sites and combined all in his famous plot (figure 2.2).

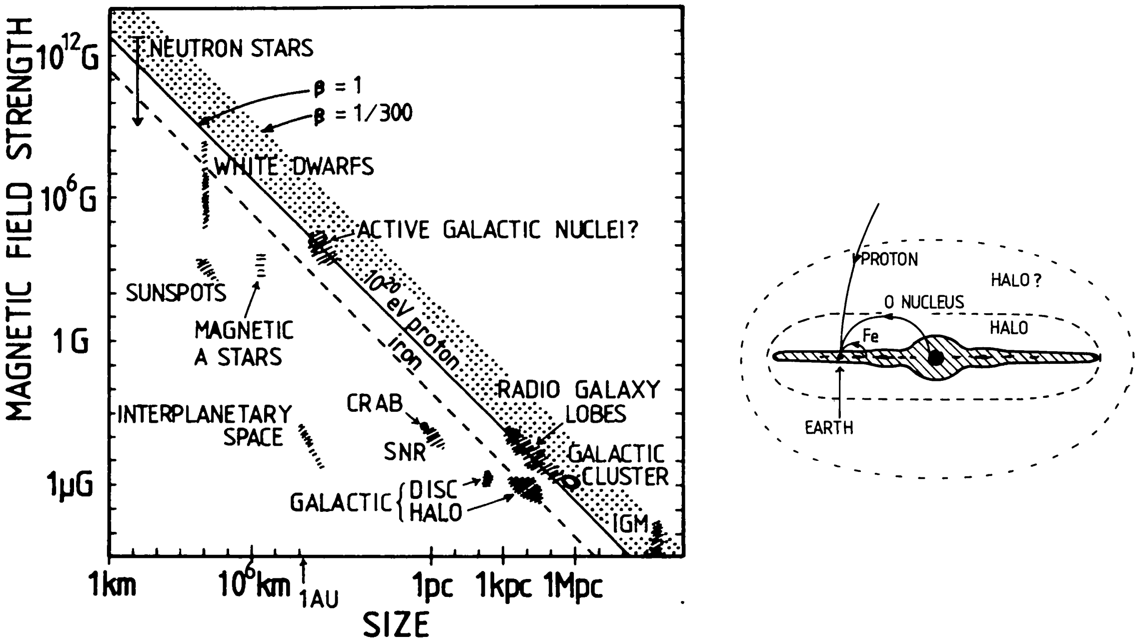

Figure 2.2: *Left*: Hillas plot for acceleration candidates of UHECRs, for p and Fe at $E = 1 \cdot 10^{20}\,\mathrm{eV}$ [5] *Right*: Schematic of gyro radius for different primaries at $E = 7 \cdot 10^{19}\,\mathrm{eV}$ for $B = 2\,\mu\mathrm{G}$. [5]

His idea was to consider the common thread of the acceleration using the relation between the maximum energy of a particle of a certain charge $z \cdot e$, the strength of the magnetic field and the size of the area, where this magnetic field should confine the particle, which is related to the gyro radius R:

$$E_{\mathrm{max}} \simeq \beta\, z\, e \left(\frac{B}{\mu\mathrm{G}}\right)\left(\frac{R}{\mathrm{kpc}}\right) \quad , \tag{2.2}$$

where β denotes the efficiency of the acceleration. As seen on the right of figure 2.2, lighter primaries at high energies have higher gyro radii resulting in a lower probability to be confined on the galactic scale, with this emerged the conclusion of extragalactic origin of highest energy cosmic rays.

The resulting compilation on the left figure 2.2 shows that only a few of the known astrophysical objects are capable of accelerating iron or even proton to $E = 1 \cdot 10^{20}\,\mathrm{eV}$, which could be another reasonable explanation of the GZK-like-cutoff.

2.1.3 Composition

Cosmic rays, further on also called primary particles, can be detected and their charge can be measured directly up to energies of some 100 TeV. Therefore the chemical composition of the cosmic rays is well known for lower energies and is shown in figure 2.3.

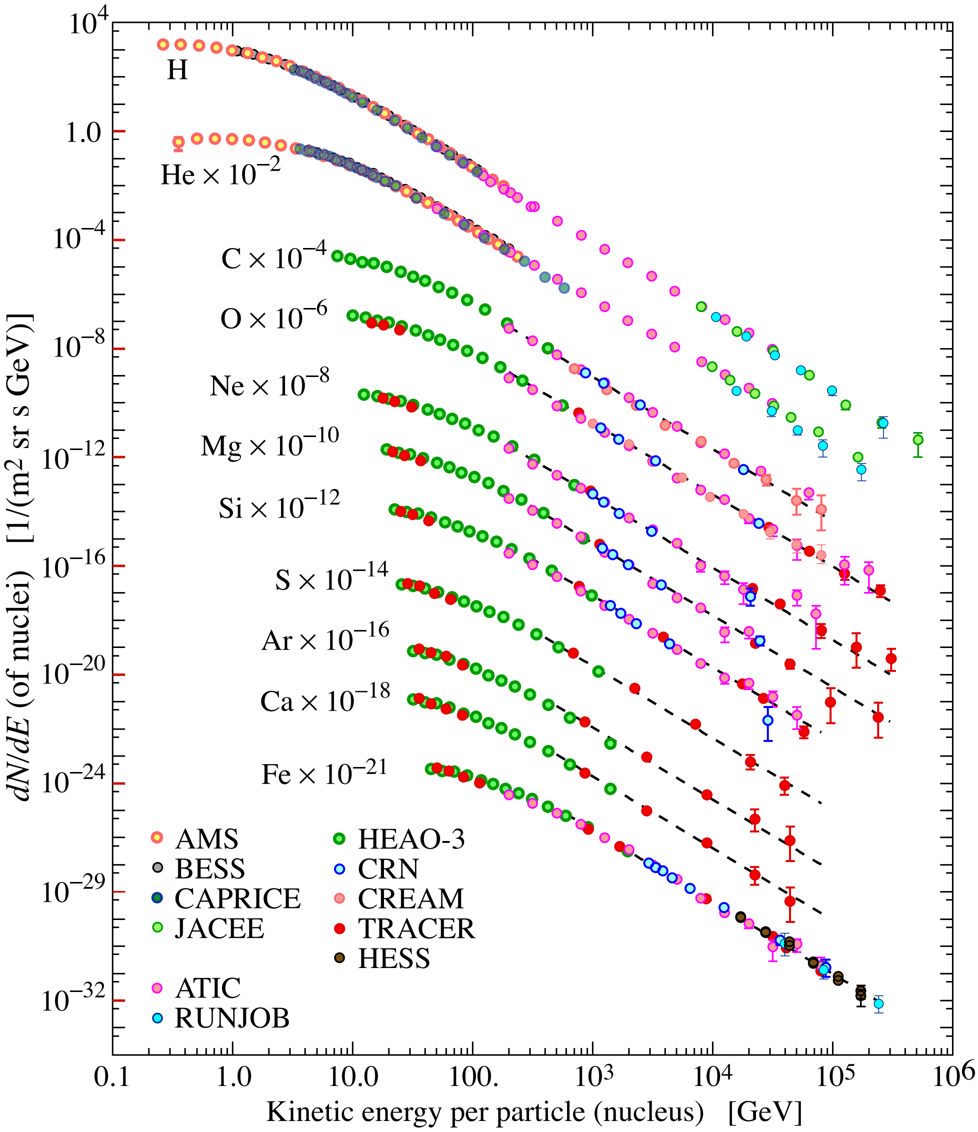

Figure 2.3: Abundance and energy spectrum of different primary particles. [14]

As the flux at high energies rapidly decreases, direct measurements become impractical because of the relatively small instrumented area of balloon- or satellite-borne experiments. Therefore the composition, one of the central questions of the UHECRs, is currently investigated with indirect measurements. The depth of the energy deposit maximum of an extensive air shower ($X_{\max}$) depends approximately linearly on the logarithm of the primary energy ($\lg E_0$) and nucleon number A (see figure 2.2.2). One can estimate the average composition of the primaries by measuring the dependency of $X_{\max}$ on $\lg E_0$, called elongation rate.

2.2 Extensive air showers

First measurements of coincidences between counters at a distance performed by Schmeiser [15], Kohlhörster [16] and Auger in 1938-39 [17] lead to the proposal of extensive air showers induced by cosmic rays. The secondary particles arriving at the surface of the Earth are one of the major means of detecting cosmic rays. Another technique of detecting EAS is the measurement of light emitted by the secondary particles in the atmosphere (see section 2.3 on page 9).

Primary particles arrive from all directions interacting with particles of the atmosphere, most commonly with gas nuclei, and produce secondary particles by inelastic hadronic interactions. These propagate successively and interact with another atmospheric particles building up cascades which are called extensive air showers (EAS). The EAS propagates with roughly speed of light, forming a particle shower front. The energy of the primary particle (i.e. total energy) is distributed among the secondary particles and is almost completely deposited in the atmosphere accompanied by emitting a proportional ammount of fluorescence light, and is thus comparable with a calorimeter with variable density. The incident direction of the primaries is also conserved due to the forward boost of the high energy interactions.

In this process different types of particles are produced as shown in figure 2.4. Usually three components are distinguished - the hadronic, electromagnetic and muonic.

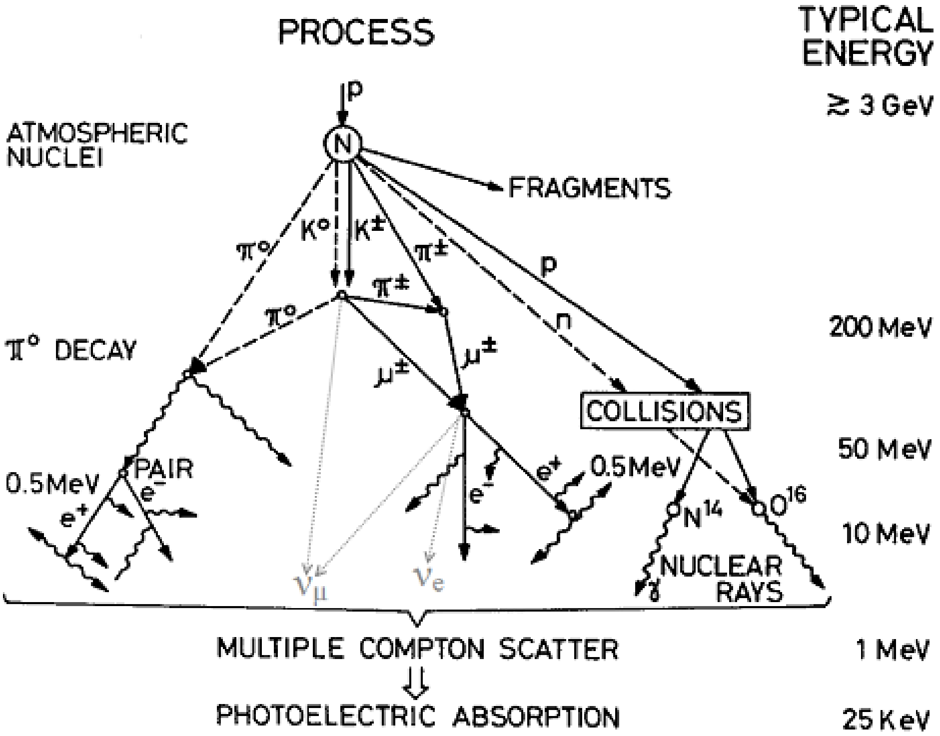

Figure 2.4: Most important processes in air showers. Adopted from [18]

First interactions at the top of the atmosphere produce high energy pions and kaons which can interact further or decay into muons ($\pi^{\pm} \rightarrow \mu^{\pm} + \nu_{\mu^{\mp}}$) or photons ($\pi^{0} \rightarrow \gamma + \gamma$) initiating electromagnetic subcascades. The first and further iterations with nuclei also produce, together with other mesons and bosonic resonances, a small amount of stable hadrons, which all form the hadronic component of the shower. Muons emerging from decaying mesons can traverse the atmosphere and arrive at the surface due to relativistic dilation of their life time, where they are measurable by ground based detectors.

To describe the inhomogeneous atmosphere in terms of traversed matter with which primary and secondary particles can interact, the vertical **atmospheric depth** is introduced:

$$X_v(h) = \int_h^\infty \mathrm{d}h' \, \rho(h') \quad , \tag{2.3}$$

with air density ρ at altitude h. The atmosphere has a total depth of about $1030\,\mathrm{g\,cm^{-2}}$ at sea level. For inclined showers the traversed depth depends on the incident angle ϑ and for $\vartheta \lesssim 60°$ is:

$$X(h, \vartheta) = \frac{X_v(h)}{\cos\vartheta} \quad . \tag{2.4}$$

2.2.1 Electromagnetic component

In terms of energy deposit the most important components of the cascade are electrons, positrons and photons, which carry about 85% of the total energy.

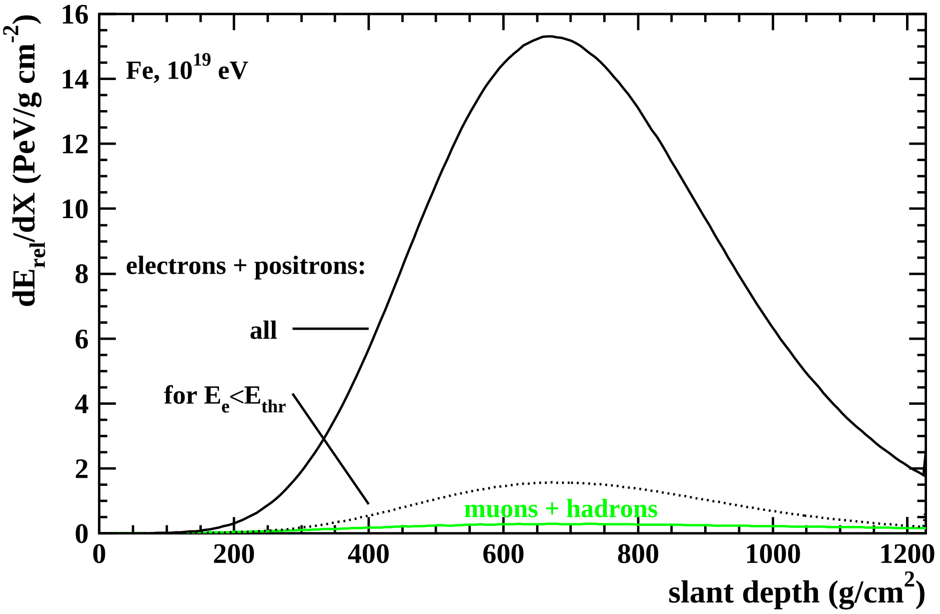

Figure 2.5: Energy deposit of electromagnetic and muonic+hadronic components. The dotted line indicates the energy deposit of secondary electrons and positrons with energy below $E_{\mathrm{thr}} = 0.1\,\mathrm{MeV}$. [19]

Apart from annihilation positrons behave similarly as electrons (which refer the both further on) and interact with the particles of the atmosphere via ionisation, bremsstrahlung - generating photons - and more infrequently knocking out delta-electrons. Produced photons above some MeV convert to electron-positron pairs via pair-production. As the processes transit into one another, an electromagnetic cascade develops parallel to the hadronic one. The cascade dies out, if the energy of the electrons fall below the critical energy E_c, where ionisation and radiation losses are equal. Hadronic cascades supply the electromagnetic component until they consume their own energy(cf. figure 2.6).

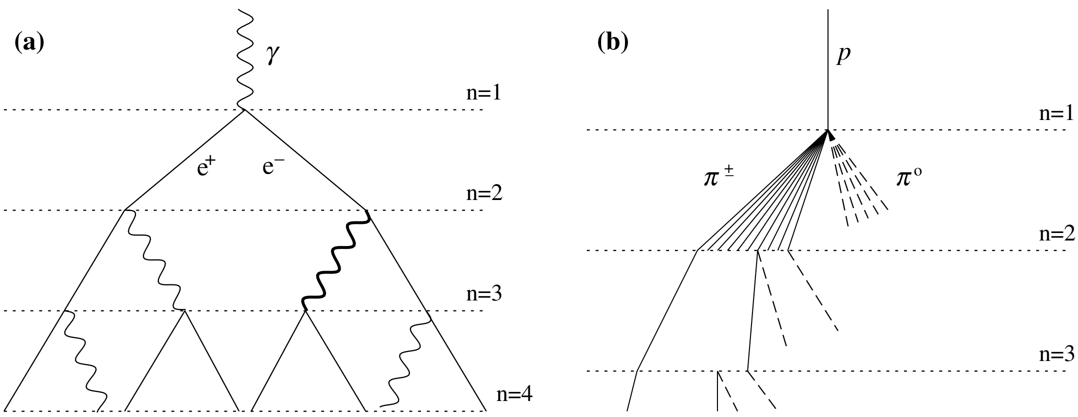

Figure 2.6: *Left*: Scheme of a electromagnetic cascade, which also can be initiated by electrons; n indicating the iteration index.
Right: same for hadronic cascade. Pion is representative also for other particles (see text). [20]

2.2.2 Heitler model

The cascade process is of stochastical nature, which can be understood by the simple Heitler model[21].

As the first particle with initial energy E_0 splits at the starting depth X_0 in two daughter particles both carrying the half of this energy. After a characteristic splitting length $\ln 2 \cdot \lambda_0$ this process starts over again n times. The radiatin length λ_0 depends on the process underlying the model (cf. λ_{em} below). At a depth X there are

$$N(X) = 2^{\frac{X}{\ln 2 \cdot \lambda_0}} \tag{2.5}$$

particles with energy $E(X) = E_0/N(X)$ each. The critical energy E_c imposes a limit on the maximum number of particles $N(X_{\text{max}}) = E_0/E_c$ - noting the linear dependence on initial energy - at the depth X_{max}, so this depth can be specified as:

$$X_{\text{max}} = X_0 + \lambda_0 \ln\left(\frac{E_0}{E_c}\right) \quad , \tag{2.6}$$

The typical interaction length for the electromagnetic cascade in air is $\lambda_{\text{em}} \approx 37\,\text{g}\,\text{cm}^{-2}$ [22] allowing up to about 30 lengths in the atmosphere for a typical shower. critical energy for electromagnetic cascades is $E_{\text{c,em}} \approx 85\,\text{MeV}$.

The Heitler-model describes the electromagnetic cascades well, but can also be extended to also approximate hadronic part of the shower. The hadronic interaction length is about $\lambda_{\text{h}} \approx 100\,\text{g}\,\text{cm}^{-2}$ and critical energy is $E_{\text{c,h}} \approx 20\,\text{GeV}$. For further details of the extension of Heitler-model to hadronic cascades see [20].

The superposition assumption states, that in a good approximation a primary consisting of a number of nucleons induces a shower of the same size, as the same number of superimposed proton showers of proportionally lower energy E_0/A [23], so together with equation 2.6 the relation 2.7 is gained:

$$X_{\text{max}}(E_0, A) \propto \ln\left(\frac{E_0}{A}\right) \quad , \tag{2.7}$$

2.2.3 Shower development

Air shower development driven by the subatomic processes described above is influenced by different random factors, primarily the first interaction height, but also stochastical interaction processes, so the position of the shower maximum can vary greatly even for the same primary, as seen in simulations in figure 2.7. The smaller fluctuation of iron showers is due to statistical averaging [3].

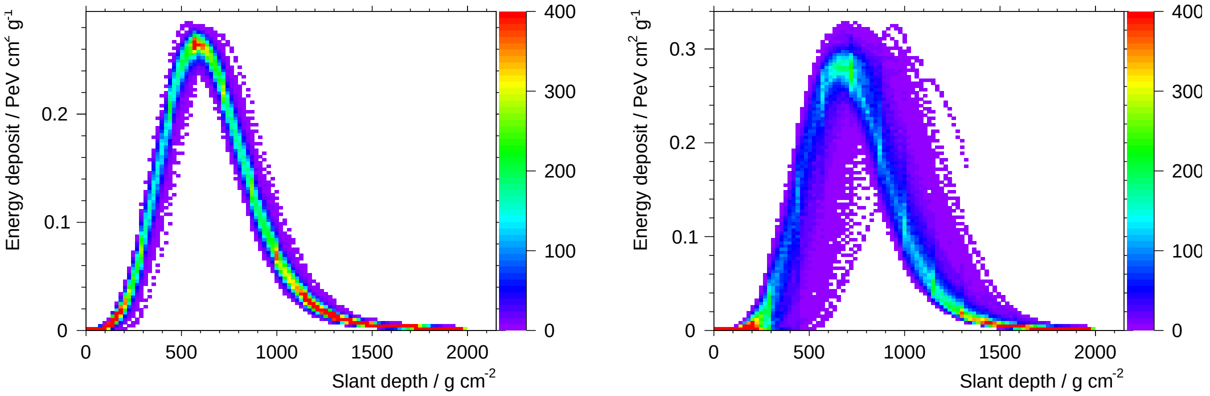

Figure 2.7: Air shower energy deposit profile fluctuations for iron (*left*) and proton (*right*). 1000 energy deposit profiles for each proton and iron are linearly superimposed. [24]

In data analysis the Gaisser-Hillas [25] formula 2.8 is used to describe the number of particles in an air shower for a given depth X

$$N(X) = N_{\max} \left(\frac{X - X_0}{X_{\max} - X_0}\right)^{\frac{X_{\max}-X_0}{\Lambda}} \exp\left(\frac{X_{\max} - X}{\Lambda}\right) \quad , \tag{2.8}$$

where $X_{\max}$ is mentioned above, N_{max} denotes the maximum number of particles during shower development, X_0 and Λ being fit parameters, related (but not identical [26]) to the starting depth of the shower and the shower decay length.

The number of particles given by this formula is related to the mean energy loss per particle being about $2.2\,\mathrm{MeV/\,g\,cm^{-2}}$. In real showers the secondary particles are not monoenergetic for a certain depth, as the simplified model suggests, but are distributed in energy over several orders of magnitude:

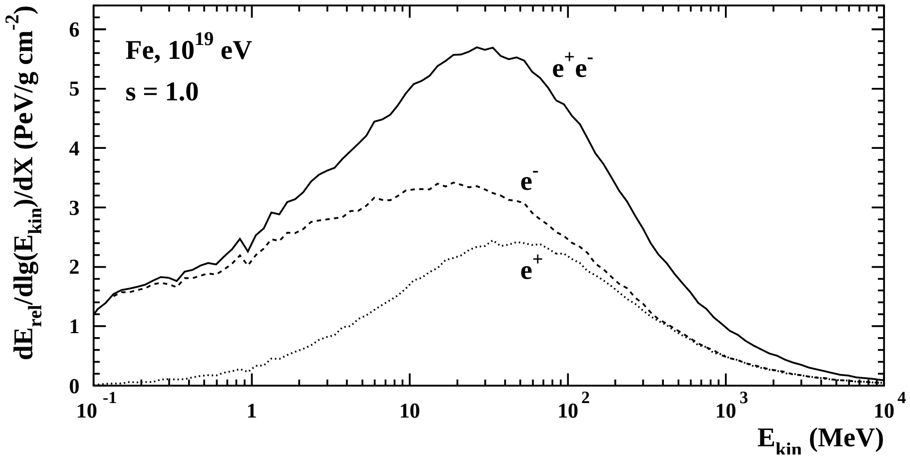

Figure 2.8: Distribution of energy release as a function of secondary particle energy for secondary positrons/electrons/both in an iron shower with $E = 1 \cdot 10^{19}\,\mathrm{eV}$ at $X_{\max}$. [19]

The shower age s used in figure 2.8 universally describes the shower development and is defined as

$$s := \frac{3X}{X + 2X_{\max}} \quad . \tag{2.9}$$

2.3 Light production

In air showers charged secondary particles produce light in the atmosphere through two mechanisms, which are reviewed below: fluorescence and Cherenkov effect. This light is measurable for detectors on the ground [27] such as the Pierre Auger Observatory and is thought even to be measurable from an orbit [28].

2.3.1 Fluorescence light

Secondary particles, if they are not decaying or their energy is too low to take part in cascades, passing through the atmosphere loose their energy primarily by means of ionisation and molecular excitation described by the Bethe-Bloch formula [14]. After excitation the air molecules, being mostly dinitrogen, emit ultraviolet light isotropically according to the wavelength spectrum shown in figure 2.9.

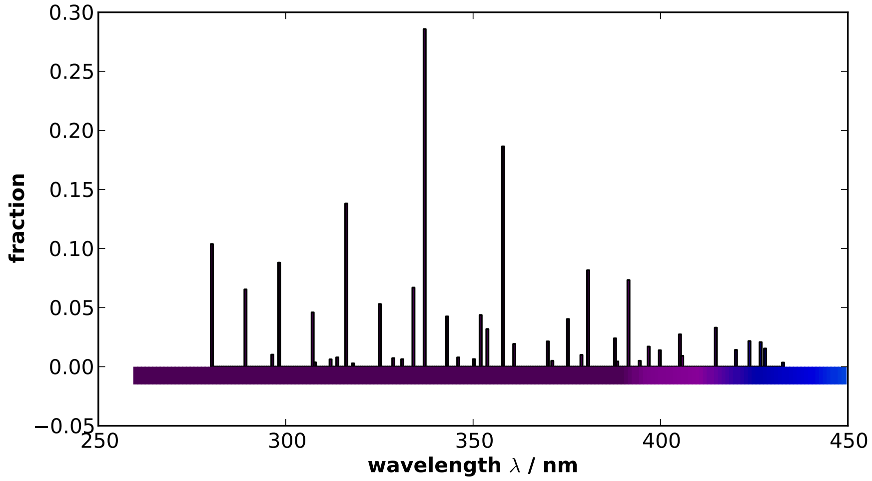

Figure 2.9: Measured spectrum of nitrogen fluorescence light between 250 nm and 450 nm at the detector aperture. Courtesy of Tim Niggemann, based on [29]

The number of produced fluorescence photons by secondary electrons is proportional to the deposited energy and traversed distance in air (between 4 and 6 photons per MeV [30, 31, 32] and nearly 4 photons per meter for electrons at $\lambda = 337\,\mathrm{nm}$). These photons are emitted isotropically and can be detected by optical instruments.

In an air shower the emitted fluorescence light per slant depth can thus be calculated as [33]:

$$\frac{\mathrm{d}^2 N_f}{\mathrm{d}X \mathrm{d}\lambda} := \iint \mathrm{d}E\, Y(\lambda, p, T, u, E_e)\, \frac{\mathrm{d}N_e(X)}{\mathrm{d}E}\, \frac{\mathrm{d}E_{dep}}{\mathrm{d}X} \quad , \tag{2.10}$$

with atmospheric pressure p, temperature T, humidity u, wavelength λ and electron energy dependent light yield Y, energy spectrum of the electrons $\mathrm{d}N_e/\mathrm{d}E$ and energy deposit $\mathrm{d}E_{dep}/\mathrm{d}X$ in this atmosphere layer.

Measurement of the fluorescence light gives full information about the number of charged particles and deposited energy at certain height and is used to measure the longitudinal development of the shower, further on also called shower profile, described by equation 2.8.

2.3.2 Cherenkov light

Another source of light in air showers is the Cherenkov effect. Charged secondary particles, which travel through the medium, deflect negatively charged electron shells and partially polarize atoms around them, compare left figure 2.10, though net polarisation in front and behind the particle is negligible. Moving faster than the speed of light in the medium allows the polarisation to drag

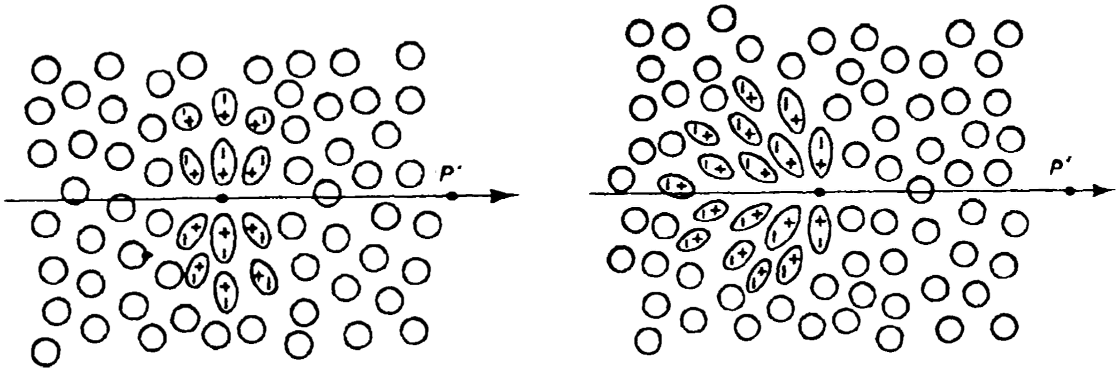

Figure 2.10: Polarisation of a medium while a charged particle P is traversing from left to right at speed v below $\frac{c_0}{n}$ (*left-hand side*) and above $\frac{c_0}{n}$ (*right-hand side*) [34]

behind the particle (compare right figure 2.10), releasing Cherenkov photons in the direction of the particle trajectory under angle θ_C , if the condition 2.11 applies:

$$\cos\theta_C = \frac{1}{\beta n} \Rightarrow \beta > \frac{1}{n} \quad , \tag{2.11}$$

where β is the relativistic speed of the particle, n the refractive index of the medium and θ_C the Cherenkov angle.

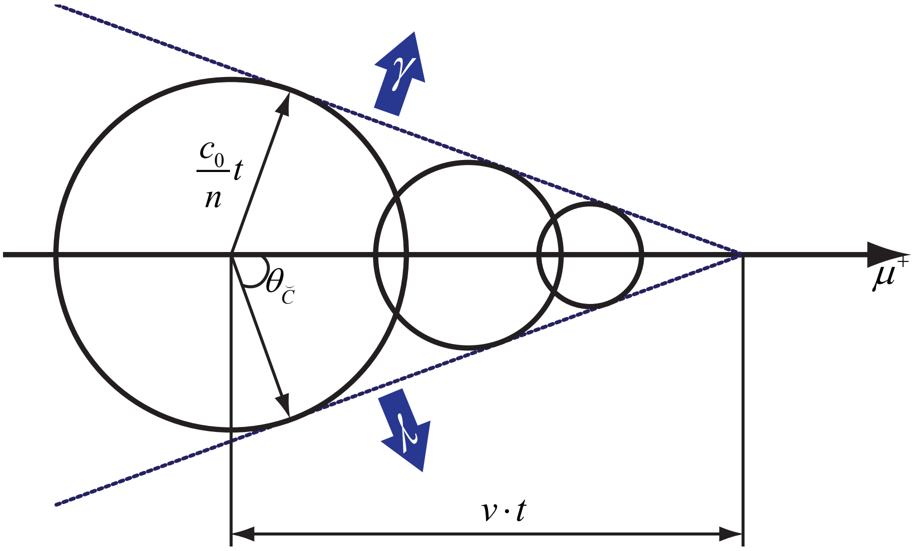

Figure 2.11: Huygens' construction is used to illustrate the Cherenkov-condition. The particle (muon) is traversing the distance $v \cdot t$ from left to right, while an elementary wave travels the distance $\frac{c_0}{n}t$. Constructive superposition is possible only at the angle θ_C, which is defined as $\cos\theta_C = \frac{c_0}{vn}$.

In air at sea level the Cherenkov angle is about 1.4° and decreases for higher altitudes. In the atmosphere the Cherenkov condition is satisfied for different particles according to figure 2.12 and energy threshold $E_{\min} = \frac{m\,c^2}{\sqrt{1-n^{-2}}}$.

A theoretical description of the effect is given e.g. in [34]. The number of photons produced per unit length is described with the Frank-Tamm formula [35]:

$$\frac{\mathrm{d}^2 N_\gamma}{\mathrm{d}x\mathrm{d}\lambda} = 2\pi\alpha z^2 \frac{1}{\lambda^2}\left(1 - \frac{1}{(n(\lambda)\beta)^2}\right) \quad , \tag{2.12}$$

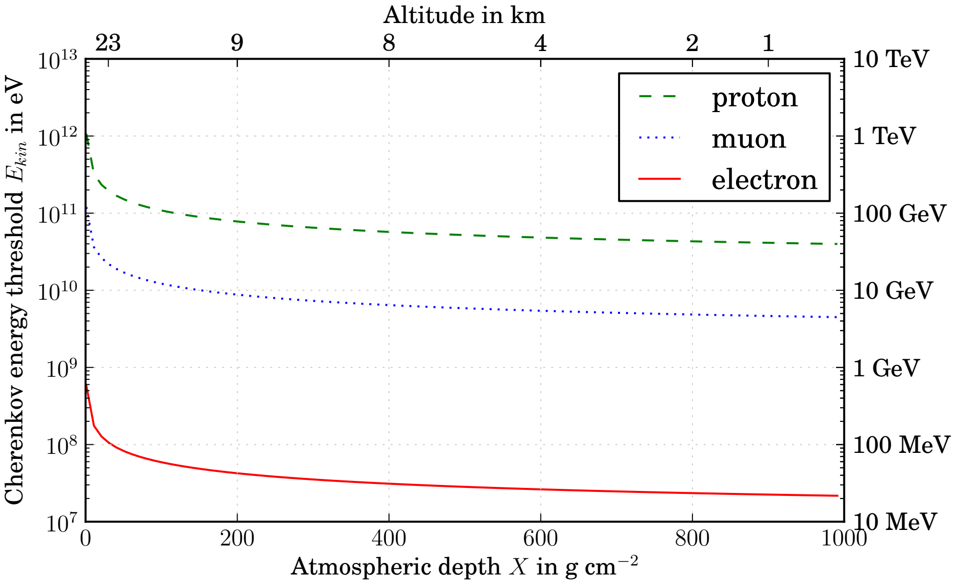

Figure 2.12: Kinetic energy threshold for Cherenkov effect for different particles with simplified atmosphere parametrization according to [36].

with wavelength of the Cherenkov photons λ, $z = 1$ charge number of traversing particle and $\alpha \approx 1/137$ fine-structure constant. The λ^{-2} dependence causes the continuous spectrum to increase towards shorter wavelengths.

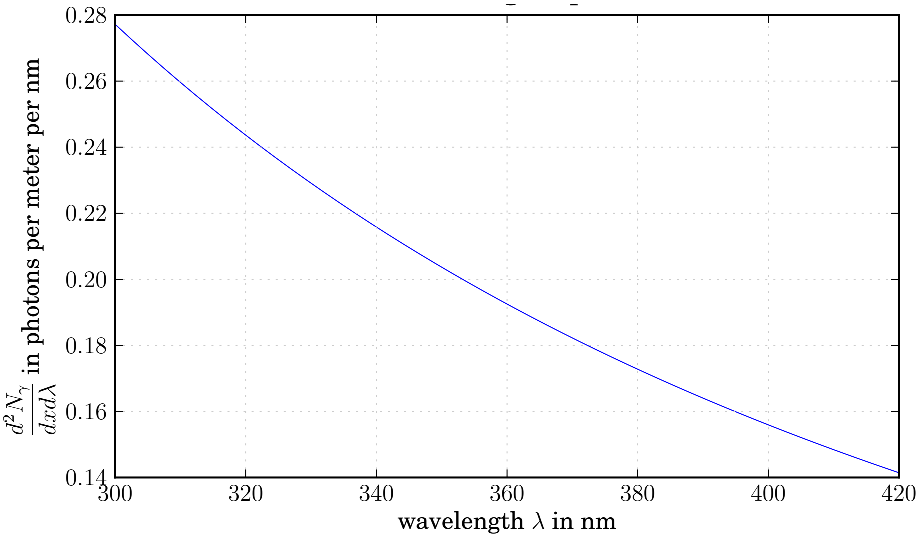

Figure 2.13: Cherenkov light yield for a single 50 MeV electron in air at sea level [37].

Photons produced in air showers are usually described in terms of slant depth, defining the Cherenkov yield y_γ in a wavelength region $(\lambda_1..\lambda_2)$:

$$y_\gamma := \frac{\mathrm{d}N_\gamma}{\mathrm{d}X} = \frac{1}{\rho(h)} \int_{\lambda_1}^{\lambda_2} \mathrm{d}\lambda \, \frac{\mathrm{d}^2 N_\gamma}{\mathrm{d}x\mathrm{d}\lambda} \quad . \tag{2.13}$$

As secondary particles undergo multiple scattering, they diverge from the shower axis, so direct Cherenkov light, despite of its narrow emittance angle is detected at considerable distances from the axis of the air shower (cf. figure 4.8 on page 26).

For single showers the maximum of Cherenkov photons production lies lower in the atmosphere than X_{max} of the fluorescence light as in the example shower in figure 2.14, which could cause the bias.

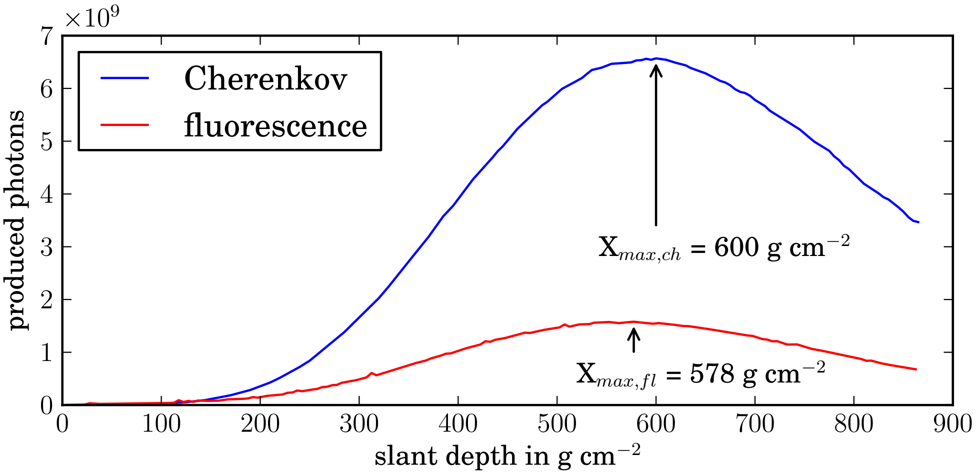

Figure 2.14: Cherenkov light production profile calculated by CORSIKA, fluorescence light profile calculated using [32] of a single vertical CORSIKA shower. Invisible energy carried by neutrinos is not accounted for.

2.4 Light attenuation

For light produced in air showers two major processes in the atmosphere deflect it from its direct path to a detector (cf. [38]).

Rayleigh scattering occurs when light scatters off particles smaller than the wavelength of the light. The angular distribution of scattered photons N_γ can be calculated as follows:

$$\frac{\mathrm{d}^2\mathrm{N}_\gamma}{\mathrm{dXd}\Omega} \propto \left| \frac{N_\gamma}{X_R} \left(\frac{400\,\mathrm{nm}}{\lambda} \right)^4 \right| (1+\cos^2\theta) \quad , \tag{2.14}$$

with $X_R = 2970\,\mathrm{g\,cm^{-2}}$ the scattering mean free path at 400 nm. Rayleigh scattering does not change the wavelength and distributes the radiation in all directions with respect to the shower axis due to its weak angular dependence and it is important for forward directed Cherenkov light.

Mie scattering occurs on spherical particles, in case of atmosphere mostly aerosols, which size is of the same order as the light wavelength. The common general approximation assumes an exponential decline with altitude as in (2.15) and strong forward peaked as in (2.16):

$$\frac{\mathrm{dN}_\gamma}{\mathrm{dx}} \approx -\frac{N_\gamma}{l_M} \exp\left(-\tfrac{h}{h_M}\right) \quad , \tag{2.15}$$

$$\frac{\mathrm{dN}_\gamma}{\mathrm{dxd}\Omega} \approx a\,\exp\left(-\tfrac{\theta}{\theta_M}\right) \cdot \left| \frac{\mathrm{dN}_\gamma}{\mathrm{dx}} \right| \quad , \tag{2.16}$$

with $a = 0.8$, $\theta_M = 26.7^\circ$, aerosol scale height $h_M \approx 7.5\,\mathrm{km}$ at Auger site, Mie scattering mean free path $l_M \approx 14\,\mathrm{km}$.

3 Pierre Auger Observatory

The Pierre Auger Observatory aims to measure cosmic ray spectrum, composition and arrival directions at energies above 10^{18} eV. The site is situated in Malargüe, in the province of Mendoza, Argentina, with area of about $3000\,\mathrm{km}^2$

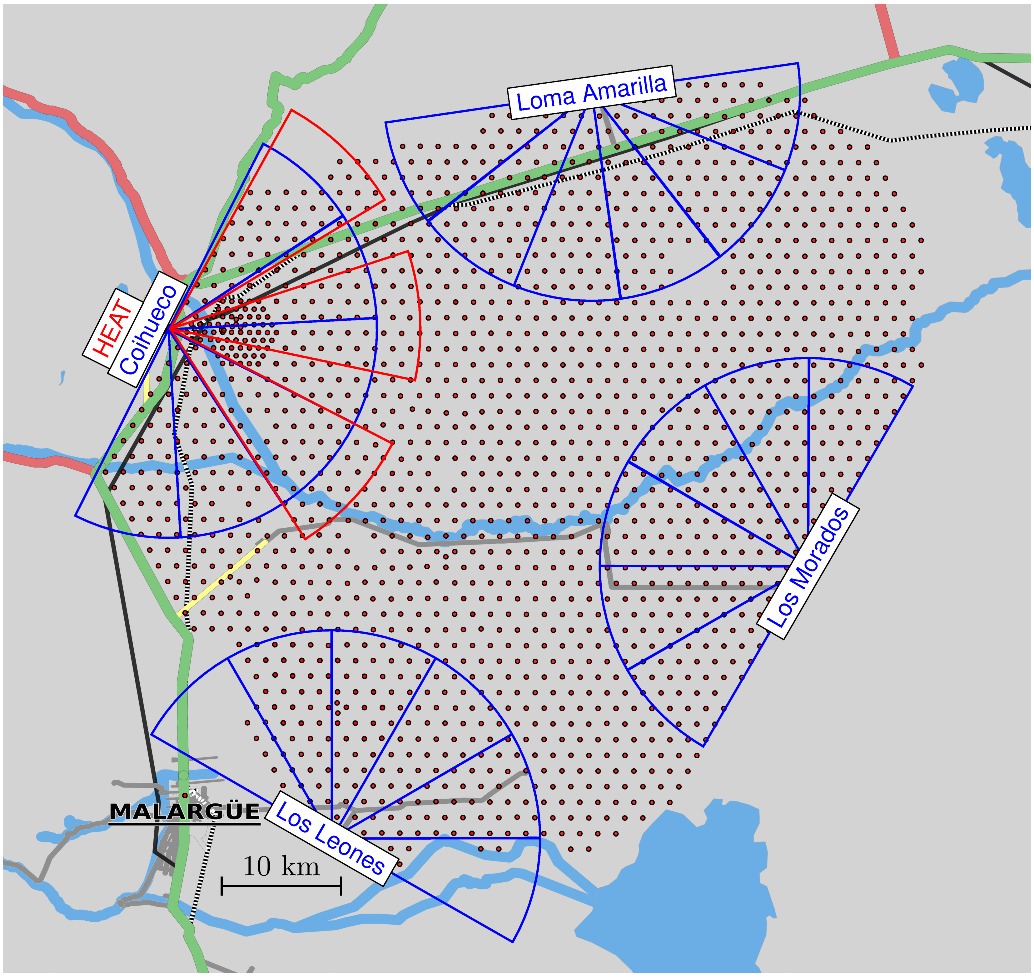

Figure 3.1: Schematics of the array overimposed on the map of the region around Malargüe. The red dots point to the positions of the surface detectors, the blue/red lines are field of view projections of fluorescence telescopes. Courtesy of Marcel Straub, [39]

It consists of two major components. *a*) The area instrumented with surface detectors and *b*) fluorescence telescopes overviewing the array. The observatory combines two detection techniques of sampling the particles of the shower arriving at the ground and collecting the light produced in the atmosphere as in figure 3.7. Several enhancements were installed in the past years, one of these are the three High Elevation Auger Telescopes (HEAT) which extend the FD and are discussed in detail below, the INFILL and HEATLET arrays are integrated into the surface detector, AERA allows for radio detection.

This chapter gives a brief outline of the different detector components.

3.1 Surface detector

The most prominent feature in the image 3.1 is the surface detector array - further on called SD. It consists of 1660 units arranged on a hexagonal grid with a spacing of 1.5 km, apart from the sub-array INFILL which has a spacing of 0.75 km. Each station is a water cherenkov detector depicted in figure 3.2 right.

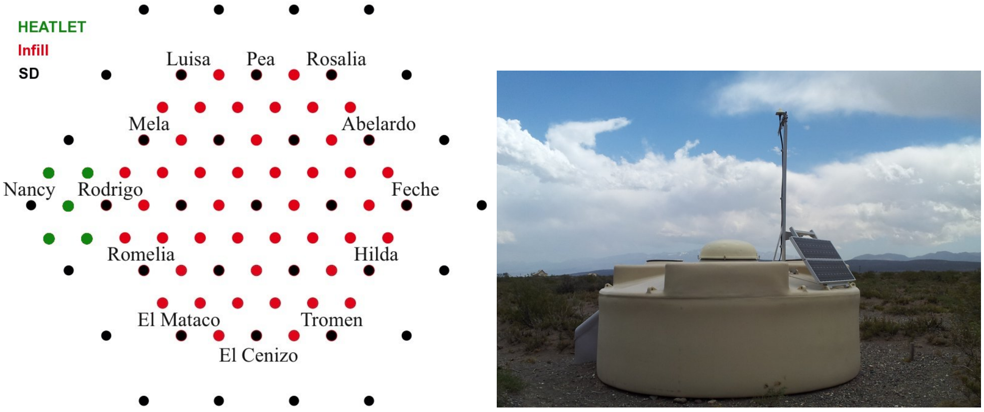

Figure 3.2: *Left*: Sketch of the Infill array and HEATLET stations. SD stations are marked black , the Infill stations red and HEATLET green. (based on [40])
Right: Single SD station

One tank is filled with 12000 liters of high purity water. The polyethylene shell is of 3.6 m diameter and 1.55 m high. Secondary particles produce Cherenkov light inside the water, which is equipped with three photomultiplier tubes (PMT). Each station is equipped with a GPS antenna for time measurements and is connected to the central data aquisition (CDAS) via wireless link. The solar panel and rechargeable battery ensure autonomous operation.

Figure 3.3: Row of surface stations as seen from Coihueco

The duty cycle of the SD is near 100%; unlike FD it can be operated during daylight hours. It detects showers with energies above $E = 3 \cdot 10^{18}$ eV at full efficiency, sampling the lateral distribution of particles. If coincident signals for one station reach a threshold, a T1 first level trigger is generated. For lower energy showers the timing information for single detectors is made available for FD.

The Infill array is installed near Coihueco with half of the spacing of the SD to lower the energy threshold for SD showers down to $E = 1 \cdot 10^{17}$ eV. HEATLET stations were deposited closer to HEAT and Coihueco locations using the smaller Infill-spacing to increase trigger rates of low energy showers measured by both FD and SD.

3.2 Fluorescence detector

The fluorescence detectors (FD) are situated at four locations around the array (cf. 3.1) - denoted as Los Leones (LL, south), Los Morados (LM, east), Loma Amarilla (LA, north) and Coihueco (CO, west) together with HEAT. These stations are called eyes.

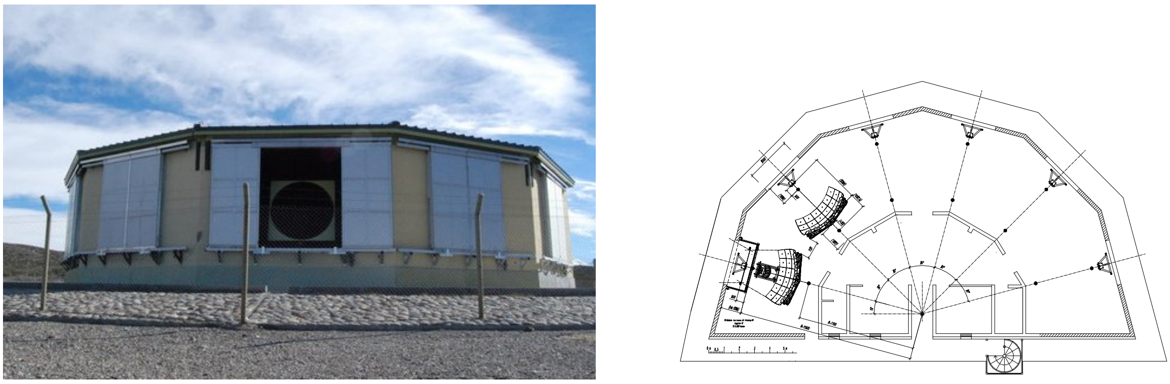

Figure 3.4:
Left: Front view of one FD building with open shutter and visible aperture.
Right: Schematic top view of one of four FD buildings. The six single telescopes are arranged beside each other [41].

The four initial FD buildings consist each of six reflective Schmidt-telescope bays as in figure 3.5. These consist of an 1.1 m radius aperture with lens and UV filter, a large spherical mirror of about 3.5 m diameter and a camera consisting of 20 × 22 hexagonal PMTs, also called pixels. Each cell views 1.5° × 1.5° of the sky, so that one telescope has a field of view of 28.6° in elevation and 30° in azimuth. Each eye covers 180°in azimuth.

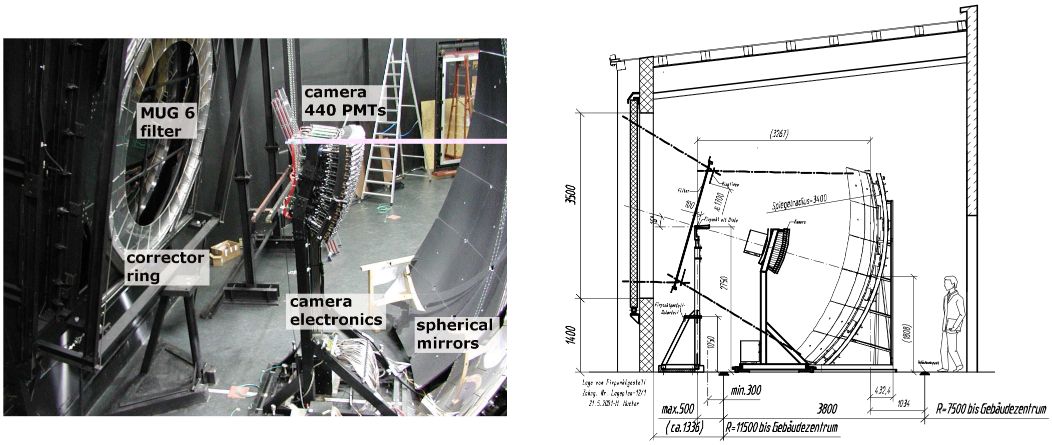

Figure 3.5: *Left*: Telescope constituents from inside [42], *Right*: Schematic drawing of a single telescope [41].

Each PMT is read out and digitized with a 10 MHz sampling rate (respectively 100 ns time binning). The light flux over time and pixels is then calculated using the absolute calibration.

The detector is operated in moonless and cloudless nights, which restricts the duty cycle to about 13%. A detailed description of the telescopes is done in [43].

The detector is sensitive to photons with wavelenghts between 300 nm and 420 nm(cf. figure 3.6) and is optimized for fluorescence light detection. In reconstruction (cf. section 4.4, page 21) the detected light is mapped back to the shower development.

The First Level Trigger (FLT) electronics monitors the pixels for signal above a certain threshold compared to the night sky with set trigger rate of about 100 Hz. Upon several pixels triggering within 20 μs a signal is prestored and the Second Level Trigger (SLT) looks for five neighboring coherent pixels arranged in a straight track indicating a shower track with a usual rate of about

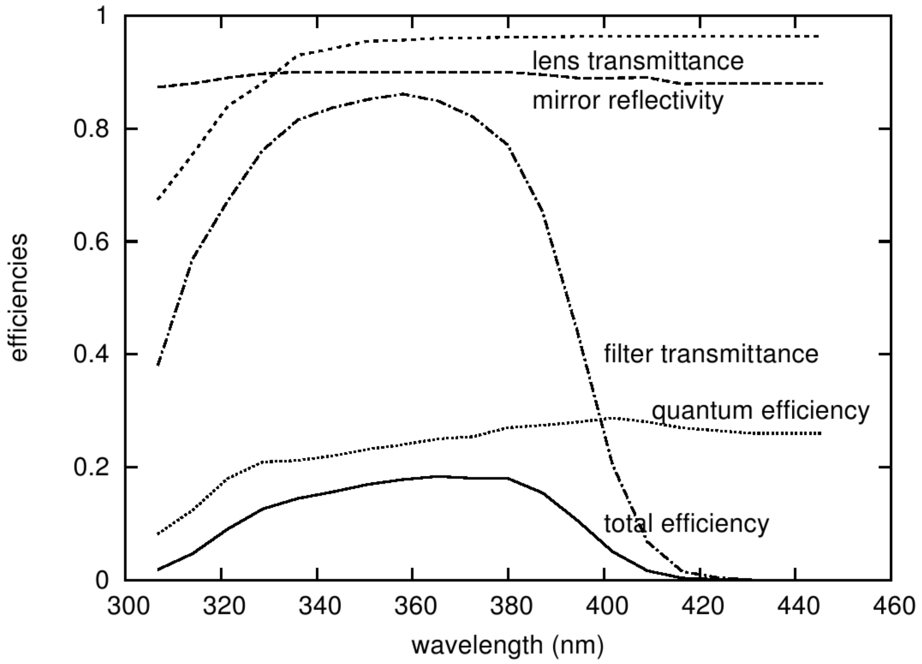

Figure 3.6: Light efficiency of the entire optical system including aperture, mirror and PMTs, as a function of wavelength [44].

one per minute. In the Third Level Trigger (TLT) all the phenomena, such as lightnings and direct muons, are rejected, if their duration is less than 400 ns or more 100 μs. The final T3 algorithm performs a fast reconstruction of the shower based on all telescopes for one eye. These events are sent to CDAS, where the SD stations in the region of interest are forced to be read out, so that the impact time on the ground can be reconstructed better.

The fluorescence detectors are capable of sampling the longitudinal profile of the shower, but if the same shower is also measured with the SD the so called HYBRID DETECTION is achieved as shown in figure 3.7.

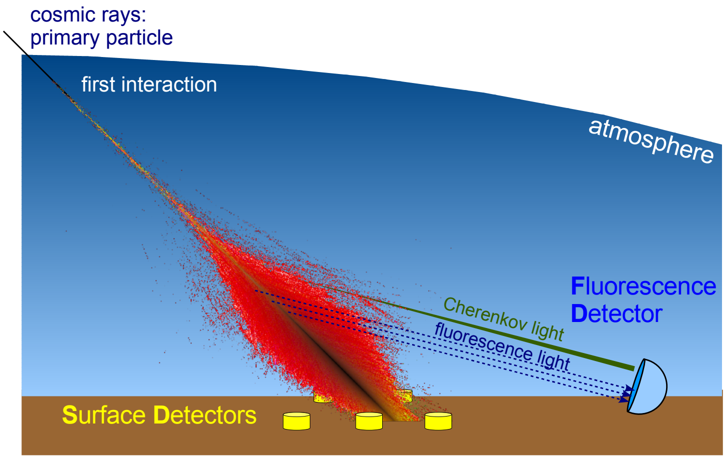

Figure 3.7: Hybrid detection of the shower - lateral extension is sampled with the SD, the longitudinal profile is measured with the FD [45].

3.3 Enhancements

The Pierre Auger Observatory is a unique site, where also other detection methods are introduced and combined.

3.3.1 Radio detection

The newest detection technique at the site exploits coherent radiation of air showers in the $10 - 100\,\mathrm{MHz}$ band. For this purpose 21 antennas (cf. 3.8) are already installed and 160 planned at the area of Infill, they constitute the Auger Engineering Radio Array (AERA). The array is self-triggering and has already detected coincident events with FD and SD. Radio signals contain information about the shower development, also it will be possible to achieve 100% duty cycle, so radio technique will join advantages of the other detection methods.

Figure 3.8: One AERA antenna near central data aquisition ANEXO

3.3.2 HEAT

It is supposed, that in the energy range between $E = 1 \cdot 10^{17}\,\mathrm{eV}$ and $E = 1 \cdot 10^{18}\,\mathrm{eV}$ the transition of galactic to extragalactic cosmic ray origin takes place.Showers with energies below $E = 1 \cdot 10^{18}\,\mathrm{eV}$ are developing higher in the atmosphere as well as emitting less light and are visible at distances below 10 km, so that the four standard eyes usually cannot fully detect these due to their limited field of view, as shown in figure 3.9.

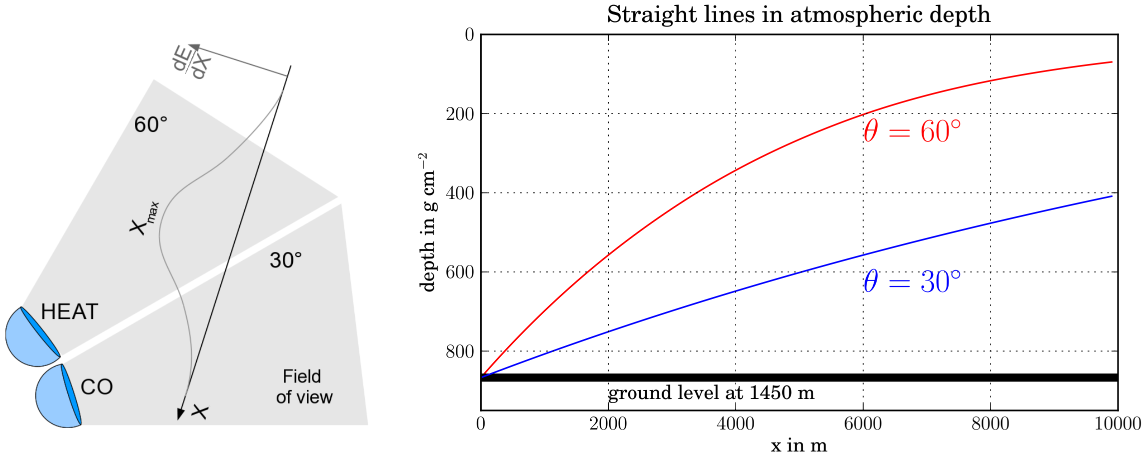

Figure 3.9: *Left*:Visualization of HEAT and Coihueco fields of view. *Right*: Fields of view in atmospheric depth units. US standard atmosphere parametrisation [46] is used.

The low energy enhancement for the FD are the High Elevation Auger Telescopes (HEAT). These three telescopes – separately also called bays– are installed at a distance of about 200 m from Coihueco and, as depicted in figure 3.10, have a field of view tilted by 29° in elevation allowing them –in combination with regular FD telescopes– to sample more of the shower development, and especially the position of $X_{\max}$, for nearby showers.

HEAT can be tilted telescope-wise from “downward” mode, which results in the same field of

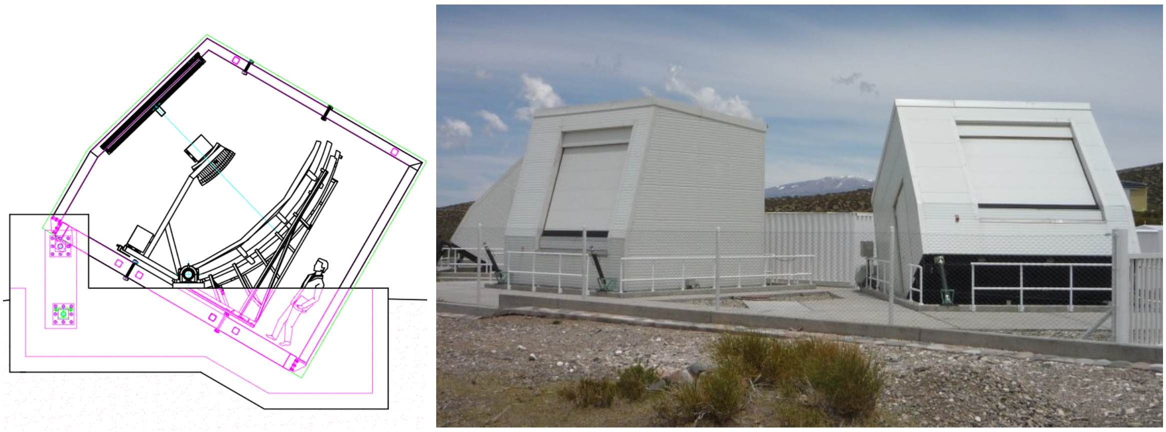

Figure 3.10: *Left*: Schematic side-view of a single tilted bay [40]
Right: Three High Elevation Auger Telescopes (HEAT) - bays 1, 2 and 3 (obscured). The bay 2 is in "downward" mode.

view as for Coihueco, to its "upward", design mode see figure 3.10. The tilting is monitored as described in [47].

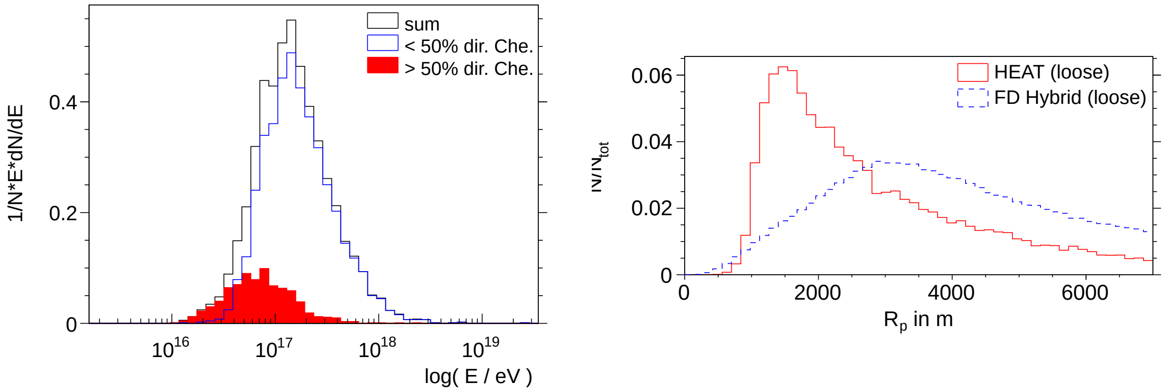

Figure 3.11: *Left*: Energy distribution of HEAT only dataset after loose cuts, separated into Cherenkov light fractions of more and less than 50%. Allowing higher Cherenkov light fraction showers, lower energy events can be recorded. *Right*: Distance to closest point of the shower axis (cf. 4.4) for HEAT only and standard FD hybrid showers. HEAT measure closer showers due to elevated field of view.

Due to the new field of view shower geometries are visible for the eye in a different way. Forward directed Cherenkov light of showers pointing towards the telescope is more abundant and contributes significantly to the detected light changing the FD trigger probability (cf. [48]) as well as the shower reconstruction 4.4.

The optical and electrical design is very similar to those described in section 3.2. The sampling rate has been increased by the factor of two, resulting in a time bin size of 50 ns. The cross-calibration with Coihueco in downward mode of HEAT was performed to determine preliminary calibration constants on telescope basis and is currently used in place of the absolute calibration.

The reconstructed HEAT data is made available by Marcel Straub for the period between 07.2009 and 10.2011.

4 EAS simulation and reconstruction

An important tool to study air shower are Monte-Carlo (MC) simulations, which model the showers development in the atmosphere.

4.1 Monte-Carlo software

4.1.1 CONEX

For high level analyses of shower parameters the simulation library compiled by Nils Scharf in the course of his PhD thesis [47] is used. The showers are generated with CONEX [49], where first high-energy interactions are tracked in detail, whereas the further shower development is approximated by numerically solving cascade equations, by which the one dimensional longitudinal profile of energy deposit is gained. To equally consider the available hadronic interaction models the arithmetic mean over the models is used in this work - QGSJET-II [50], Sibyll [51] and EPOS [52].

4.1.2 CORSIKA

A program for the detailed simulation of particles in an air shower is CORISKA (COsmic Ray SImulations for KAscade) [53, 54]. In the simulation secondary particles are tracked until they reach the ground. The major aspect for this code is the capability of CORSIKA to simulate Cherenkov light.

CORSIKA is organized in a Fortran framework, which handles the in- and output of data, particle decays, energy deposit, atmosphere parametrization and magnetic field of the Earth. It also integrates hadronic interaction models, in this study QGSJET-II for higher and FLUKA [55] for lower energy are used. The electromagnetic interactions are simulated using the default NKG formulae [56]. The Cherenkov option is developed by the HEGRA Collaboration and K. Bernlöhr [57].

CORSIKA code tracks single secondary particles after their production taking into account their interactions, decays and energy deposit. As their energy falls below a given threshold, multiple particles are combined to one representative particle with an appropriate weight. The technique is called thinning and is controlled by the parameter $\eta_{\mathrm{th}} = E_{\mathrm{thin}}/E_0$ ($\eta_{\mathrm{th}} = 10^{-6}$ is used in this work) and the maximum weight of a thinned particle $w_{\max}$ (10^6 is used). The simulation results are a thinned longitudinal profile, the lateral particle distribution and Cherenkov light photons on the ground. Steering cards and further details of shower generation for this study are given in section A.3.

The coordinate systems are summarized in figure 4.1. In contrast to the x-axis pointing to the East in Auger coordinates, CORSIKA uses the geomagnetic north for its x-axis. The current direction of the magnetic field pointing in Malargüe is used [58]: $2°31'2"$ declination eastwards, $35°40'26"$ inclination and $24.3\,\mu$T absolute magnitude.

4.2 $\overline{\text{Off}}\underline{\text{line}}$ framework

$\overline{\text{Off}}\underline{\text{line}}$ is the software framework developed by the Pierre Auger Collaboration for handling the cosmic ray air shower data structures. It is used for the reconstruction of both the data recorded by the observatory, but also for detector simulation of Monte-Carlo showers, since it incorporates detector description, and processes the data in module sequences (e.g. in section A.2). Parts of the framework are utilizable independently, for example shower data files interpreter libraries

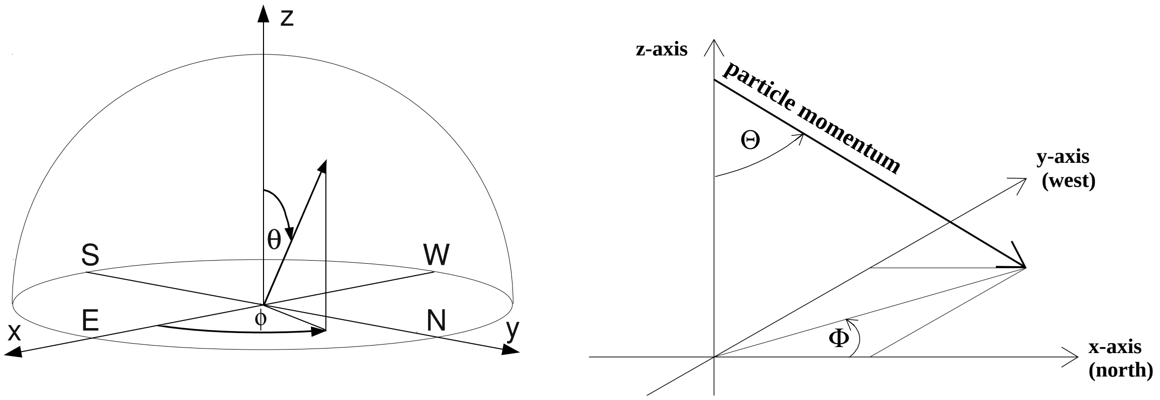

Figure 4.1: Coordinate system definitions of *Left*: Auger [59] and *Right*: CORSIKA [54] . φ (Φ in CORSIKA, ϕ in Offline) denotes the shower azimuth, ϑ (Θ in CORSIKA, θ in Offline) denotes the zenith angle. The x-axis points to geographical east in Auger, and to geomagnetic north in CORSIKA as also shown in 4.8.

for reading ADST files, operations with and manipulation of basic geometrical entities used in 4.5 or coordinates transformations.

4.2.1 Detector description

The physical and electrical properties of the detector are incorporated into the framework. Offline uses a modular structure which can be controlled by XML steering cards. One of the significant changes concerning HEAT is the introduction of the so called VIRTUAL EYE, a combination of two or more existing eyes in a new single one. The CoHE-eye incorporates Coihueco and HEAT data. Each physical eye separately would sample the shower development only partially, combined measurement allows for full reconstruction as shown in figure 4.2. In the following the example event no. SD11699524 is used.

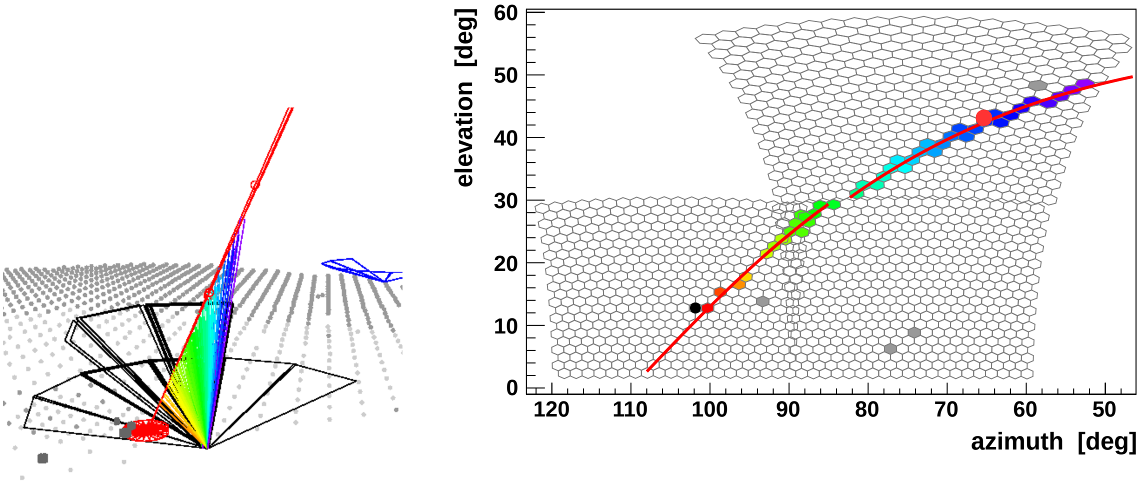

Figure 4.2: *Left*: Shower as seen by Coihueco (lower 3 field-of-view segments) and HEAT (3 upright telescopes). Coloured lines are single pixel directions towards the shower axis, which is shown in red. The colour-code represents timing information of the light trace from red to blue. Triggered SD stations are scaled in size according to measured signal, compared to uninvolved stations. *Right*: Trace of the shower with colour-coded arrival time as seen in HEAT (top) and Coihueco (bottom) combined to COHE. The shower axis for COHE (as well as separate axes for each HEAT and Coihueco eyes) is fitted to the trace and $X_{\max}$ is determined to be at the red marker.

4.3 Shower simulation

A shower geometry and an energy deposit profile are required to simulate the detector response to a Monte-Carlo shower in Offline. The used module sequence (A.2) is described closely following [60].

4.3.1 Monte-Carlo showers in Offline

EventFileReaderOG reads the output of several simulation programs , most notably CONEX and CORSIKA, and makes the required data available for the following modules of the framework. As showers are generated without specific impact point in the array, *EventGeneratorOG* specifies one or multiple shower *core* positions, generated from a list or placed randomly; additionally a desired time and date of the event is specified.

To simulate the hybrid detector response the *SdSimpleSimKG* is used, where according to the impact point of the shower the nearest surface station is set to be triggered and the GPS time of the SD trigger is calculated. After the initialization of the SD information the internal infrastructure of the fluorescence detector is initialized in the *FdSimEventCheckerOG*.

4.3.2 Light simulation and propagation

In the *ShowerLightSimulatorKG* fluorescence and Cherenkov photons are generated along the shower axis. All further calculations are performed within the wavelength band determined by the detector response. The energy deposit profile is directly converted to fluorescence photons using the light yield (cf. (2.10)). The Cherenkov photons are simulated using a parametrization of Cherenkov yield for electrons above the Cherenkov threshold forming a light cone as they accumulate moving along the shower axis. The angular distribution of Cherenkov light is commonly parametrized as an exponential with the function of Cherenkov energy threshold as scaling angle (cf. [38]). The beam is attenuated by Mie and Rayleigh scattering.

In the *LightAtDiaphragmSimulatorKG* the shower segment in the field of view of the telescopes and arrival time of the light at the aperture are calculated and a reasonable geometry is ensured then the time binning is calculated. For the time range all light fractions are attenuated and tracked to the aperture through the atmosphere. The one-dimensional shower is blurred according to the mean lateral distribution of the energy deposit and timing spread in *ShowerPhotonGeneratorOG*. Currently the lateral distribution parametrization of the fluorescence light is also used for Cherenkov light.

4.3.3 Telescope response

The raytracing through the detector geometry from the edge of the diaphragm is performed in *TelescopeSimulatorKG*. As the detector is operated in a dimly lit environment, the *FdBackgroundSimulatorOG* simulates the ambient light from diffuse background, stars, milky way band, moon etc. The response of the photomultiplier tubes to the total calculated light flux is performed in *FdElectronicsSimulatorOG*, where the absolute calibration of the telescopes is used and the resulting signal is realistically smeared. As the absolute calibration for HEAT is currently being in preparation the cross-calibration with Coihueco is used instead (cf. [61]).

4.4 Shower reconstruction

The reconstruction of an air shower is a key step, common for simulated showers and detector data. The most important modules in the sequence used (as in A.2) are taken from [62] and are as follows:

4.4.1 Light allocation

In *FdCalibratorOG* the photons are calculated with the help of absolute calibration for each telescope. For the virtual eye CoHe light from constituting real telescopes is combined in *FdEyeMergerKG*. For each pixel the arrival time is calculated in *FdPulseFinderOG*. The *PixelSelectorOG* rejects time and angular isolated pixels.

4.4.2 Geometry determination

After all relevant pixels are found, the shower geometry is searched in two steps.

First the so called SHOWER DETECTOR PLANE (SDP) is determined in *FdSDPFinderOG*. This plane is defined to include the shower axis and the position of the eye as in figure 4.3. The normal vector $\vec{n}$ determining the SDP is found by minimizing χ^2 calculated as (4.1):

$$\chi^2 = \sum_{i}^{pixels} |\vec{n} \cdot \vec{r}_i|^2 \, w_i \quad , \tag{4.1}$$

where $\vec{r}_i$ is the pointing direction of a relevant pixel and w_i is a weight determined by the light amount in the i-th pixel. The angle to the ground is denoted as ϑ_{SDP} and the azimuthal angle w.r.t. the east as φ_{SDP}. The colored rays in 4.2 represent the pointing directions. Refinements are described in [63].

After finding the SDP the axis in the SDP is determined by *FdAxisFinderOG*. The axis of every shower is unambiguously defined by three parameters provided a known SDP: the angle χ_0 from the horizontal to the shower axis within SDP, the shortest distance R_p from the eye to the shower axis and time t_0 defined by the idealized shower front crossing the R_p reference point at the axis. These quantities are depicted in figure 4.3.

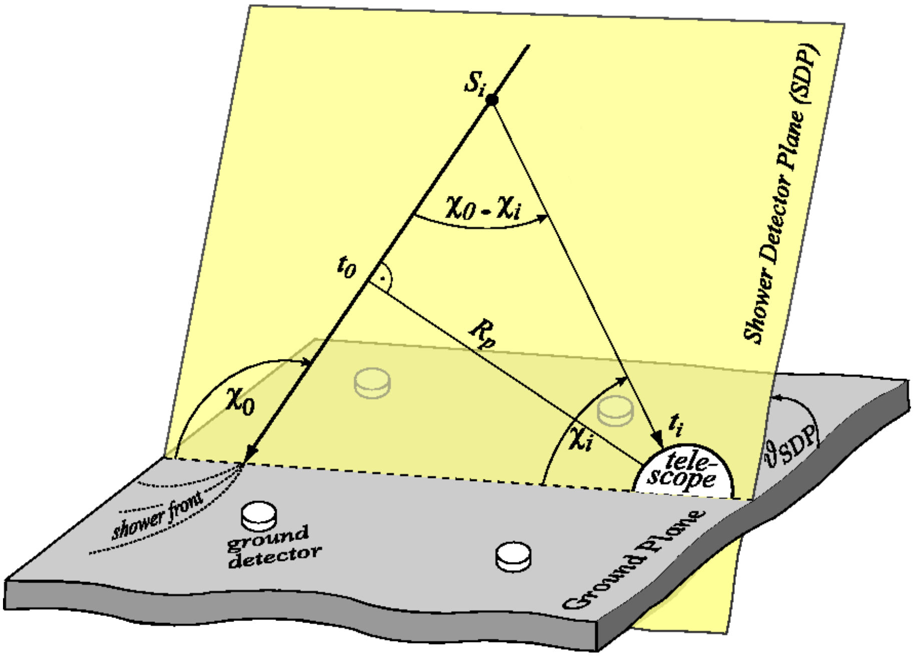

Figure 4.3: Sketch of the shower detector plane, three principal shower geometry parameters are defined as χ_0 - the angle from ground to shower axis in SDP, R_p - the shortest distance from eye to shower axis, t_0 - time of crossing of the R_p reference point by the idealized shower front. SDP is inclined with respect to the ground plane by angle ϑ_{SDP}. For every shower axis point S_i the arrival time at the aperture t_i and the arrival angle to the ground inside the SDP χ_i are measured [64].

To find the axis, geometrical considerations of the expected arrival time for photons emitted at the axis are used; from a point S_i of the shower axis light travels to the eye under angle χ_i in the SDP. The arrival t_i time is correlated with this angle via (4.2):

$$t_i = t_0 + \frac{R_p}{c} \tan\left(\frac{\chi_0 - \chi_i}{2}\right) \quad , \tag{4.2}$$

with the speed of light c. The axis is found by simultaneous fit with three free parameters on the FD timing and the SD impact time, if the SD trigger timestamp is available, also using the measured FD-SD time offset, due to physical light pathway delays and unequal signal processing. These steps are done in $HybridGeometryFinder$.

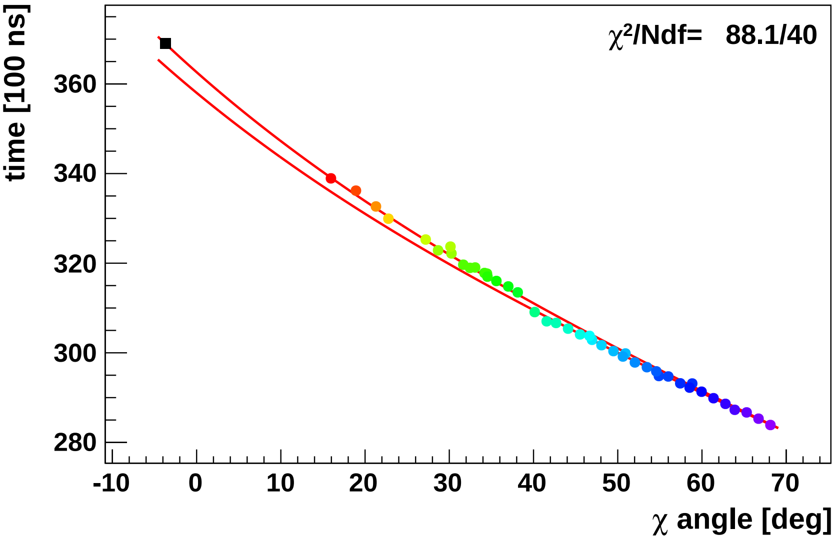

Figure 4.4: Time fit of arrival directions for determination of the shower axis. Timing is again color-coded, two fit functions correspond to HEAT and Coihueco points of view, black square is the time of SD trigger also used in the fit, HEAT data ranges approximately from 70° to 40° and Coihueco to 15°.

4.4.3 Determination of energy deposit

The $FdApertureLight$ module takes different light sources into account and the deposited energy per slant depth is calculated. Knowing the shower geometry allows to calculate the light from energy deposit based on a parametrization of the lateral distributions of fluorescence and Cherenkov light [65, 66] and parametrization of angular distribution of Cherenkov light [38]. The routine outlined here is detailed in [67, 68].

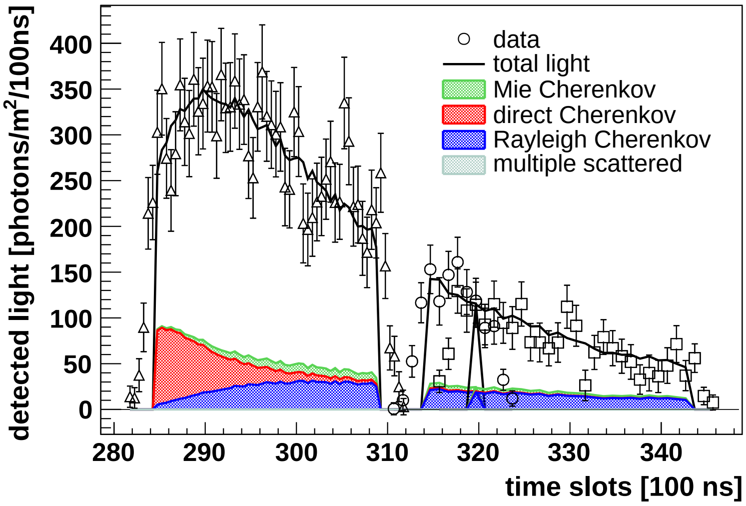

Figure 4.5: Light arriving at three telescopes (depicted in 4.2) over time is extrapolated beyond the mirrorcrossings. Different sources contributing are estimated from shower geometry.

For a given geometry every shower segment can be mapped to a certain slant depth and arrival time. The algorithm calculates the expected number of fluorescence and Cherenkov photons from both direct production and scattering processes depending on the number of particles and deposited energy, transforms it in matrix notation and solves it numerically.

Photons produced in slant depth segment X_i are isotropically distributed over a sphere with surface $4\pi r_i^2$, transmitted as a fraction T_i due to attenuation processes and are detected at the distance r_i with efficiency ε. Thus the factor $d_i = \frac{\varepsilon T_i}{4\pi r_i^2}$ is introduced. The fluorescence light flux y_i^f can be calculated as:

$$y_i^f = d_i \, Y_i^f \, w_i \, \Delta X_i \quad , \tag{4.3}$$

with fluorescence yield Y_i^f, ΔX_i the slant depth segment and w_i the energy deposit per slant depth. For direct Cherenkov light a yield for photons emitted at the β_i angle to the axis can be calculated:

$$y_i^{Cd}(\beta_i) = d_i \, f_C(\beta_i) \, Y_i^C \, N_i^e \, \Delta X_i \quad , \tag{4.4}$$

with $f_C(\beta_i)$ denoting the fraction of Cherenkov photons emitted towards the telescope, Cherenkov yield Y_i^C and N_i^e the number of electrons and positions above Cherenkov energy threshold at depth i. Maintaining the notation the Cherenkov light scattered towards the telescope can be calculated at depth i as:

$$y_i^{Cs} = d_i \, f_s(\beta_i) \sum_{j=0}^{i} \mathcal{T}_{ji} Y_j^C \, N_j^e \, \Delta X_j \quad , \tag{4.5}$$

where the sum accounts for the photons produced and accumulated between slant depths j and i, of which the fraction $\mathcal{T}_{ji}$ arrives at i due to attenuation and fraction $f_s(\beta_i)$ is scattered towards the detector.

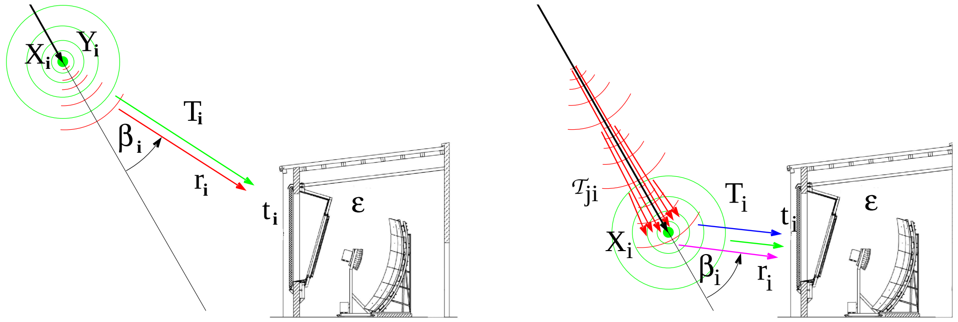

(a) *Direct light contribution.* (b) *Scattered light contribution.*

Figure 4.6: Illustration of the light flux arriving the telescopes. Color-coded are fluorescence light (green), direct Cherenkov light (red), scattered Cherenkov light - Rayleigh (blue) and Mie (magenta). The parameters are introduced in the text. [67]

A parametrization α_i can be introduced to transform the number of electrons to the respective energy deposit using universality of electron energy spectra in shower age (cf. [69]) as $w_i = N_i^e \alpha_i$. Therefore, it is possible to consider the sum of all light contributions (4.3) (4.4) (4.5) as a vector $\mathbf{y}$ indexed in depth steps which is related to the same-dimensional vector of energy deposit $\mathbf{w}$ over the FLUORESCENCE-CHERENKOV MATRIX $\mathbf{C}$ as

$$\mathbf{y} = \mathbf{C}\mathbf{w} \quad . \tag{4.6}$$

The matrix has the following structure:

$$C_{ij} = \begin{cases} 0, & i < j \\ c_i^d + c_i^s & i = j \\ c_{ij}^s & i > j \end{cases} \tag{4.7}$$

with entries found by comparison with the equations above:

$$c_i^d = d_i\,(Y_i^f\; +\; f_C(\beta_i)\,Y_i^C\,\tfrac{1}{\alpha_i}) \tag{4.8}$$

$$c_{ij}^s = d_i\,f_s(\beta_i)\,T_{ij}\,Y_i^C\,\tfrac{1}{\alpha_i} \tag{4.9}$$

By inverting the matrix an estimator of the energy deposit can be found numerically:

$$\hat{\mathbf{w}} = \mathbf{C}^{-1}\mathbf{y} \quad . \tag{4.10}$$

At this point Cherenkov light fractions can be estimated as ratio of direct and scattered Cherenkov light and total light arriving the aperture.

$$R_{c+cs} = \frac{N_c + N_{cs}}{N_f + N_c + N_{cs}} \ . \tag{4.11}$$

In this work the ratio of direct Cherenkov light only and total light is chosen to minimize influence of scattered light and is denoted as *direct Cherenkov light fraction* usually expressed in percent.

$$R_c = \frac{N_c}{N_f + N_c + N_{cs}} \ , \tag{4.12}$$

with N_c number of direct Cherenkov photons, N_{cs} number of scattered Cherenkov photons and N_f number of fluorescence photons at the aperture

4.4.4 Determination of shower parameters

In *FdEnergyDepositFinder* the Gaisser-Hillas function (2.8) is fitted to the measured energy deposit profile as in figure 4.7 with atmospheric depth of shower maximum X_{max}, atmospheric depth of the first interaction X_0, maximum energy deposit (corresponding to N_{max} in the formula) and mean free path Λ. The integral over the energy deposit is the calorimetric energy. The so called missing energy carried away by neutrinos and high-energy muons cannot be observed by telescopes and is accounted for in this step on the basis of simulations and hadronic interaction models. The correction is of the order of 10% [3].

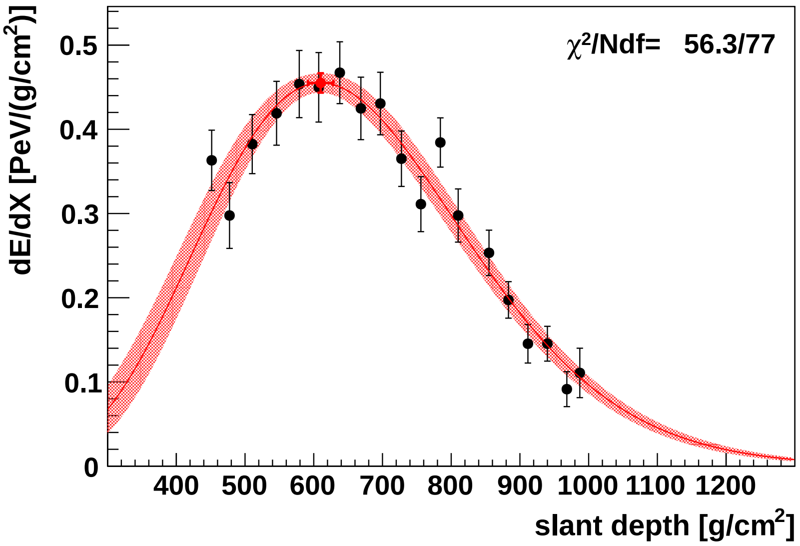

Figure 4.7: Gaisser-Hillas fit to the measured energy deposit in Coihueco and HEAT with statistical uncertainty band in red, and X_{max} at the top of the red curve (red marker).

4.5 Cherenkov photons simulated in CORSIKA

As an approach to cross-check the Cherenkov light simulation in Offline a method to extract detailed Cherenkov light information from CORSIKA was developed.

In CORSIKA Cherenkov photons are only recorded in a defined area. In the following a single proton shower of $E = 3.7 \cdot 10^{16}\,\mathrm{eV}$ simulated with QGSJET-II inclined by $\vartheta = 44°$ is shown. Corresponding photons are plotted in 4.8.

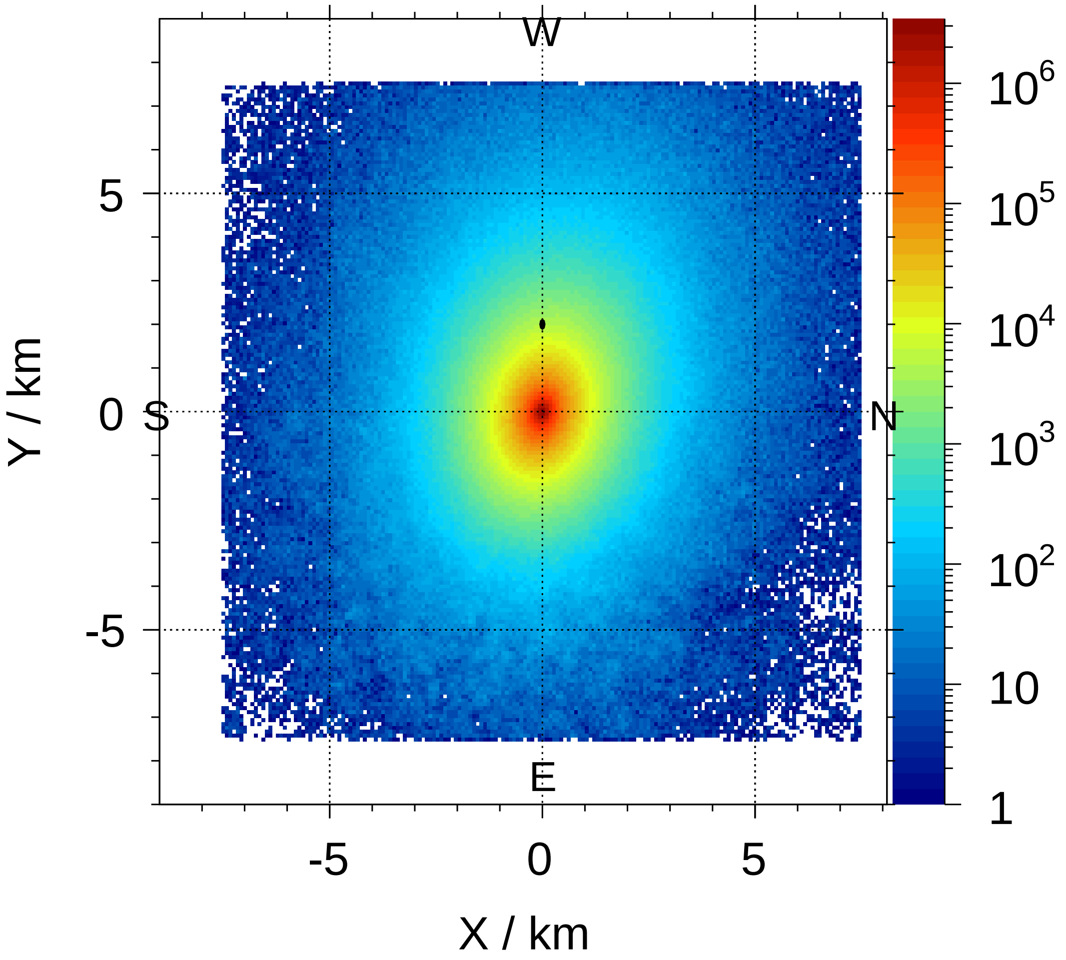

Figure 4.8: Number of Cherenkov photons on the ground for simulated CORSIKA shower. Shower core is at the origin of coordinates. The Cherenkov light is brightest directly at the shower core, but a 2 km distant detector on the ground, marked as a black ellipse is also abundantly illuminated.

CORSIKA provides information about position of the hit on the ground, angular direction, production height, hit time as well as weight for each Cherenkov photon. With these it is possible to calculate the photon track in the atmosphere and consider all emission points as in figure 4.9. The attenuation of the photons in the atmosphere is currently not implemented, but could be deactivated in Offline also for cross-checks.

The CORSIKA Cherenkov simulation takes more aspects of the Cherenkov light generation into account than the light simulation in Offline. Although the shower axis is pointing to the origin of coordinates, some particles are travelling in the direction of the telescope continuously producing photons (visible as low intensity tracks). These can cause light and time profile fluctuations not observed in fluorescence dominated showers. Another attribute shown in the simulation is the asymmetry in the light production with respect to the shower axis, as more electrons are arriving at the aperture on the side of the shower in front of the detector than on the opposite side.

For detailed investigation of the influence on the reconstruction and comparisons of Cherenkov

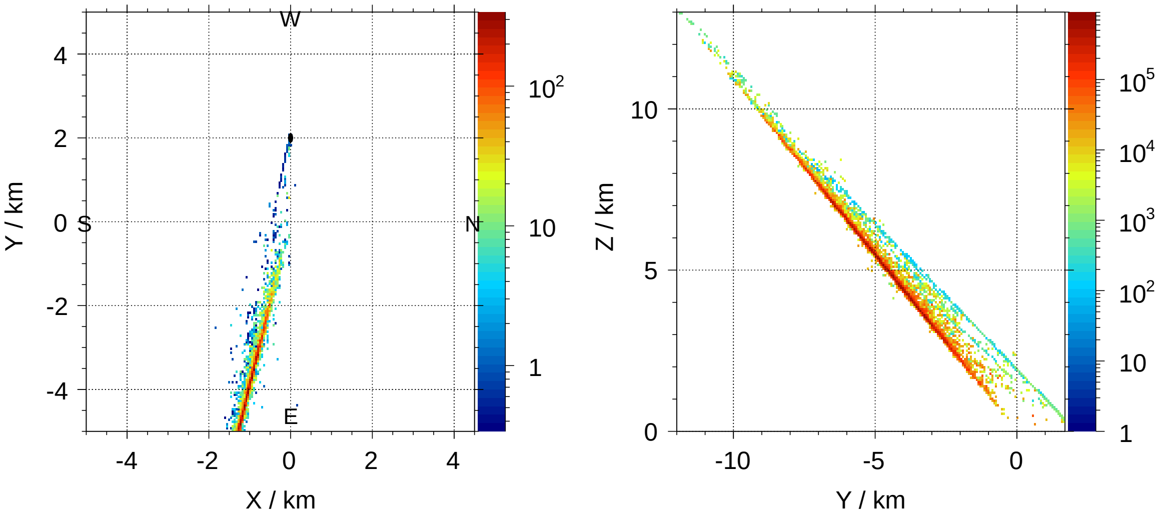

Figure 4.9: Number of emitted photons in *Left*: side and *Right*: top projection, which hit an artificial detector flat on the ground placed 2 km away from the shower core. CORSIKA coordinates are used (cf. 4.1)

light reconstructed from data and Monte-Carlo showers, a realistic aperture description was implemented, using the real detector description in simulated or recorded data files. CORSIKA photons arriving at the apertures within the fields of view of the telescopes are selected. The apertures are made scalable in radius, which can circumvent the thinning effect of too many photons missing the aperture. With this approach simulated Cherenkov photons can be eventually used in the reconstruction chain (for example as an input for *TelescopeSimulatorKG*) independently of Offline Cherenkov simulation for better reconstruction of Cherenkov abundant showers.

Figure 4.10 shows a preliminary time-angle profile gained from CORSIKA Cherenkov photons alongside with Offline.

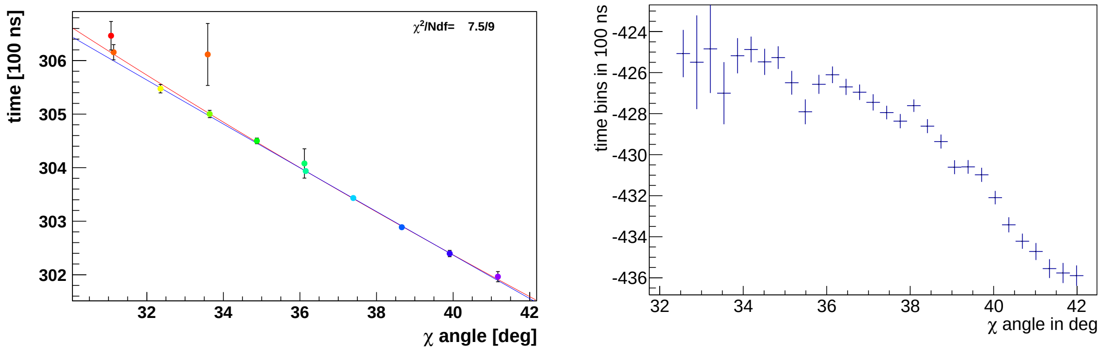

Figure 4.10: Time-Angle profiles as described in subsection 4.4.2 from the single shower, referenced at the beginning of the section, simulated at 1.7 km distance with the *Left*: Offline reconstruction fluorescence and Cherenkov light and *Right*: CORSIKA Cherenkov photons hitting a detector aperture with coordinates and pointing of the HEAT bay 2. A different development in both time-angle profiles indicates differences in light simulation in Offline and CORSIKA and should be further investigated.

The presented intermediate results and framework should be further investigated and expanded. As the usage of Offline is restricted to geometrical tools and detector geometry description the approach allows an independent cross-check of the Cherenkov light handling. However an effort of incorporation in Offline is favorable to perform a piecewise cross-check and to reuse parts of the framework e.g. the description of the atmosphere. The main limitation is the computational power and time needed for production for the detailed Cherenkov information.

5 Cherenkov light in simulated showers

In this chapter the framework consistency for the reconstruction described in the previous chapter is checked for the showers with high direct Cherenkov fraction (cf. (4.12) on page 25). For the high level analyses in the standard FD the Cherenkov cut was introduced in [70], such that events with Cherenkov light fraction greater than 50% are rejected. This was due to prevent low energy events triggered by the sheer Cherenkov light and possible events with high X_{max} uncertainty. In this work in two MC datasets a significant reconstruction bias of X_{max} for the showers with direct Cherenkov fraction greater than 50% is found reconfirming the cut introduced previously.

5.1 Monte-Carlo datasets

The dataset denoted as *CORSIKA* (cf. A.3, page ix) is generated with CORSIKA version 6.980 and reconstructed with Offline version v2r7p7. The *CONEX* dataset is generated by Nils Scharf [47]. Both are used after loose cuts (cf. 6.1, page 33) and are not separated into different primaries, hadronic interaction models or energy bins for this step.

Each dataset is subdivided into the showers with direct Cherenkov fraction below and above 50% as in figure 5.1:

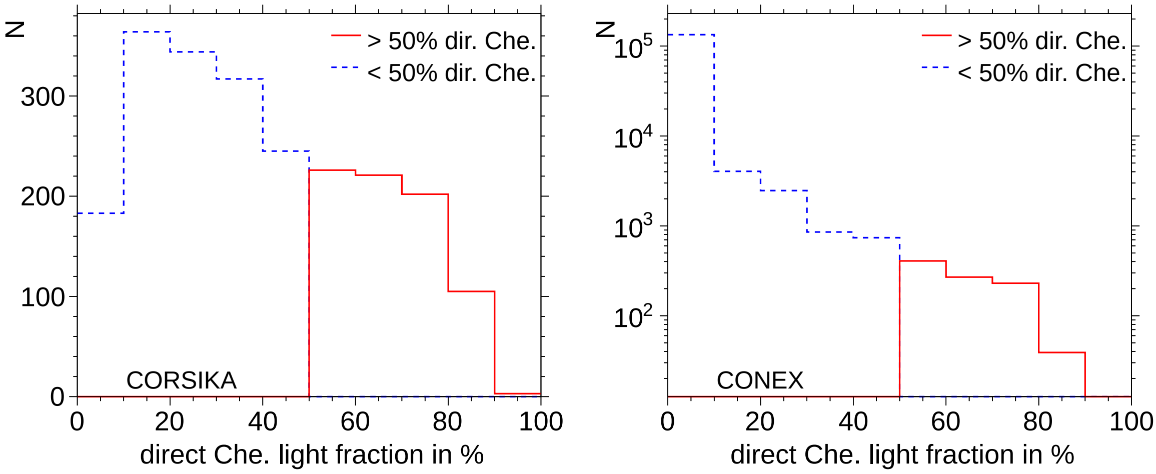

Figure 5.1: Direct Cherenkov light fraction for CORSIKA and CONEX datasets. Cherenkov poor showers are more abundant in CONEX dataset, as the simulated core positions are not close to the eye (cf. A.3).

5.2 Biases for high Cherenkov light fraction

To check the consistency of the framework for simulated and reconstructed HEAT showers, the parameters introduced in section 4.4 are considered in the order of their appearance in the reconstruction chain.

The absolute bias and bias in units of standard deviations are considered for all energies in sum. The bias for observable A is calculated as the difference between simulated ($_{\text{MC}}$) and reconstructed ($_{\text{rec}}$) value, the normalized bias is defined as the ratio of bias and reconstruction uncertainty $A_{\text{uncert.}}$ of the observable: shower detector plane orientation angles φ_{SDP} and ϑ_{SDP}, shower axis parameters R_p, t_0 and χ_0 and finally energy and X_{max}.

$$\mathrm{Bias} = A_{\mathrm{MC}} - A_{\mathrm{rec}} \tag{5.1}$$

$$\mathrm{norm.\ Bias} = \frac{A_{\mathrm{MC}} - A_{\mathrm{rec}}}{A_{\mathrm{uncert.,rec}}} \tag{5.2}$$

The μ shown in figures is the mean bias indicating systematic error of the reconstruction and the σ is the standard deviation of the distributions. Only the statistical uncertainty of the mean is considered.

5.2.1 Shower detector plane

Shower detector plane observables φ_{SDP} in figure 5.2 and ϑ_{SDP} in figure 5.3 described in 4.4 are first to be considered.

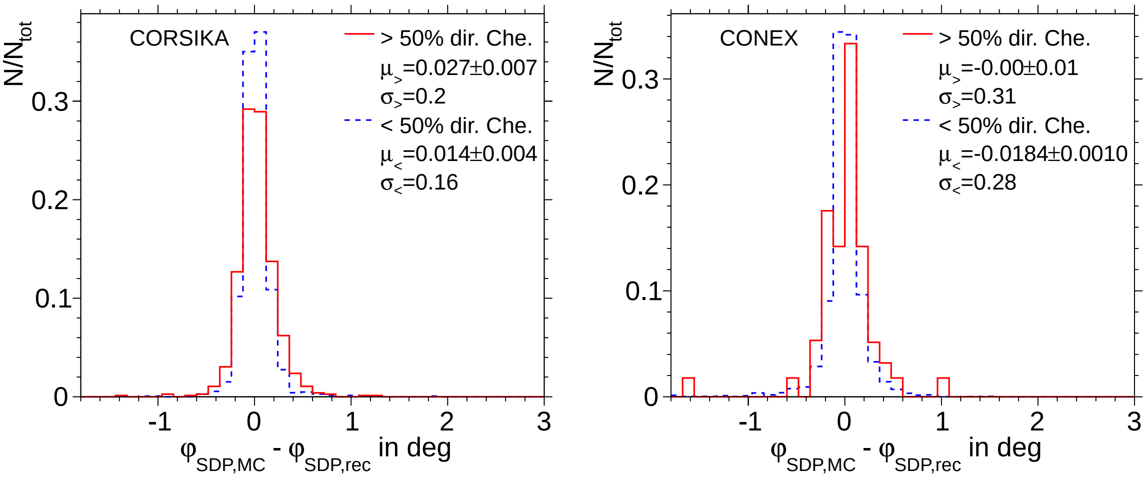

Figure 5.2: Absolute bias on φ_{SDP} for two Cherenkov fraction ranges for CORSIKA and CONEX. High Cherenkov fraction does not bias the reconstruction of the SDP.

Direct Cherenkov light arriving at the detector originates from a narrow section of the light cone in its direction and is expected to be produced in the SDP. As the simulated Cherenkov light is produced at the shower axis, there is no significant reconstruction bias of SDP for Cherenkov-rich showers, as both CORSIKA and CONEX datasets show.

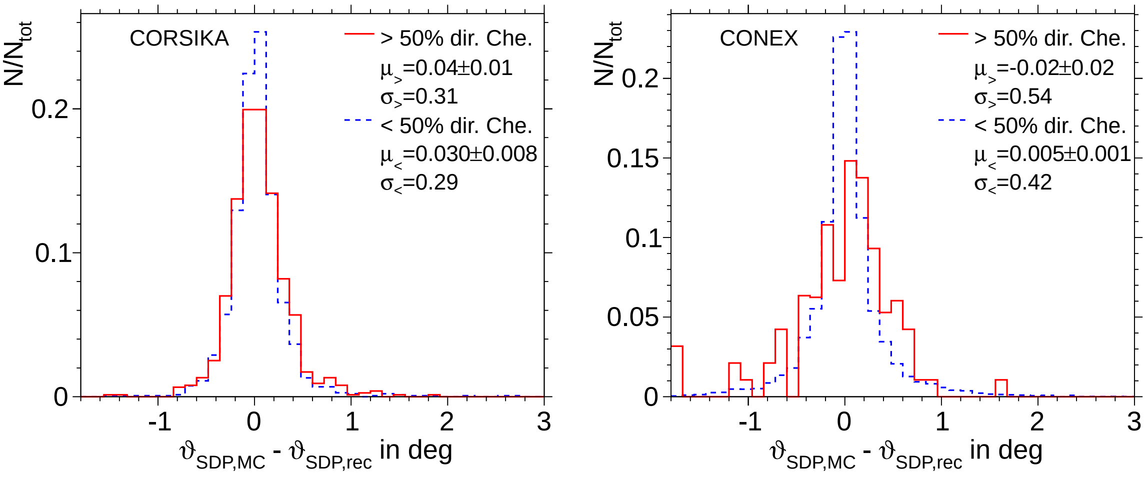

Figure 5.3: Absolute bias on ϑ_{SDP} for two Cherenkov fraction ranges for CORSIKA and CONEX. CONEX and CORSIKA are not compatible with each other the diviation is however small compared to the resolution.

5.2.2 Shower axis

Offline reconstructs the shower axis similarly for Cherenkov-rich and -poor showers, the biases are within the angular resolution of the telescopes (between 1° and 2° [71]) and timing resolution between (50 ns and 200 ns [72]). The smaller spread σ in timing and distance to the axis does not mean a better reconstruction, as the normalized biases (cf. A.2, page vi) are the same for both Cherenkov fraction ranges. The narrower distribution can result from a more constrained phase space for the axis placement. The shower axis is reconstructed with minimum bias for showers with Cherenkov light fraction lower than 50%.

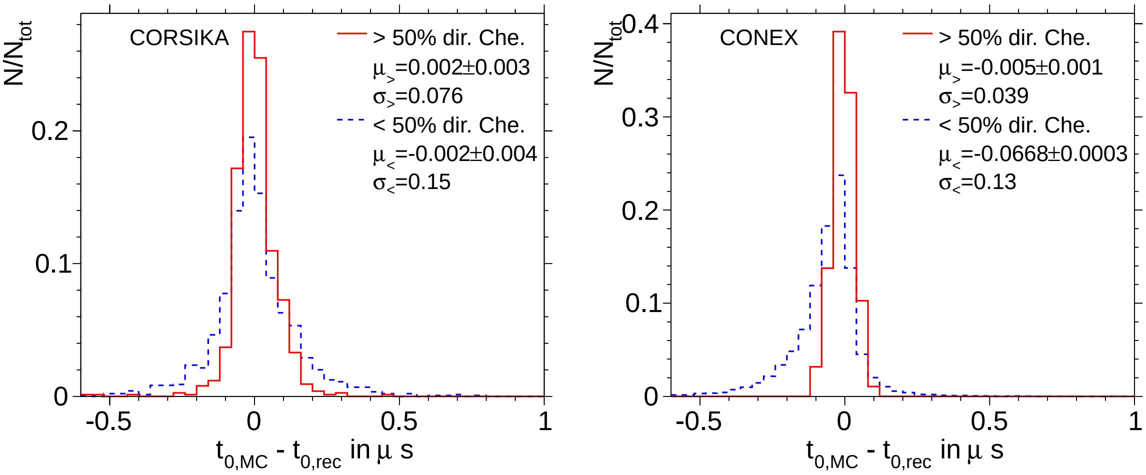

Figure 5.4: Absolute bias on time at the point of closest approach t_0 for two Cherenkov fraction ranges for CORSIKA and CONEX. The resolution for Cherenkov-rich showers is reduced by half.

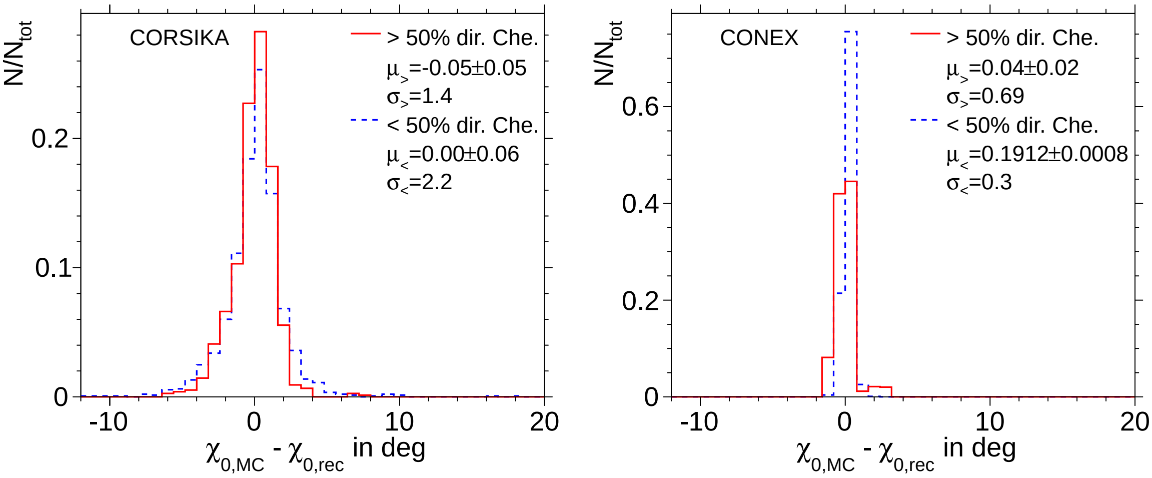

Figure 5.5: Absolute bias on the angle to the ground within SPD χ_0 for two Cherenkov fraction ranges for CORSIKA and CONEX. For the two MC datasets separately the two Cherenkov fractions are compatible. CORSIKA and CONEX are not comparable, as CONEX shows significantly smaller standard deviation, but both biases are within the detector resolution.

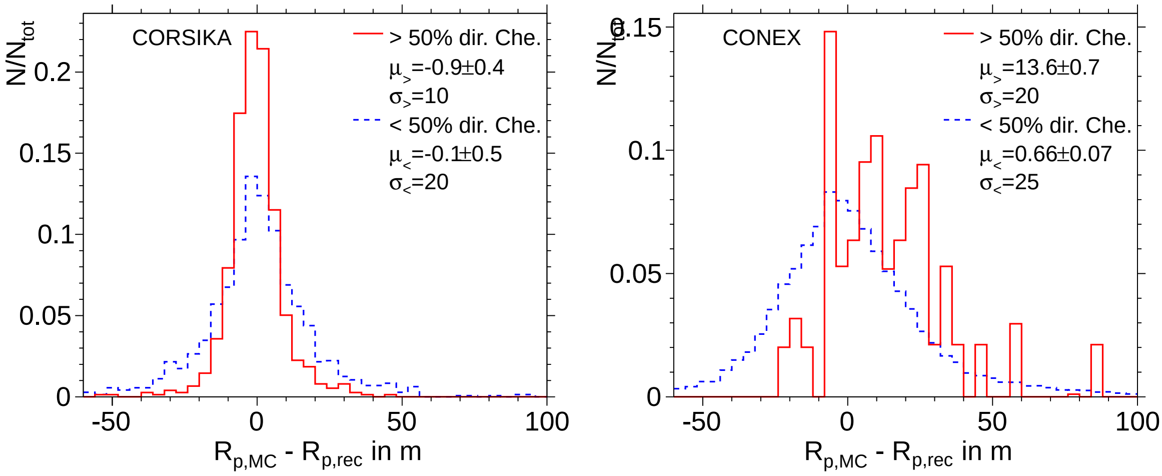

Figure 5.6: Absolute bias on distance of closest approach R_p for two Cherenkov fraction ranges for CORSIKA and CONEX. For CORSIKA the Cherenkov-rich distribution is half as wide as for showers with Cherenkov light fraction less than 50% but both are unbiased. The CONEX showers with high Cherenkov light fraction show a significant bias paired with statistical fluctuations.

5.2.3 Shower parameters

The energy bias for CORSIKA in figure 5.7 is similar for low and high Cherenkov fractions. The somewhat narrower spread can result from limited energy range of showers with high Cherenkov fraction (cf. A.3). The CONEX showers with high Cherenkov light fraction are showing a distinct diviation from an unbiased distribution. The limited shower core distribution range, possibly also only one interaction model and primary, used for CORSIKA simulations and different simulation approaches could result in the discrepancy between CORSIKA and CONEX for Cherenkov rich showers.

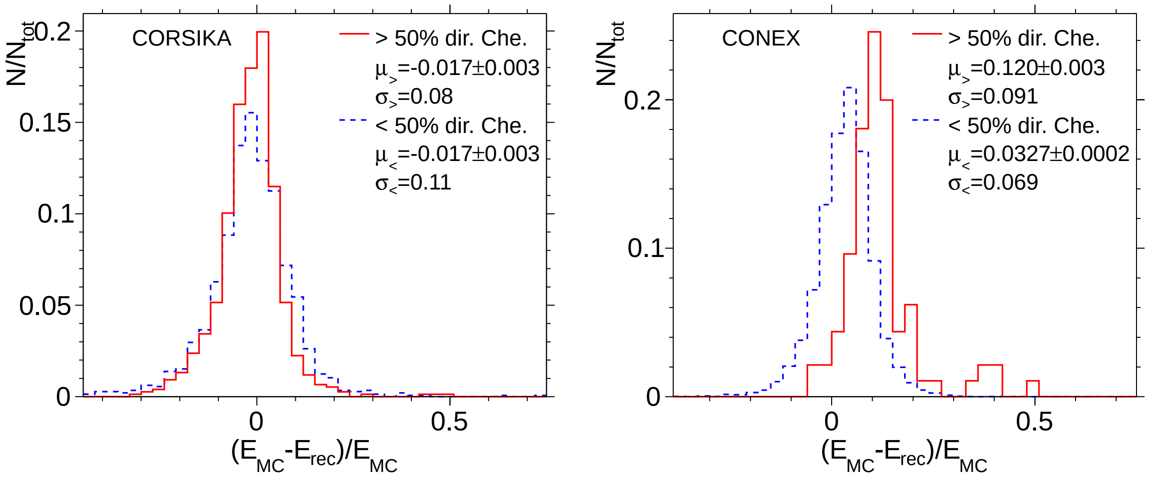

Figure 5.7: Absolute bias on primary energy for two Cherenkov fraction ranges for CORSIKA and CONEX over all energies. The distinct discrepancy can be observed between the reconstructions of Cherenkov-rich shower generated in CORSIKA and CONEX.

The distinct bias of $X_{\max}$ in figure 5.8 is in the order of detector resolution. Two MC datasets are differing from each other, but allow both to conclude, that only showers with low Cherenkov light fraction are consistently reconstructed by the framework and Cherenkov cut introduced above should be used to minimize reconstruction biases.

The bias of $X_{\max}$ for high direct Cherenkov fractions recurs in subsection 6.2.1.

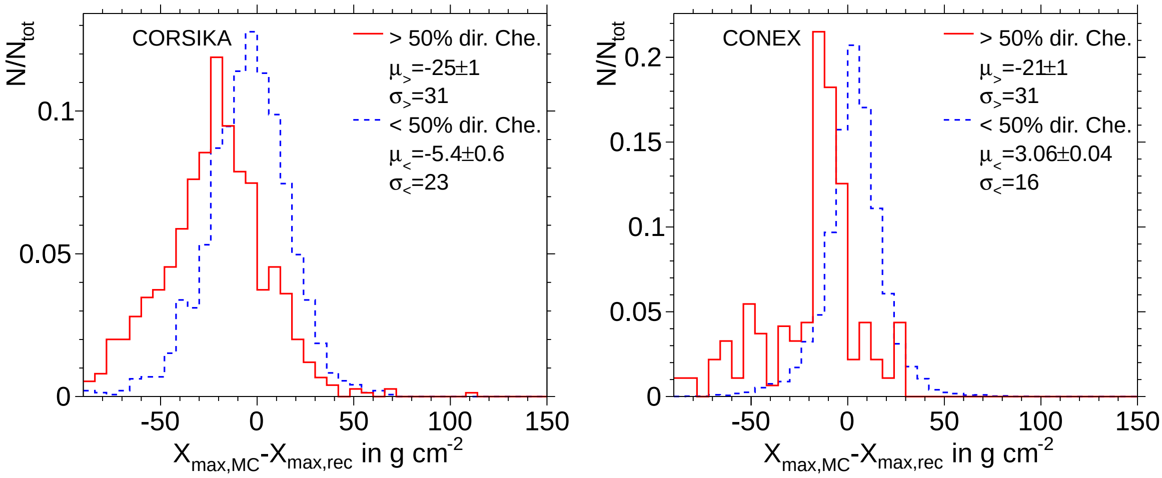

Figure 5.8: Absolute bias on on X_{max} for two Cherenkov fraction ranges for CORSIKA and CONEX over all energies.

6 Cherenkov light in HEAT data

In this chapter the datasets used for the analysis are introduced, the $X_{\max}$ dependence on Cherenkov light is estimated using a loose dataset and the correction of the dependence for the tight dataset is proposed.

6.1 Datasets and cuts

In following sections multiple datasets are used, for which the cuts presented below are applied. For all showers the detection by COHE with HEAT pointed upwards is required. With zenith angle smaller than 60° and energy higher than 10^{15} eV the reconstruction of the shower axis and profile is ensured. The list of the cuts below and their cut efficiencies are summarized in A.4.

6.1.1 Loose

The "loose" dataset contains 17743 showers recorded with COHE between 06.2010 and 10.2011.

- **thetaMax 60.** Cut for maximum zenith angle removes upward going laser shots, horizontal showers and showers after unsuccessful fit without meaningful axis reconstruction.
- **minLgEnergyFD 15.** The absolute energy cut removes all showers without energy reconstruction or unrealistic fit results.
- **energyError 0.95** Maximum relative energy error cut removes showers with meaningful energy entries if an unsuccessful Gaisser-Hillas fit yields a non meaningful 100% uncertainty.
- **xMaxError 250.** $X_{\max}$ uncertainty is set to be lower than $250\,\mathrm{g\,cm^{-2}}$.
- **heatOrientationUp** Only tilted state of HEAT is accepted.
- **eyeCut 100000** The virtual eye COHE (as described in section 4.2) is selected.

6.1.2 Tight

To ensure the compatibility of data with the CONEX dataset the period between 06.2010 and 10.2011 is used, which contains 4603 showers after cuts. The cut set is based on [61] and chosen on top of loose cuts as follows.

- **energyError .2** The relative energy uncertainty is required to be lower 20%.
- **xMaxInFOV 0.0** The $X_{\max}$ is required to be strictly in the field of view of a camera.
- **xMaxError 40.0** The $X_{\max}$ uncertainty is required to be lower than $40\,\mathrm{g\,cm^{-2}}$ matching the detector resolution.
- **deltaProfileChi2 4, profileChi2Ratio 0.9** The difference and ratio cuts for χ^2 of Gaisser-Hillas and straight line fits are discarding flat or multiply bumped energy deposit profiles.
- **maxDepthHole 30.** If the shower profile is sampled partially, e.g. at mirror crossing, or being obscured by clouds, the gap in units of slant depth is required to be smaller than $30\,\mathrm{g\,cm^{-2}}$.
- **maxCoreTankDist 1500.** The reconstructed core position is required to be near an SD station.

6.1.3 Tight and fiducial volume cut

The fiducial volume cut, denoted as FOV-cut, is also used on top of the tight data set. Depending on geometry, energy and atmospheric parameters, showers do not always fall into the observed field of view such that the shower maximum is reconstructed reliably. To minimize the bias the fiducial volume cut is introduced in [73] and optimized for COHE in [61]. After this cut there are 2307 events left.

6.2 Mean X_{max}

In the high level analysis the mean X_{max} and spread are tied to the primary composition (cf. [24]). The Cherenkov fraction cut used there is effective against the reconstruction bias shown before. In this section the distribution of X_{max} mean measured with HEAT is shown to have a small dependence on the Cherenkov fraction and is also affecting the showers with Cherenkov fraction below 50% used for other studies. The Cherenkov light fraction for a given energy is mainly dependent on the shower geometry from the point of view of the detector and is not expected to have this small dependence. A first order correction is proposed.

6.2.1 Monte-Carlo cross-check

To check the assumption of mean X_{max} not depending on Cherenkov light fraction, CONEX dataset after tight cuts is considered in 6.1.Although with high fluctuations for lower energy bins (6.1), Monte-Carlo shows a flat distribution of mean X_{max} over the relevant Cherenkov fraction range, confirming the assumption above. The mean X_{max} depends on the primary composition, as can be seen in the difference between the proton and the iron distribution below. As the composition of the cosmic rays is currently studied, no safe assumption can be made about the offset and any direct correction, as presented below, has to change the slope of the distribution only.

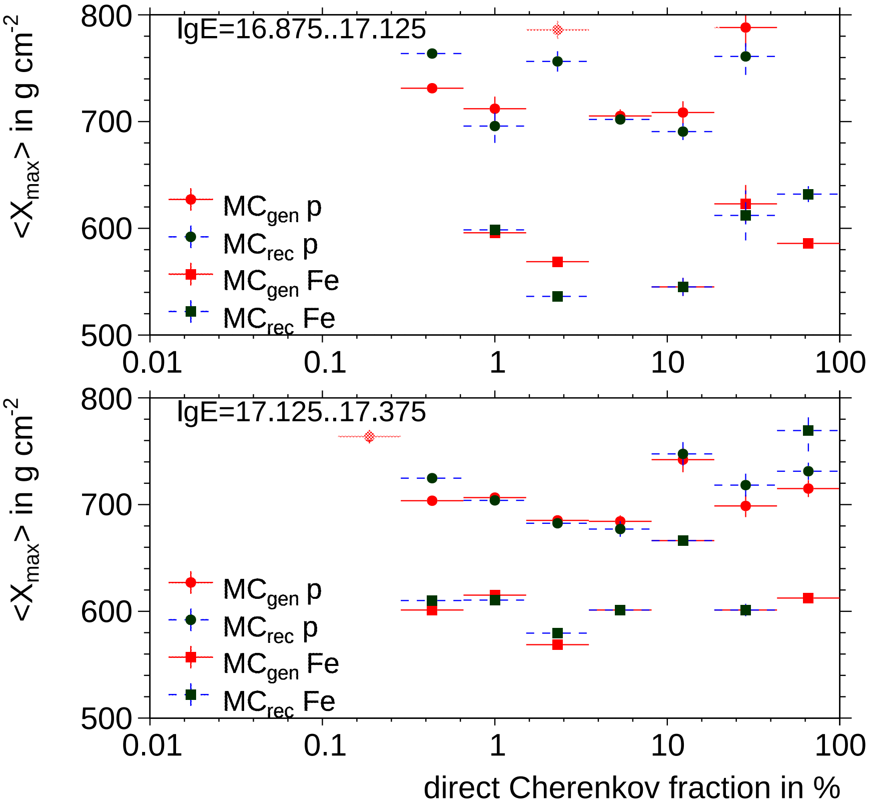

Figure 6.1: Dependence of mean X_{max} on the direct Cherenkov light fraction for CONEX showers. ($E = 1 \cdot 10^{17}\,\mathrm{eV}, E = 1 \cdot 10^{17.25}\,\mathrm{eV}$)

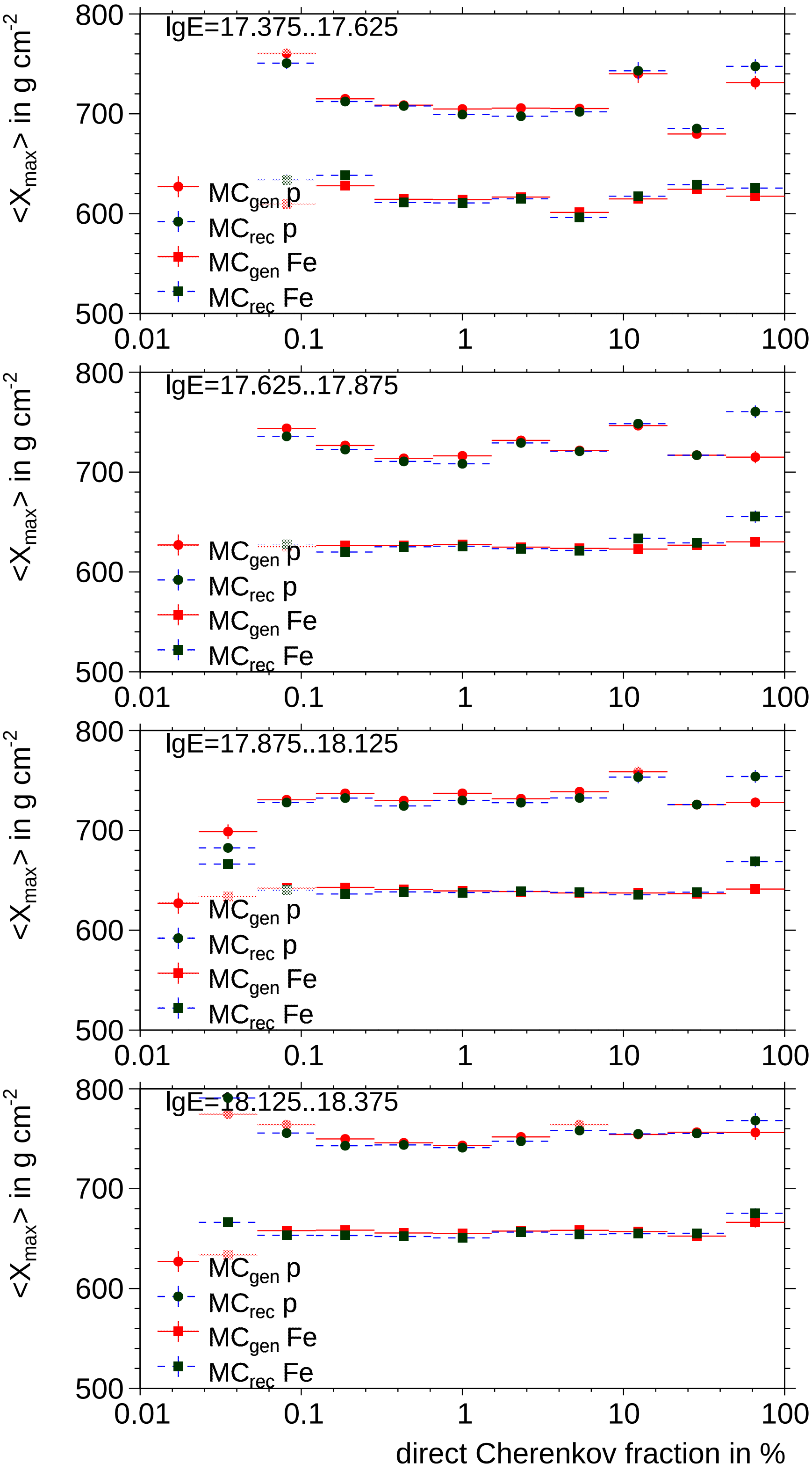

Figure 6.1: (cont.) Dependence of mean $X_{\max}$ on the direct Cherenkov light fraction for CONEX showers. ($E = 1 \cdot 10^{17.5}$ eV, $E = 1 \cdot 10^{17.75}$ eV, $E = 1 \cdot 10^{18.0}$ eV, $E = 1 \cdot 10^{18.25}$ eV)

6.2.2 HEAT data

In the plots 6.2 the linear mean, as most simple first order assumption, of X_{max} was determined for every bin of direct Cherenkov fraction for the dataset after loose cuts. Statistical uncertainties are given for the error of the mean X_{max}. A linear fits determining the slopes, statistical uncertainties and reduced χ^2 values are performed in ROOT [74]. The slope of the linear fit is denoted as m below and its statistical uncertainty as σ_m.

The three datasets are showing similar behaviour. Apart from lowes energy bin, the data shows a The shape is similar for loose and tight datasets indicating a reconstruction issue common for all showers justifying the correction based on the loose dataset. The offsets differ for all three datasets. The FOV-cut does not eliminate the dependence on its own and will not be considered further.

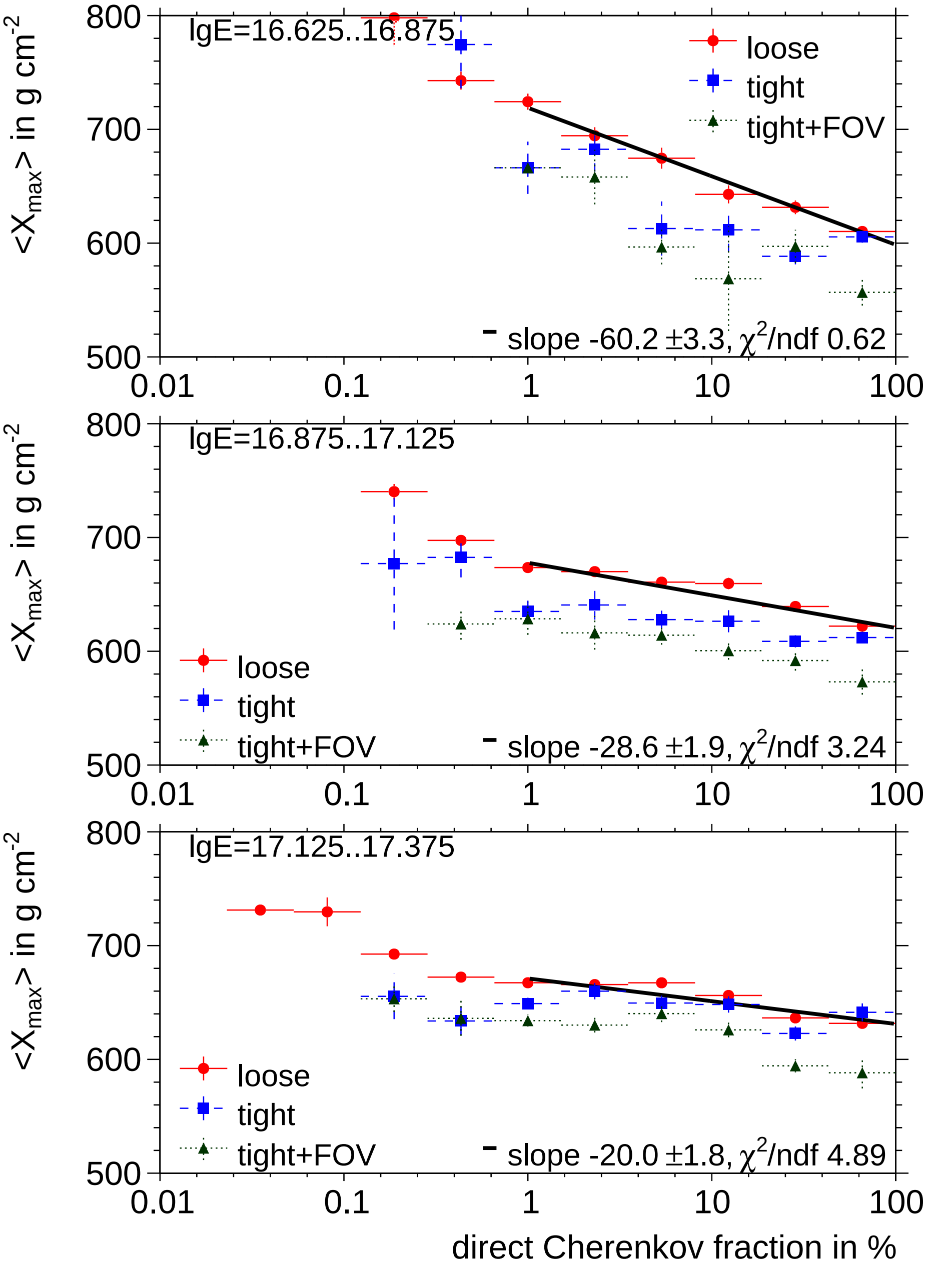

Figure 6.2: Dependence of mean X_{max} on direct Cherenkov light fraction for three data sets ($E = 1 \cdot 10^{16.75}$ eV, $E = 1 \cdot 10^{17.0}$ eV, $E = 1 \cdot 10^{17.25}$ eV). The three datasets show similar shapes for all energies, the distributions have different offsets being flat in the region around 0.1% and 3% (for all but two energy bins).

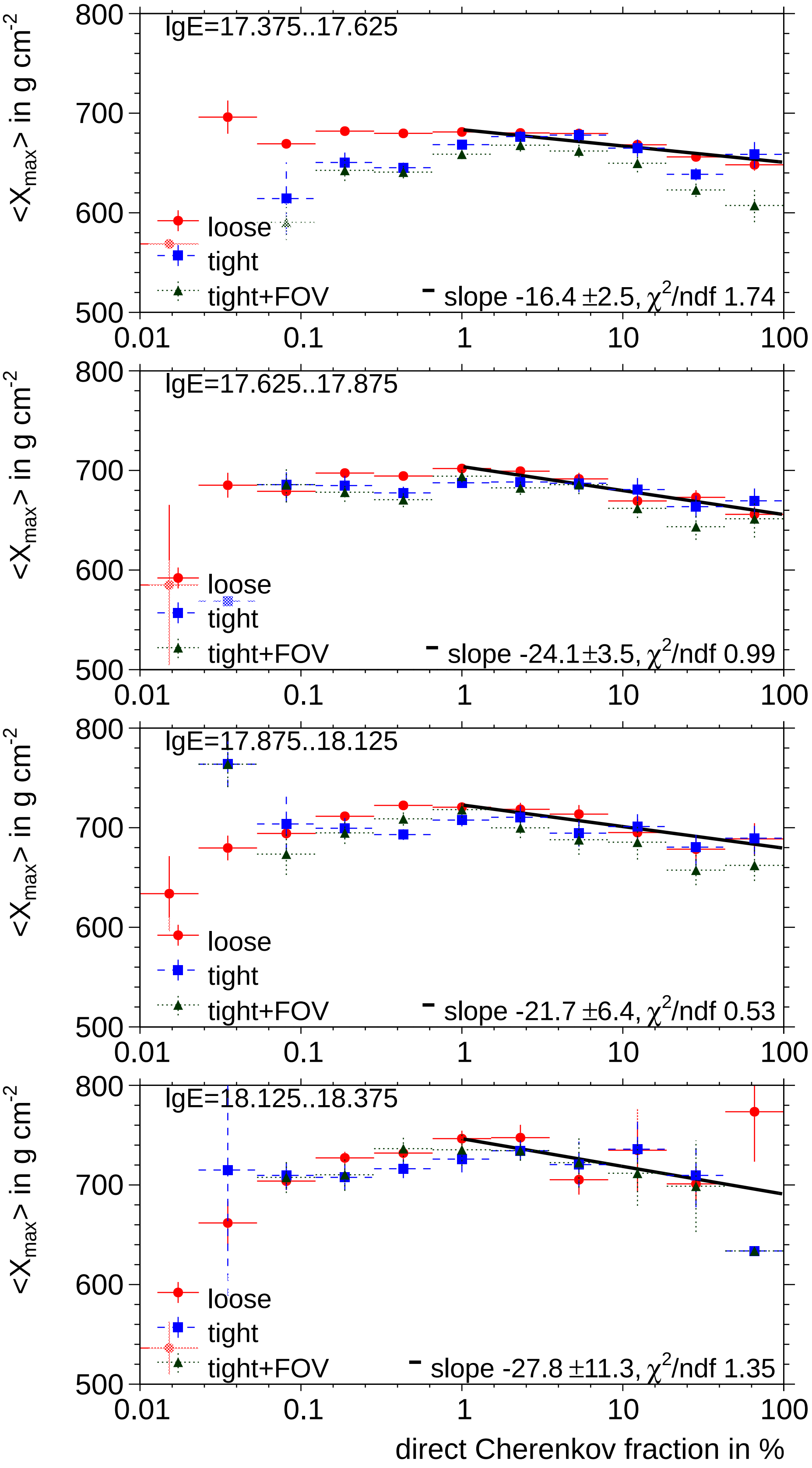

Figure 6.2: (cont.) Dependence of mean $X_{\max}$ on direct Cherenkov light fraction for three data sets ($E = 1 \cdot 10^{17.5}$ eV, $E = 1 \cdot 10^{17.75}$ eV, $E = 1 \cdot 10^{18.0}$ eV, $E = 1 \cdot 10^{18.25}$ eV)

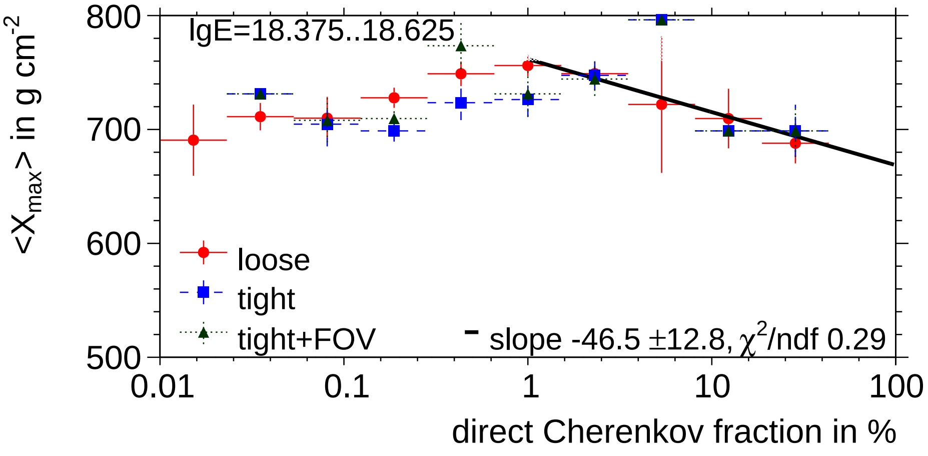

Figure 6.2: (cont.) Dependance of mean $X_{\max}$ on direct Cherenkov light fraction for three data sets ($E = 1 \cdot 10^{18.5}$ eV).

The reason for the dependence is not yet known. In showers with higher Cherenkov light fraction the fluorescence light yield has a lower influence on the shower profile, thus if the absolute or spectral yield measurement of the fluorescence light used in the reconstruction is inaccurate, a dependence in energy and $X_{\max}$ on Cherenkov light fraction is expected. Stereo shower measurements, that is observation of the same shower from different points of view, or with a different type of detector (cf. [75]) shoud be insightful to reduce this systematics.

As shown in an unpublished talk in 2007 Collaboration meeting by Jose Bellido, the dependence is also present in standard FD data and its magnitude is dependent on the relative time offset between SD and FD (cf. 4.4). With detailed Cherenkov simulations as in 4.5 it is possible to determine a systematically different timing behaviour or axis relation of Cherenkov light compared to the current model in the framework.

6.2.2.1 Correction

The correction of $X_{\max}$ for showers with significant Cherenkov light contribution is chosen to be applied for fraction greater than 1%, keeping showers with lower fraction unaffected. The adjusted $\tilde{X}_{\max}$ and its new statistical uncertainty can be expressed using short-hand notation $N_T = N_c + N_{cs} + N_f$ for total number of photons as follows:

$$\tilde{X}_{\max}(N_c, N_{cs}, N_f) = X_{\max} - m \lg\left(\frac{N_c}{N_T} \cdot 100\right) , \quad \text{for} \quad \tfrac{\mathrm{N_c}}{\mathrm{N_T}} > 0.01 \tag{6.1}$$

$$\sigma_{\tilde{X}\max} = \sqrt{\sigma^2_{X\max} + \left(\sigma_m \lg\left(\frac{N_c}{N_T} \cdot 100\right)\right)^2 + \left(\frac{m}{\ln 10}\right)^2 \left(\frac{1}{N_c} - \frac{1}{N_T}\right)} , \tag{6.2}$$

with N_c number of direct Cherenkov photons, N_{cs} number of scattered Cherenkov photons and N_f number of fluorescence photons at the aperture. m is the correction parameter from the fit and σ_i the corresponding uncertainties, which are summarized in 6.3. $\tilde{X}_{\max} = X_{\max}$ is valid for Cherenkov light fractions below 1%. For energy bins $E = 1 \cdot 10^{18.25}$ eV and $E = 1 \cdot 10^{18.5}$ eV the number of events above 10% is not sufficient, therefore the correction should be applied to the energy region $E = 10^{16.75}$ to $10^{18.0}$ eV.

The correction is applied to the dataset after tight cuts as presented in figures 6.4. The last bin of Cherenkov light fraction is not considered due to the bias described in 5.2 - the vertical green line indicates the 50% Cherenkov fraction cut. The dependence is now mostly in the range of statistical uncertainty of the newly fitted slope. The bias of high Cherenkov fraction showers has become the dominant effect but is not considered in this work.

To conclude, a dependence of the mean $X_{\max}$ on Cherenkov light fraction was found and quantified for the HEAT data. The origin is not yet known, although the Monte-Carlo simulations do not show this dependence, nor is it significant for energies higher than 10^{18} eV. For the lower energies and high Cherenkov light fractions a correction was suggested and applied to the tight dataset. The resulting mean X_{max} distribution is compatible to a constant within two standard deviations and is dominated by higher order fluctuations.

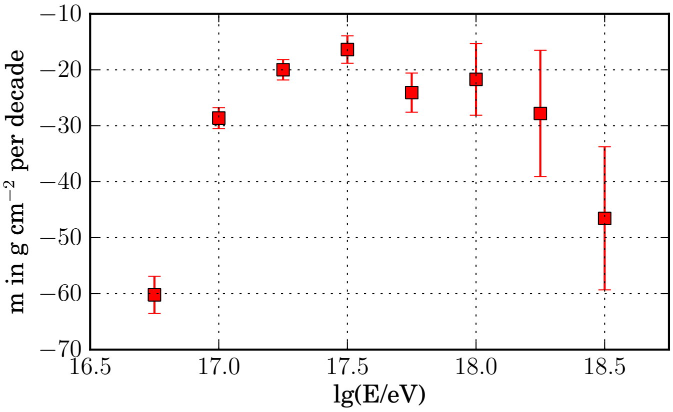

Energy bin	m	$\pm\sigma_m$
	g cm^{-2}	
16.75	-60.2	3.3
17.0	-28.6	1.9
17.25	-19.9	1.8
17.5	-16.3	2.5
17.75	-24.1	3.5
18.0	-21.7	6.4
18.25	-27.8	11.3
18.5	-46.5	12.8

Figure 6.3: Correction factors m for mean X_{max} at considered energy bins. Statistical uncertainties are extracted from the fit

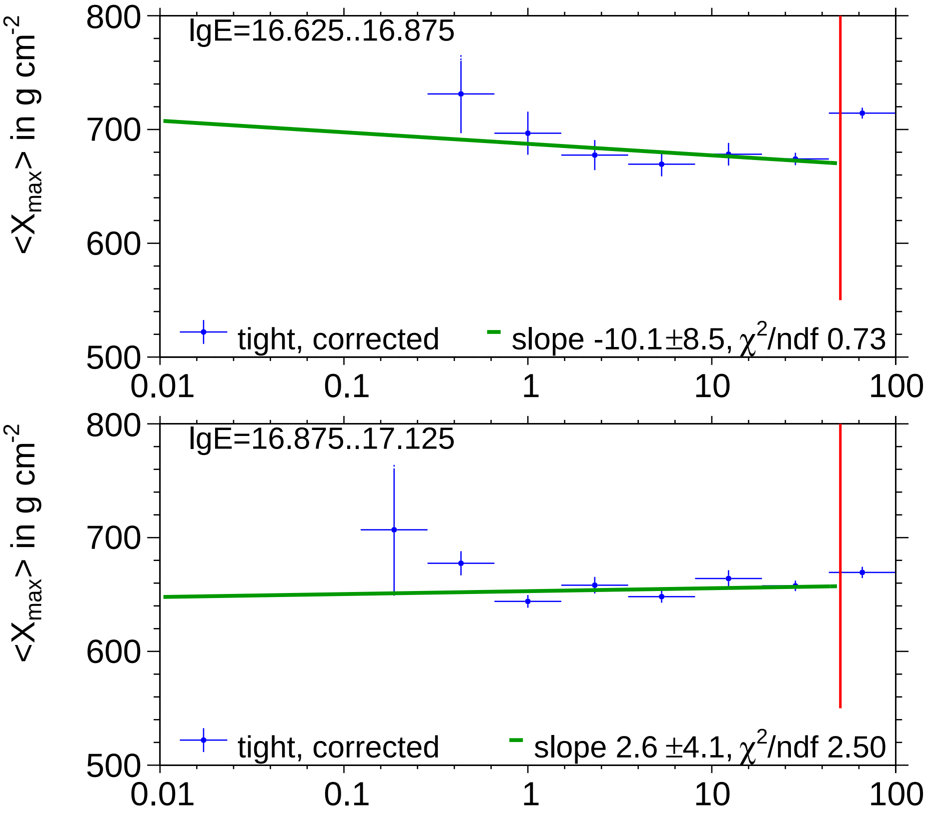

Figure 6.4: Mean X_{max} at different direct Cherenkov light fractions for the tight dataset with applied correction and 50% Cherenkov cut (dark-red line), the distribution is flat within two standard deviations. ($E = 1 \cdot 10^{16.75}\,\mathrm{eV}, E = 1 \cdot 10^{17.0}\,\mathrm{eV}$)

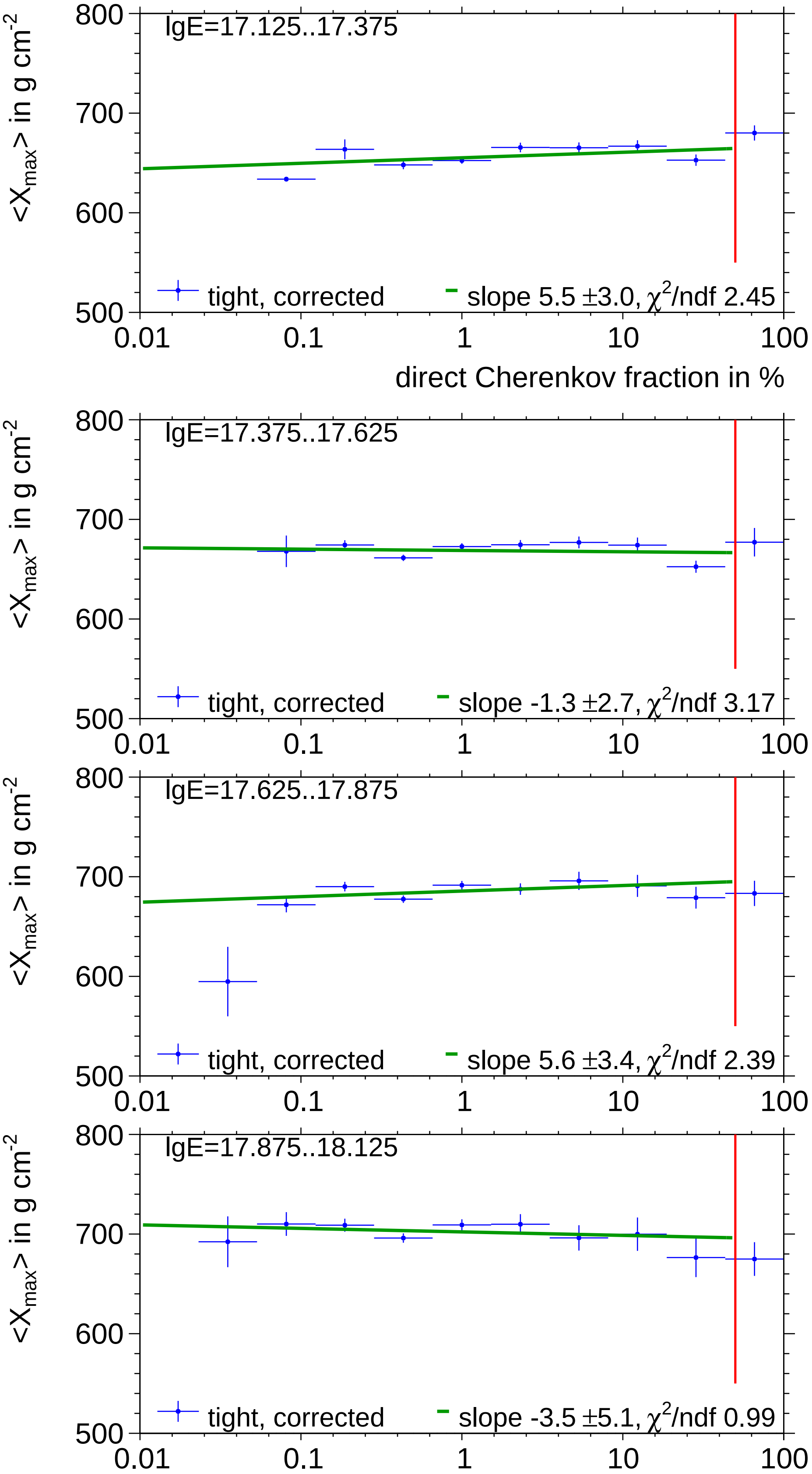

Figure 6.4: (cont.) Mean X_{max} at different direct Cherenkov light fractions for the tight dataset with applied correction. ($E = 1 \cdot 10^{17.25}$ eV, $E = 1 \cdot 10^{17.5}$ eV, $E = 1 \cdot 10^{17.75}$ eV, $E = 1 \cdot 10^{18.0}$ eV)

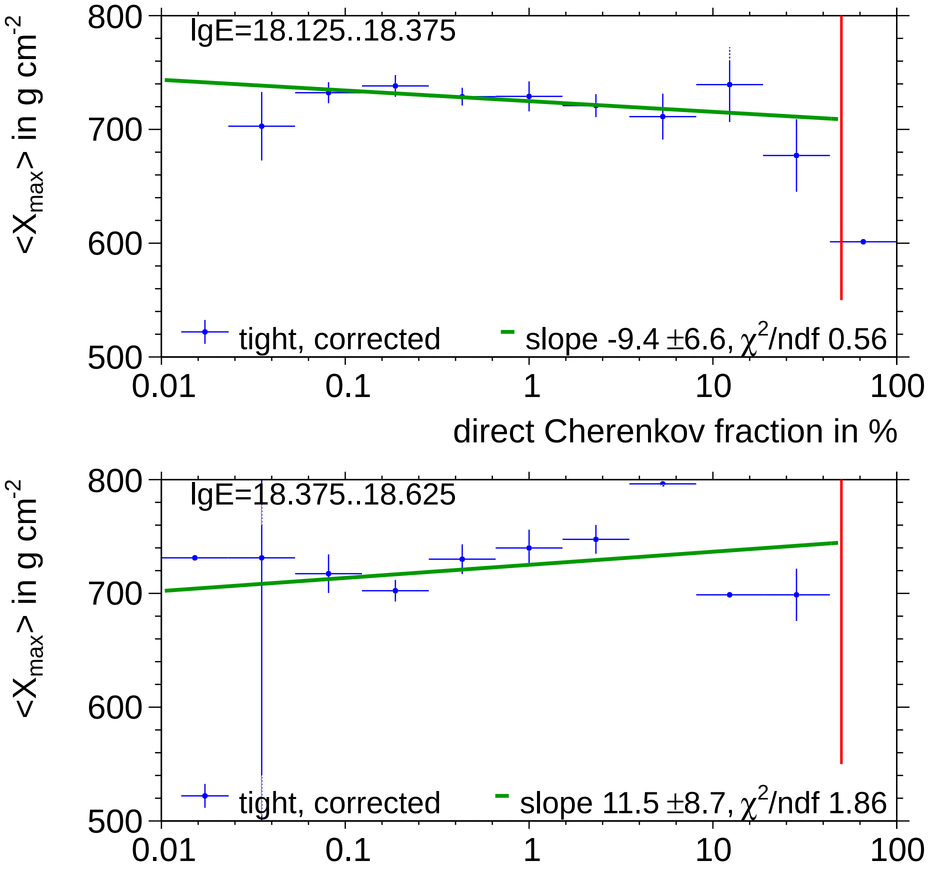

Figure 6.4: (cont.) Mean $X_{\max}$ at different direct Cherenkov light fractions for the tight dataset with applied correction ($E = 1 \cdot 10^{18.25}$ eV, $E = 1 \cdot 10^{18.5}$ eV).

7 Summary and outlook

HEAT is the newest extension of the fluorescence detector at the Pierre Auger Observatory. The higher elevation of the field of view compared to the other four sites allows a measurement of lower energy showers. The number of showers pointing towards the telescopes is increasing and with it the showers with high Cherenkov light fraction.

For this work various shower datasets are used. The HEAT data is split into two datasets with loose cuts only and tight cuts. The CONEX datasets for proton and iron after tight cuts are used for MC comparison. The CORSIKA dataset is generated in the course of building a Cherenkov light library for further studies.

A framework for the extraction of detailed Cherenkov light information from CORSIKA simulations using a realistic detector geometry description is developed. With it the Cherenkov light simulation in Offline can be cross-checked or complemented. The CORSIKA Cherenkov simulation takes more aspects of the Cherenkov light into account and is independent of the Cherenkov light description in Offline. Thus it can be used for further studies of the showers with high Cherenkov fraction.

The Offline framework simulates the detector response for the Monte-Carlo showers and is the main tool for reconstruction of air showers recorded by the telescopes. In this work the reconstruction of Cherenkov dominated showers is compared to the showers with Cherenkov light fraction of less than 50%. A study is performed with CORSIKA showers reconstructed in Offline looking for reconstruction biases. It was shown, that the biases of angular reconstruction, including the shower-detector-plane and shower axis parameters, for both Cherenkov rich and poor showers are small and lie below the resolution of the detector. The energy reconstruction bias is also small for both high and low Cherenkov fraction showers.

The quantity $X_{\max}$ shows a significant bias for the simulated showers with Cherenkov light fraction above 50%, which indicates an inconsistency of the framework. As the generated CORSIKA sample is limited to one interaction model and one primary, and the CONEX dataset is statistically limited in the region of high Cherenkov fraction showers, the bias should be further investigated in a dedicated Monte-Carlo study. With a study using the data or simulation of e.g. stereo showers recorded by two eyes at different locations the bias could be understood best, the major caveats being low statistics for this shower class and the absence of other high elevation telescopes with an overlapping field of view.

The mean $X_{\max}$ distribution in HEAT data shows a small dependence on direct Cherenkov fraction per energy bin for fractions above several percents, which is not expected, as the Cherenkov fraction is mainly dependent on the position of the shower relative to the telescopes. The HEAT data is divided into three datasets with loose, tight and FOV cuts on top of each other reproducing the $X_{\max}$ dependence in all of them. The dependence is found in all considered energy bins, becoming steeper for higher energies. The cross-check with the CONEX dataset shows no such dependence for proton and iron showers.

The Dataset after loose cuts is used as the basis of the dependence estimation with a linear fit on mean $X_{\max}$ as a function of direct Cherenkov fraction. The dependence is then used as a first order correction for the HEAT dataset after tight cuts. The resulting mean $X_{\max}$ after correction is shown and is dominated by the bias for high Cherenkov fractions and statistical fluctuations.

A Appendix

A.1 Bias of CORSIKA dataset

A.1.1 Normalized Bias

Normalized biases of CORSIKA dataset.

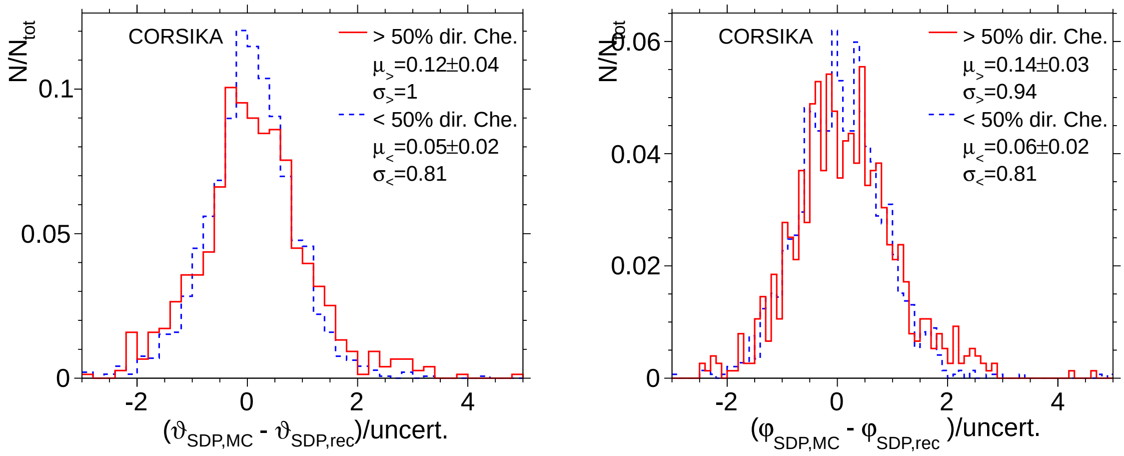

Figure A.1: Normalized bias on SDP angles φ_{SDP} and ϑ_{SDP} for two Cherenkov fraction ranges

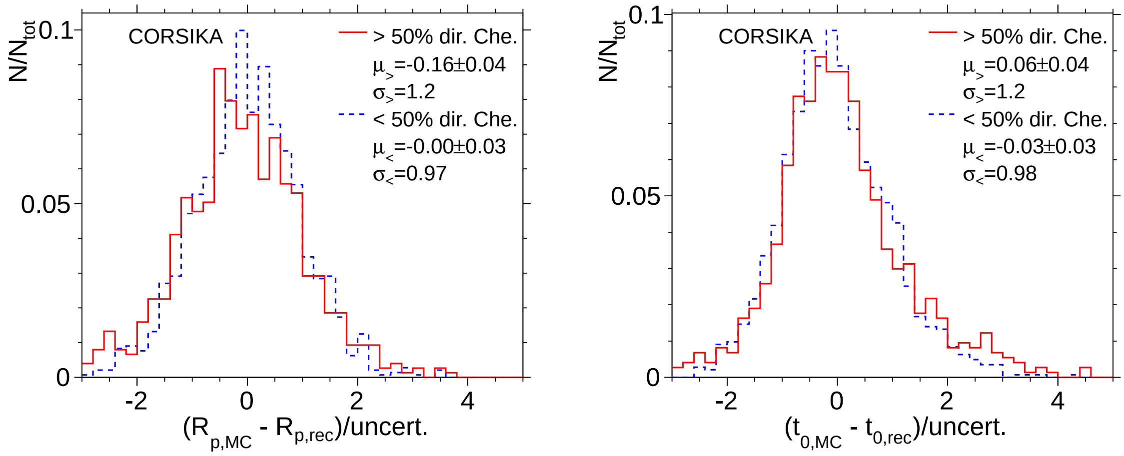

Figure A.2: Normalized bias on distance of closest approach R_p and time at the point of closest approach t_0 for two Cherenkov fraction ranges

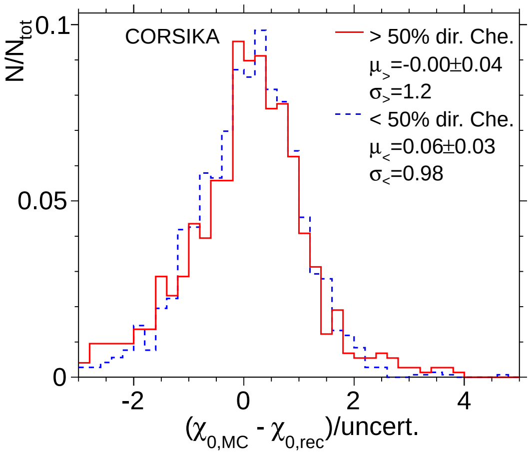

Figure A.3: Normalized bias on angle to the ground within SPD χ_0 for two Cherenkov fraction ranges

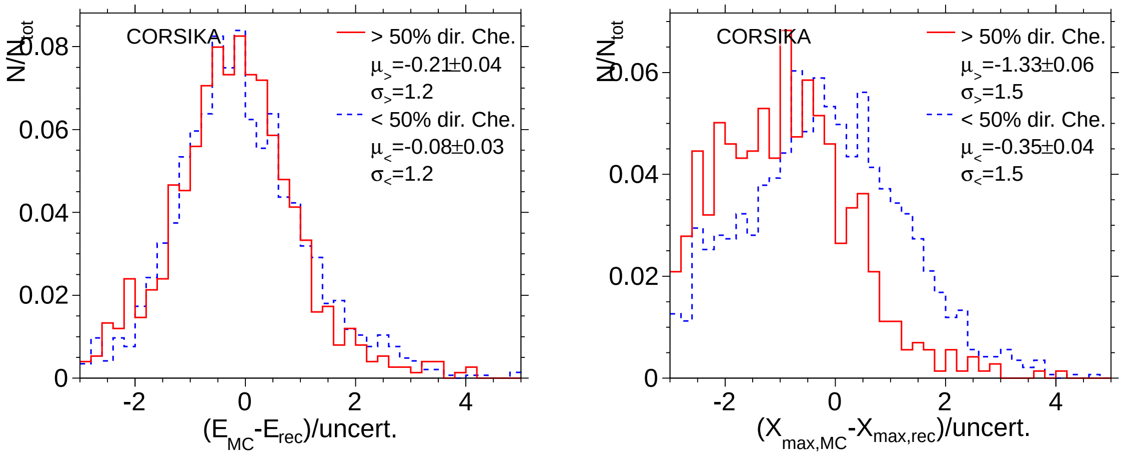

Figure A.4: Normalized bias on primary energy E_0 and shower maximum $X_{\max}$ for two Cherenkov fraction ranges

A.2 Module sequence

Module sequence used for reconstruction of CORSIKA showers.

```
<loop numTimes="unbounded" pushEventToStack="yes">
  <!-- Simulation -->
  <module> EventFileReaderOG </module>
  <module> MCShowerCheckerOG </module>
  <loop numTimes="1" pushEventToStack="yes">
    <module> EventGeneratorOG </module>
    <try>
      <module> SdSimpleSimKG </module>
    </try>
    <try>
      <module> FdSimEventCheckerOG </module>
      <module> ShowerLightSimulatorKG </module>
      <module> LightAtDiaphragmSimulatorKG </module>
      <module> ShowerPhotonGeneratorOG </module>
      <module> TelescopeSimulatorKG </module>
      <module> FdBackgroundSimulatorOG </module>
      <module> FdElectronicsSimulatorOG </module>
      <module> FdTriggerSimulatorOG </module>
    </try>
    <try>
      <module> CentralTriggerSimulatorXb </module>
      <module> CentralTriggerEventBuilderOG </module>
      <module> EventBuilderOG </module>
    </try>
  </loop>
  <!-- Reconstruction -->
  <loop numTimes="1" pushEventToStack="yes">
    <module> EventCheckerOG </module>
    <try>
      <module> FdCalibratorOG </module>
      <module> FdEyeMergerKG </module>
      <module> FdPulseFinderOG </module>
      <module> PixelSelectorOG </module>
      <module> FdSDPFinderOG </module>
      <module> FdAxisFinderOG </module>
      <module> HybridGeometryFinderOG </module>
      <module> HybridGeometryFinderWG </module>
      <module> FdApertureLightOG </module> <!-- deprecated -->
      <module> FdApertureLightKG </module>
      <module> FdEnergyDepositFinderKG </module>
    </try>
    <module> RecDataWriterNG </module>
  </loop>
</loop>
```

A.3 CORSIKA steering card

The steering card for CORSIKA is customized for every shower. The CORSIKA sample is generated with discrete log energies (setting $Min{=}Max$) $\lg E/\,\mathrm{eV} = 16.5, 16.75, 17.0, 17.25$, zenith angles 2°, 12°, 22°, 32°, 42°, 52° and 62° and azimuth angles with step of 15° between −180°..180°. The core positions are optimized for higher probability of Cherenkov rich showers, being placed in discrete distances on the 1.5 km, 2.2 km, 2.9 km and 3.6 km in front of HEAT bay 2 optical axis, rotated by 0°, 10.5° and −13.5°.

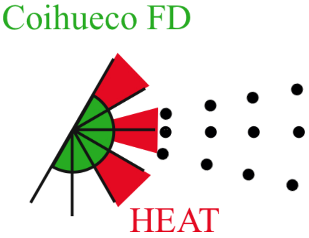

Figure A.5: Core positions for CORSIKA dataset

```
RUNNR   1
EVTNR   1                              number of first shower event
NSHOW   1                              number of showers to generate
USER    bekman                         user
DIRECT  <DIR>                          output directory
SEED    <SEED1> 0 0
SEED    <SEED2> 0 0
SEED    <SEED3> 0 0
THIN    1.000E-06 1.000E+06 500.E2     thining parameters
PRMPAR  14                             particle type of prim. particle
ESLOPE  -2.7                           slope of primary energy spectrum
ERANGE  <Emin>  <Emax>                 primary energy (10^(Emin) .. 10^(Emax)) eV
THETAP  <ThMin>  <ThMax>               zenith angle (deg)
PHIP    <PhiMin>  <PhiMax>             azimuth angle (deg)
OBSLEV  1.452E+05                      observation level (in cm)
FIXCHI  0.001                          starting altitude (g/cm**2)
ATMOD   22                             US Std
MAGNET  19.8 -14.3
HADFLG  0  0  0  0  0  2               flags hadr.interact.&fragmentation
ECUTS   0.1  0.1  0.0005  0.001        energy cuts for particles / GeV
ECTMAP  1E6                            cut on gamma factor for printout
MUADDI  F                              additional info for muons
MUMULT  T                              muon multiple scattering angle
ELMFLG  T   T                          em. interaction flags (NKG,EGS)
STEPFC  1.0                            mult. scattering step length fact.
RADNKG  2.E4                           outer radius for NKG lat.dens.distr.
ARRANG  0                              rotation of array to north
LONGI   T  5.  T  T                    longit.distr. & step size & fit & out
MAXPRT  0                              max. number of printed events
DATBAS  F                              write .dbase file
PAROUT  T  F                           write DAT file, write .tab file
DEBUG   F  6  F  1000000               debug flag and log.unit for out
CERARY  1 1  0.0 0.0   15000E2 15000E2   Che. array
CWAVLG  300.  420.                     Cherenkov wavelength range
CERSIZ  50                             Cherenkov bunchsize
CERFIL  T                              Cherenkov output to extra file
CSCAT   0  0.  0.                      scatter Cherenkov events
CERQEF  F  T  F                        QuantEff, atmosphere, mirrorreflec.
EXIT
```

A.4 Cuts

A.4.1 COHE

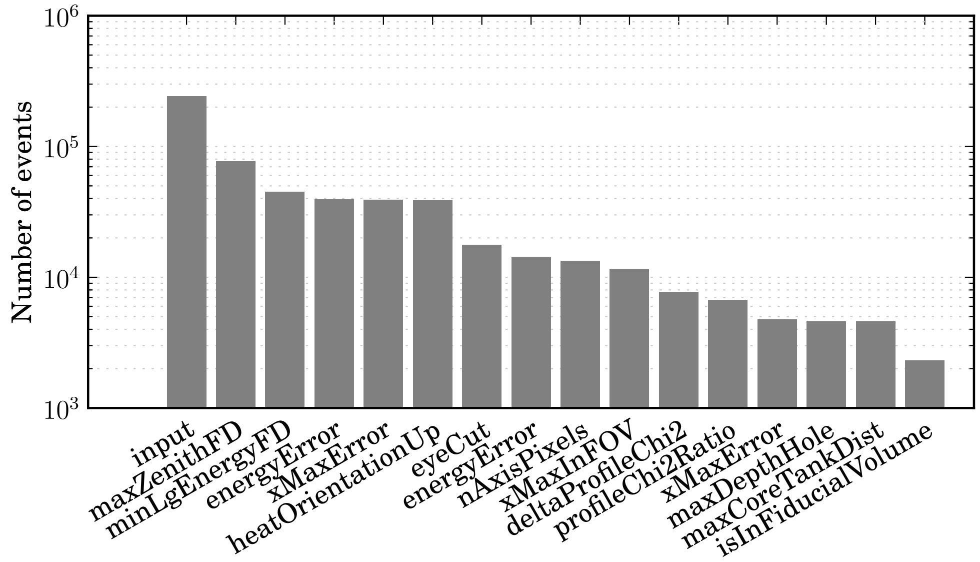

Figure A.6: Events after selection for COHE data: loose, tight and FOV datasets

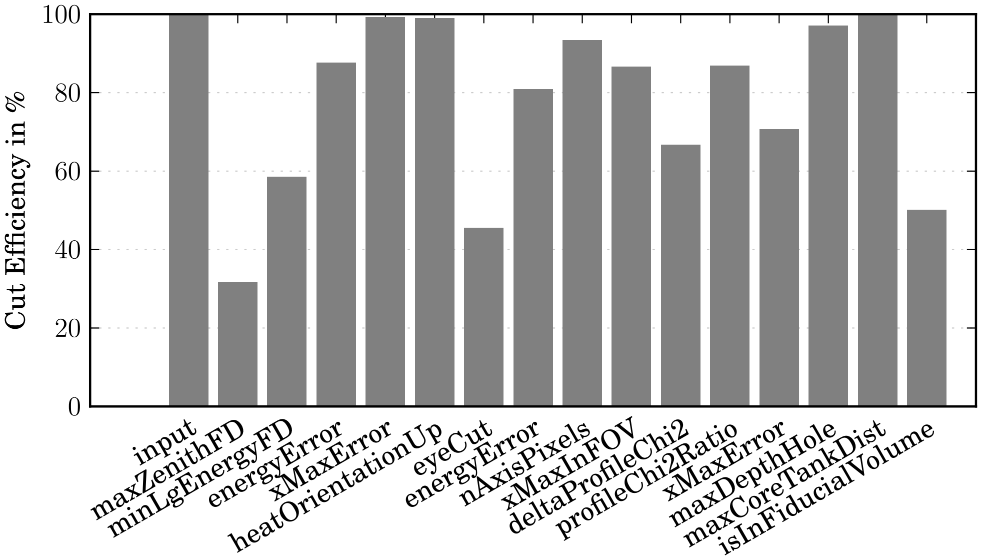

Figure A.7: Selection efficiency for COHE data: loose, tight and FOV datasets

A.4.2 CONEX proton

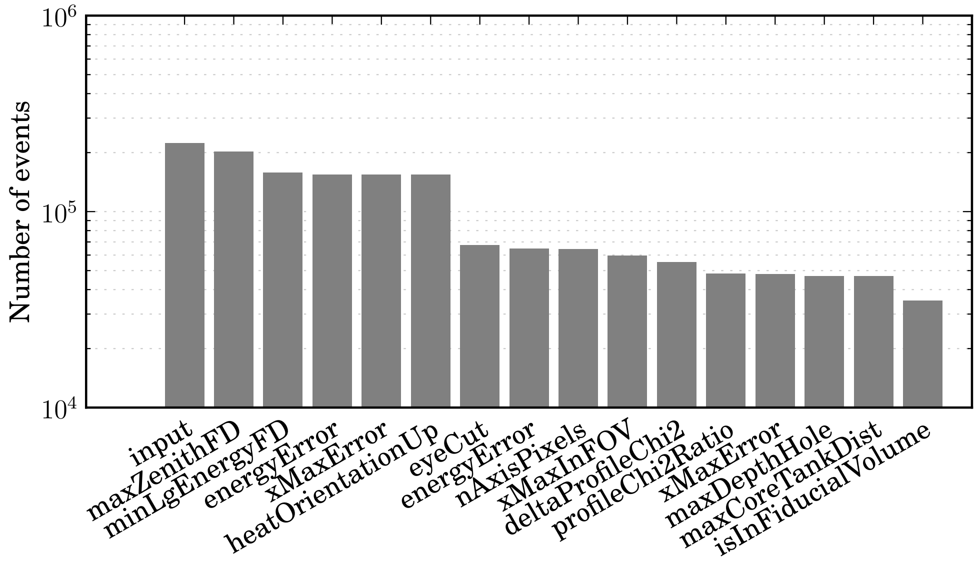

Figure A.8: Events after selection for CONEX p data: loose, tight and FOV datasets

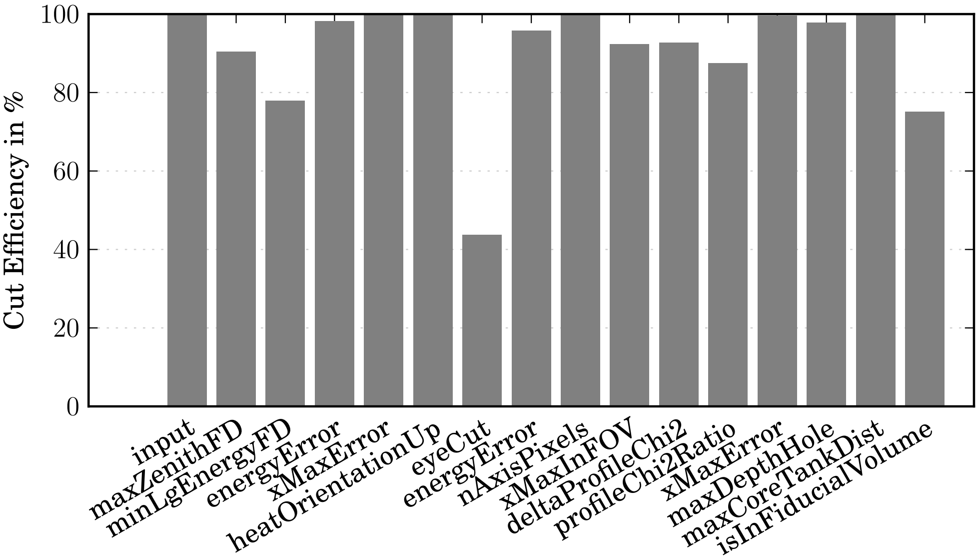

Figure A.9: Selection efficiency for CONEX p data: loose, tight and FOV datasets

A.4.3 CONEX iron

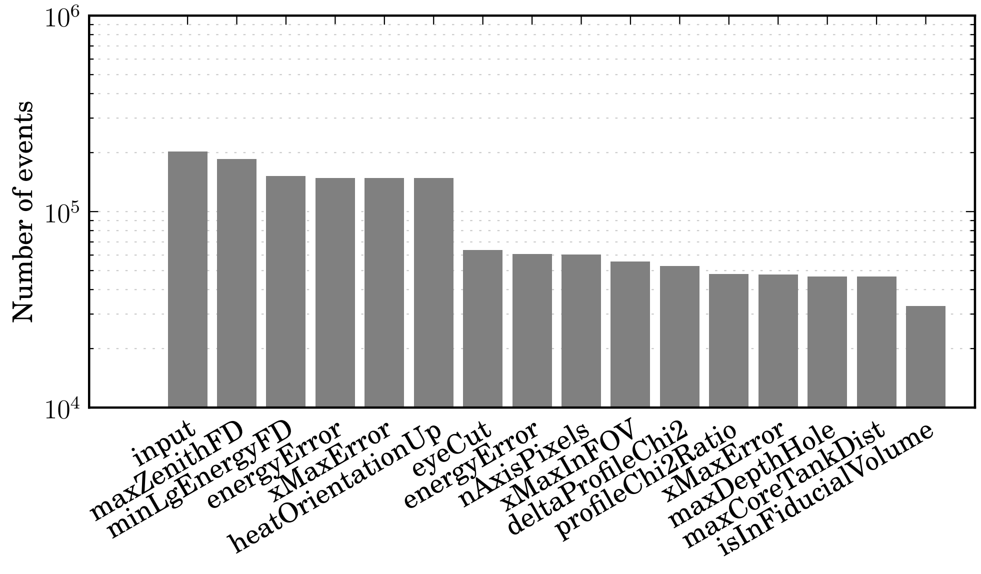

Figure A.10: Events after selection for CONEX Fe data: loose, tight and FOV datasets

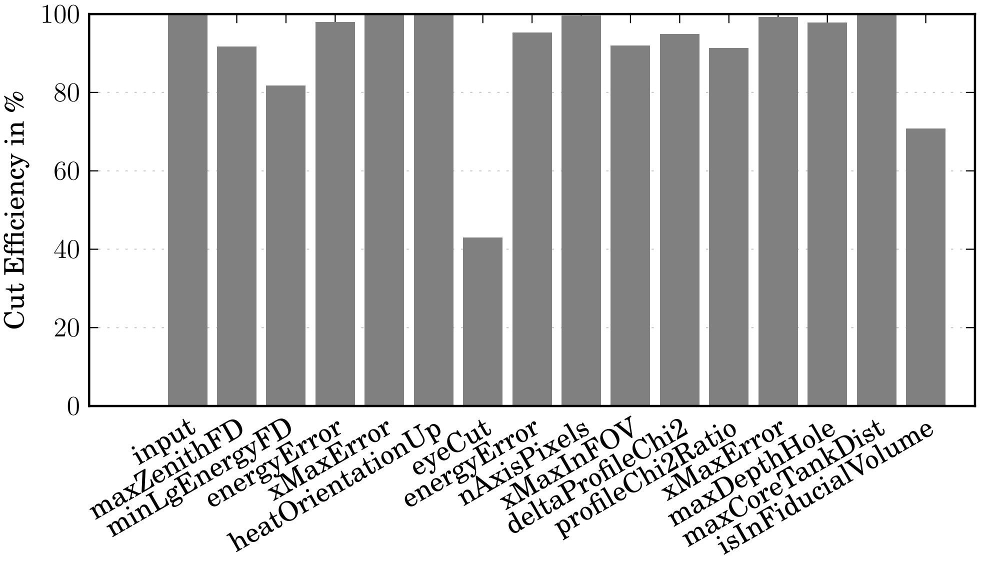

Figure A.11: Selection efficiency for CONEX Fe data: loose, tight and FOV datasets

A.4.4 CORSIKA

Direct Cherenkov fraction cut result is accordingly inverted for high fraction data set.

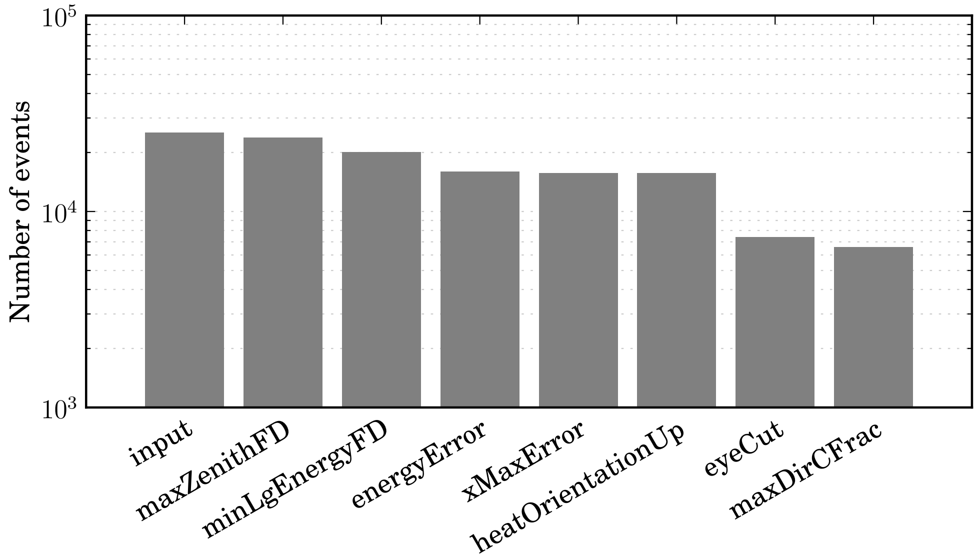

Figure A.12: Events after selection for CORSIKA low Cherenkov fraction data with loose cuts

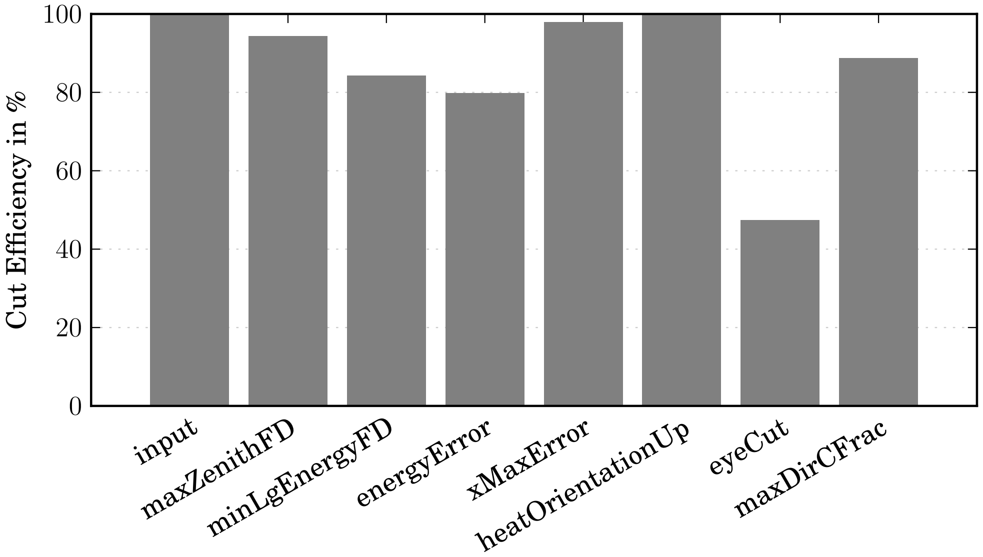

Figure A.13: Selection efficiency for CORSIKA low Cherenkov fraction data with loose cuts

A.5 HEAT data

Number of events of the HEAT data after loose cuts are shown here.

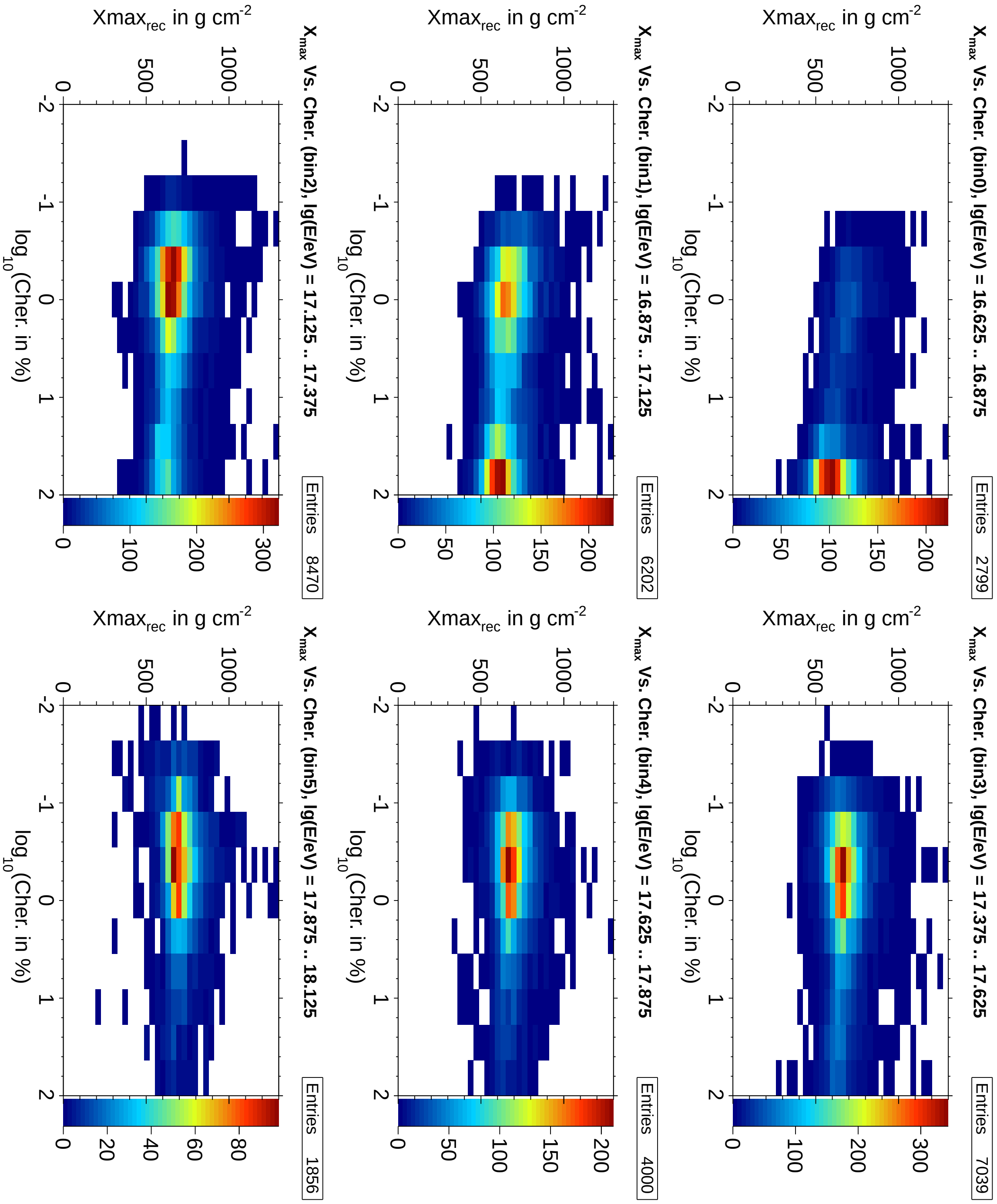

Figure A.14: Distribution of X_{max} over Cherenkov light fraction for HEAT data after loose cuts is shown. ($E = 10^{16.75,\,17.0,\,17.25,\,17.5,\,17.75,\,18.0}$ eV)

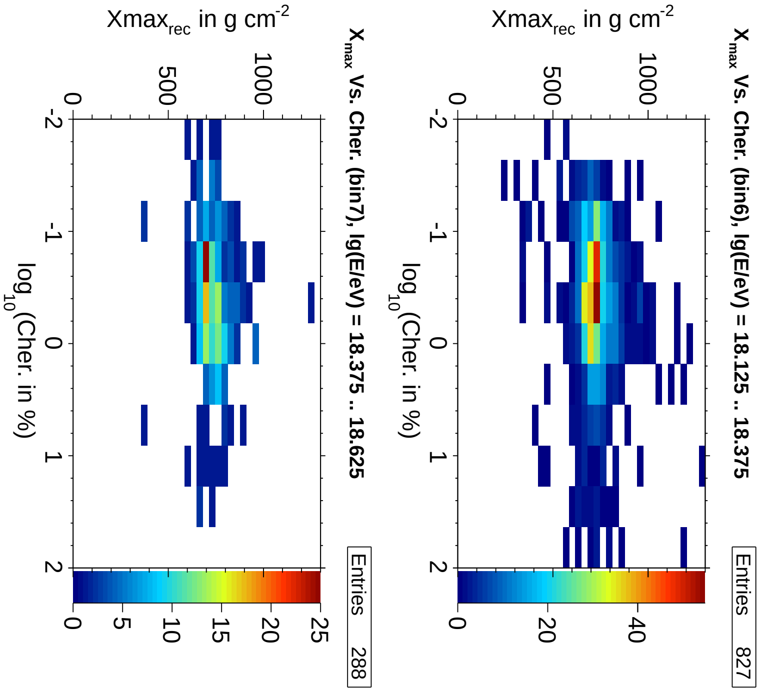

Figure A.14: (cont.) Distribution of X_{max} over Cherenkov light fraction for HEAT data after loose cuts. ($E = 10^{18.25,\,18.5}\,\mathrm{eV}$)

A.6 Atmosphere parametrisation

For every altitude an atmospheric depth is assigned depending on the density profile parametrisation. Typically the US standard atmosphere [76] is used. In [46] it was parametrised as follows:

Layer i	Altitude h km	a_i $\mathrm{g\,cm^{-2}}$	b_i $\mathrm{g\,cm^{-2}}$	c_i cm
1	0 ... 7	-149.801663	1183.6071	954248.34
2	7 ... 11.4	-57.932486	1143.0425	800005.34
3	11.4 ... 37	0.63631894	1322.9748	629568.93
4	37 ... 100	$4.35453690 \cdot 10^{-4}$	655.67307	737521.77
5	> 100	0.01128292	1.	10^9

For the atmosphere layers 1 to 4 the depth is parametrised as:

$$X(h) = a_i + b_i \cdot \exp\left(-\frac{-h}{c_i}\right), \quad \text{withi} = 1, ..., 4, \tag{A.1}$$

for very high altitudes denoted as layer 5, the depth is parametrised linearly:

$$X(h) = a_5 - b_5 \frac{-h}{c_5} \quad . \tag{A.2}$$

Bibliography

[1] V. F. Hess, *Beobachtungen der durchdringenden Strahlung bei sieben Freiballonfahrten*, Phys. Z., 13 (1912), p. 1084.

[2] J. Blümer, R. Engel, and J. R. Hörandel, *Cosmic Rays from the Knee to the Highest Energies.* Submitted to Progr. Part. Nucl. Phys., (arXiv astro-ph/0904.0725), 2009.

[3] A. Letessier-Selvon and T. Stanev, *Ultrahigh energy cosmic rays*, Rev. Mod. Phys, 83 (2011), pp. 907–942.

[4] H. Dembinski, *Measurement of the Ultra High Energy Cosmic Ray Flux from Data of very inclined showers at the Pierre Auger Observatory*, PhD Thesis, RWTH Aachen, 2009.

[5] A. M. Hillas, *The origin of ultra-high-energy cosmic rays*, Ann. Rev. Astron. Astrophys., 22 (1984), pp. 425–444.

[6] K. Greisen, *End to the cosmic-ray spectrum?*, Phys. Rev. Lett., 16 (1966), pp. 748–750.

[7] G. T. Zatsepin and V. A. Kuz'min, *Upper Limit of the Spectrum of Cosmic Rays*, Sov. J. Exp. Theor. Phys. Lett., 4 (1966), p. 78.

[8] H. Ulrich *et al.*, *Energy spectrum and elemental composition of cosmic rays in the pev region*, The European Physical Journal C - Particles and Fields, 33 (2004), pp. s944–s946.

[9] T. Antoni *et al.*, *Kascade measurements of energy spectra for elemental groups of cosmic rays: Results and open problems*, Astroparticle Physics, 24 (2005), pp. 1 – 25.

[10] R. U. Abbasi *et al.*, *First Observation of the Greisen-Zatsepin-Kuzmin Suppression*, Phys. Rev. Lett., 100 (2008), p. 101101.

[11] R. U. Abbasi *et al.*, *Monocular measurement of the spectrum of uhe cosmic rays by the fadc detector of the hires experiment*, Astroparticle Physics, 23 (2005), pp. 157 – 174.

[12] D. R. Bergman, *Chasing the GZK with HiRes*, Mod.Phys.Lett. A, 18 (2003), pp. 1235–1245.

[13] J. Abraham *et al.*, Pierre Auger Collaboration, *Measurement of the energy spectrum of cosmic rays above* 10^{18} *eV using the Pierre Auger Observatory*, Physics Letters B, 685 (2010), pp. 239–246.

[14] K. Nakamura *et al.*, *Review of Particle Physics, 2010-2011.*, Journal of Physics G: Nuclear and Particle Physics, 37 (2010), p. 075021.

[15] K. Schmeiser, *Die harten Ultrastrahlschauer*, Leipzig: J. A. Barth, 1938.

[16] W. Kolhörster, I. Matthes, and E. Weber, *Gekoppelte Höhenstrahlen*, Naturwissenschaften, 26 (1938), pp. 576–576.

[17] P. Auger, R. Maze, and T. Grivet-Meyer, *Extensive cosmic showers in the atmosphere containing ultra-penetrating particles*, C. R. Acad. Sci. Ser. II, 206 (1938), pp. 1721–1722.

[18] O. C. Allkofer and P. K. F. Grieder, *Cosmic rays on earth.*, 1984.

[19] M. Risse and D. Heck, *Energy release in air showers*, Astroparticle Physics, 20 (2004), pp. 661 – 667.

[20] J. Matthews, *A Heitler model of extensive air showers*, Astropart. Phys., 22 (2005), pp. 387–397.

[21] W. Heitler, *The Quantum Theory of Radiation*, Oxford University Press, Oxford, third ed. ed., 1954.

[22] S. Eidelman *et al.*, *The Review of Particle Physics*, Physics Letters, B 592 (2004), p. 1.

[23] T. Gaisser, *Cosmic Rays and Particle Physics*, Cambrigde University Press, Cambridge, 1990.

[24] M. Straub, *Mass composition studies with the low energy extension heat at the pierre auger observatory*, master thesis, RWTH Aachen, III. Physikalisches Institut A, 2012.

[25] T. K. Gaisser and A. M. Hillas, *Reliability of the Method of Constant Intensity Cuts for Reconstructing the Average Development of Vertical Showers*, in Proc. 15th Int. Cosm. Ray Conf., vol. 8, Plovdiv, Bulgaria, 1977, p. 353.

[26] T. Abu-Zayyad *et al.*, *A measurement of the average longitudinal development profile of cosmic ray air showers between* 10^17 *and* 10^18 *eV*, Astroparticle Physics, 16 (2001), pp. 1 – 11.

[27] A. Bunner, *The atmosphere as a cosmic ray scintillator*, Cornell University, 1964.

[28] Yoshiyuki Takahashi and the JEM-EUSO Collaboration, *The jem-euso mission*, 2009.

[29] G. Lefeuvre *et al.*, *Absolute measurement of the nitrogen fluorescence yield in air between 300 and 430 nm*, Nucl.Instrum.Meth.A, 578 (2007), p. 78.

[30] F. Kakimoto *et al.*, *A Measurement of the air fluorescence yield*, Nucl. Instrum. Meth., A372 (1996), pp. 527–533.

[31] M. Nagano, K. Kobayakawa, N. Sakaki, and K. Ando, *New measurement on photon yields from air and the application to the energy estimation of primary cosmic rays*, Astroparticle Physics, 22 (2004), pp. 235 – 248.

[32] M. Ave *et al.*, AIRFLY Collab., *Measurement of the pressure dependence of air fluorescence emission induced by electrons*, Astropart. Phys., 28 (2007), p. 41.

[33] F. Arqueros, J. R. Hörandel, and B. Keilhauer, *Air fluorescence relevant for cosmic-ray detection—summary of the 5th fluorescence workshop, el escorial 2007*, Nuclear Instruments and Methods in Physics Research Section A: Accelerators, Spectrometers, Detectors and Associated Equipment, 597 (2008), pp. 1 – 22.

[34] J. Jelley, *Čerenkov radiation, and its applications*, Pergamon Press, 1958.

[35] I. M. Frank and I. E. Tamm, Compt. rend. acad. sci. U.R.S.S., 14 (1937), p. 107.

[36] A. M. Hillas, *The sensitivity of cerenkov radiation pulses to the longitudinal development of cosmic-ray showers*, Journal of Physics G: Nuclear Physics, 8 (1982), p. 1475.

[37] P. Ciddor and O. S. of America, *Refractive Index of Air: New Equations for the Visible and Near Infrared*, Applied optics, Optical Society of America, 1996.

[38] F. Nerling and U. Karlsruhe, *Description of cherenkov light production in extensive air showers*, (2005). GAP2005-063.

[39] M. M. Haklay and P. Weber, *OpenStreetMap: User-Generated Street Maps*, IEEE Pervasive Computing, 7 (2008), pp. 12–18.

[40] T. H.-J. Mathes, Pierre Auger Collaboration, *The heat telescopes of the pierre auger observatory: Status and first data*, 2011.

[41] J. Abraham *et al.*, Pierre Auger Collaboration, *The Fluorescence Detector of the Pierre Auger Observatory*, Nucl.Instrum.Meth., A620 (2010), p. 227–251.

[42] K. H. Kampert, Pierre Auger Collaboration, *The Pierre Auger Observatory - status and prospects*, Nuclear Physics B Proceedings Supplements, 151 (2005), pp. 393–400.

[43] J. Abraham *et al.*, Pierre Auger Collaboration, *Atmospheric effects on extensive air showers observed with the Surface Detector of the Pierre Auger Observatory*, Astropart. Phys., 32 (2009), pp. 89–99.

[44] L. P. Jr, *Fdsim user's manual - preprod v2r0.* GAP2003-084, 2003.

[45] F. Schmidt and J. Knapp, *Corsika shower images*, 2005.

[46] B. Keilhauer *et al.*, *Impact of varying atmospheric profiles on extensive air shower observation: atmospheric density and primary mass reconstruction*, Astropart. Phys., 22 (2004), pp. 249–261.

[47] N. Scharf, *The energy spectrum of cosmic rays detected with the HEAT extension at the Pierre Auger Observatory*, PhD thesis, RWTH Aachen, III. Physikalisches Institut A, 2012.

[48] D. Kruppke-Hansen and J. Rautenberg, *Investigation of heat's high trigger rate.* GAP2011-121, 2011.

[49] T. Bergmann *et al.*, *One-dimensional Hybrid Approach to Extensive Air Shower Simulation*, Astropart. Phys., 26 (2007), pp. 420 – 432. astro-ph/0606564.

[50] S. S. Ostapchenko, *QGSJET-II: towards reliable description of very high energy hadronic interactions*, Nucl. Phys. B Proc. Suppl., 151 (2006), pp. 143–146. hep-ph/0412332.

[51] R. S. Fletcher, T. K. Gaisser, P. Lipari, and T. Stanev, *SIBYLL: An event generator for simulation of high energy cosmic ray cascades*, Phys. Rev. D, 50 (1994), pp. 5710–5731.

[52] K. Werner, F.-M. Liu, and T. Pierog, *Parton ladder splitting and the rapidity dependence of transverse momentum spectra in deuteron-gold collisions at the BNL Relativistic Heavy Ion Collider*, Phys. Rev. C: Nucl. Phys., 74 (2006), p. 11.

[53] D. Heck *et al.*, *CORSIKA: A Monte Carlo Code to Simulate Extensive Air Showers.* Report FZKA 6019, Karlsruhe, 1998.

[54] D. Heck and T. Pierog, *Extensive Air Shower Simulations with CORSIKA: A User's Guide*, 2011.

[55] A. Fassó, A. Ferrari, J. Ranft, and P. Sala, *Fluka: a multi-particle transport code.* CERN-2005-10 (2005), INFN/TC 05/11, SLAC-R-773, 2005.

[56] L. A.A.., U. V.V., and P. A.V., *Fluctuations of the number of particles in an electromagnetic cascade*, Sov. J. Nucl. Phys., 30:2 (1979), pp. 223–226.

[57] K. Bernlöhr, *Simulation of imaging atmospheric Cherenkov telescopes with CORSIKA and sim telarray*, Astropart. Phys., 30 (2008), pp. 149–158.

[58] I. A. of Geomagnetism *et al.*, *International geomagnetic reference field: the eleventh generation*, Geophysical Journal International, 183 (2010), pp. 1216–1230.

[59] M. Grigat, *Large Scale Anisotropy Studies of Ultra High Energy Cosmic Rays Using Data Taken with the Surface Detector of the Pierre Auger Observatory*, PhD Thesis, RWTH Aachen, 2011.

[60] P. Assis *et al.*, *Manual of fluorescence detector simulation in offline.* GAP2008-014, 2008.

[61] S. Falk *et al.*, *A first look at heat data.* GAP2010-123, 2010.

[62] S. Falk, R. Engel, R. Ulrich, and M. Unger, *Telescope alignment studies.* GAP2011-123, 2011.

[63] B. F. Patrick Younk, *On sdp reconstruction accuracy.* GAP2006-086, 2006.

[64] D. Kümpel, *Geometry reconstruction of fluorescence detectors revisited*, diploma thesis, Bergische Universitä Wuppertal, 2007.

[65] D. Gora *et al.*, *Universal lateral distribution of energy deposit in air showers and its application to shower reconstruction*, Astropart.Phys., 24 (2006), pp. 484–494.

[66] M. Giller and G. Wieczorek, *Influence of the scattered cherenkov light on the width of shower images as measured in the eas fluorescence experiments*, Astropart.Phys., 31 (2009), pp. 212–219.

[67] M. Unger, *Showerprofile reconstruction from fluorescence and cherenkov light.* GAP2006-010, 2006.

[68] M. Unger *et al.*, *Reconstruction of longitudinal profiles of ultra-high energy cosmic ray showers from fluorescence and cherenkov light measurements*, Nucl. Instrum. Meth., A588 (2008), pp. 433 – 441. arXiv astro-ph/0801.4309.

[69] F. Nerling, J. Blümer, R. Engel, and M. Risse, *Universality of electron distributions in high-energy air showers - description of cherenkov light production*, Astropart.Phys., 24 (2005), pp. 421–437.

[70] J. Bellido, *Measuring the mean xmax as a function of the shower energy using the hybrid data.* GAP2007-019, 2007.

[71] M. Settimo, L. Perrone, and C. Bonifazi, *Hybrid angular resolution with corsika showers and comparison to data.* GAP2009-063, 2009.

[72] D. Kuempel, *Geometry reconstruction of fluorescence detectors revisited.* GAP2007-099, 2007.

[73] E. J. Ahn *et al.*, *Measurement of the depth of shower maximum of cosmic rays above 1 eev.* GAP2009-078, 2009.

[74] R. Brun and F. Rademakers, *Root - an object oriented data analysis framework*, in AIHENP'96 Workshop, Lausane, vol. 389, 1996, pp. 81–86.

[75] T. Niggemann, *New telescope design with silicon photomultipliers for fluorescence light detection of extensive air showers*, master thesis, RWTH Aachen, III. Physikalisches Institut A, 2012.

[76] National Aeronautics and Space Administration (NASA), *U.s. standard atmosphere 1976.* Report NASA-TM-X-74335, 1976.

Danksagung

Mein außerordentlicher Dank gilt Herrn Prof. Dr. Thomas Hebbeker fur die Möglichkeit diese Arbeit anfertigen zu dürfen und an dem Pierre-Auger-Observatorium mitarbeiten zu können. Seine Denkanstöße und Vorschläge zusammen mit kritischen Betrachtungen haben immer die Probleme aufzuzeigen und zu lösen geholfen. Besonderes möchte ich für die Gelegenheit danken den Experiment vor Ort und in Aktion zu sehen und den internationalen Forschungsbetrieb mitzuerleben. Außerdem möchte ich Herrn Prof. Dr. Christopher Wiebusch für die Bereitschaft danken, der Zweitgutachter der Arbeit zu sein.

Mein Großer Dank gilt allen Mitgliedern der Aachener Auger-Gruppe, die zu allen Fragen und Problemen die Hilfestellung und den Rat boten. Die Gruppenmeetings waren immer sehr hilfreich für die Arbeit.

Dr. Christine Meurer möchte ich für das Begeistern für das Thema und die einleitende Betreuung besonderes Danken.

Der große Dank gilt Marcel Straub und Matthias Plum für das Korrekturlesen der Arbeit und die vielen Anregungen. Nils Scharf und Maurice Stephan möchte ich sehr für viele Wegweisungen danken.

Ich danke Stefan und Anna für die schöne TeX-Vorlage.

Mi agradecimiento personal a mi mejor mitad, que me ha apoyado con todas sus fuerzas, y en todos los casos.

Meinen Eltern möchte ich für die stetige Unterschtützung und den Rückhalt in meinem ganzen Physikstudium danken.

Erklärung

Hiermit versichere ich, dass ich diese Arbeit einschließlich beigefügter Zeichnungen, Darstellungen und Tabellen selbstständig angefertigt und keine anderen als die angegebenen Hilfsmittel und Quellen verwendet habe. Alle Stellen, die dem Wortlaut oder dem Sinn nach anderen Werken entnommen sind, habe ich in jedem einzelnen Fall unter genauer Angabe der Quelle deutlich als Entlehnung kenntlich gemacht.

Aachen, den 16. Juli 2012

Ilya Bekman